UNIVERSITY OF CALIFORNIA, SAN DIEGO

Dynamics of stratified flow past a sphere: simulations using temporal, spatial and body inclusive numerical models.

A dissertation submitted in partial satisfaction of the
requirements for the degree
Doctor of Philosophy

in

Engineering Sciences (Mechanical Engineering)

by

Anikesh Pal

Committee in charge:

Professor Sutanu Sarkar, Chair
Professor Yuri Bazilevs
Professor Juan Carlos Del Alamo
Professor Eugene R. Pawlak
Professor Stefan Llewellyn Smith

2016

The dissertation of Anikesh Pal is approved, and it is acceptable in quality and form for publication on microfilm and electronically:

_____

_____

_____

_____

_____

Chair

University of California, San Diego

2016

Dedicated to Maa, Baba and Alibha

TABLE OF CONTENTS

LIST OF SYMBOLS

$\mathbf{u_i}(i = 1, 2, 3)$	Velocity in cartesian coordinate system
u_r	Velocity in radial direction
u_θ	Velocity in azimuthal direction
u_z	Velocity in streamwise direction
U_∞	Free stream velocity
U_0	Defect velocity
ρ	Total density
ρ^*	Deviation of from the background density
ρ_{bg}	Background density
ρ_0	Reference density
ν	Molecular viscosity
ε	Turbulent dissipation
κ	Thermal diffusivity
Re	Reynolds number
Re_b	Buoyancy Reynolds number
Fr	Froude number
Pr	Prandtl number
$\langle\cdot\rangle$	Reynolds average
g	Acceleration due to gravity
Ω	Wave frequency
N	Buoyancy frequency

LIST OF FIGURES

LIST OF TABLES

ACKNOWLEDGEMENTS

I would like to sincerely thank my advisor Prof. Sutanu Sarkar for his constant guidance and inspiration for the past 5 years. Also, thanks to all my thesis committee members Prof. Stefan Llewellyn Smith, Prof. Eugene R. Pawlak, Prof. Yuri Bazilevs and Prof. Juan Carlos Del Alamo for their help and suggestions on my thesis work. I would like to thank Prof. Elias Balaras and Dr. Antonio Posa for sharing the IBM code.

I would also like to thank all my previous and current colleagues Hieu, Matt, Eric, Narsimha, Vamsi, Masoud and Karu for the support, suggestions and friendship at the CFD lab at UCSD. Also, I would like to thank my close friends and roommates Josh, James and Lawrance for all their support and help in my personal life.

I owe my dissertation to my parents and it is tough to put in words how grateful I am to them for their love, support, inspiration and sacrifices that led me to this phase of life.

A very special thanks to Alibha, for being morally supportive for the past one and half years and inspiring me on a regular basis which helped me finish my Ph.D within a limited time.

I am grateful for the financial support provided through Office of Naval Research (ONR) Grant N00014-15-1-2718 administered by Dr. Ron Joslin. I am also thankful to the Department of Defense High Performance Computing Modernization Program from providing computational resources.

Chapter 2 is a reprint of the material published in the following journal: **A. Pal**, M. B. deStadler, & S. Sarkar (2013), The spatial evolution of fluctuations in a self-propelled wake compared to a patch of turbulence,. *Phys. of Fluids.*, 25 (9), 095106. The thesis author was the primary author of this paper.

Chapter 3 is a reprint of the material published in the following journal: **A. Pal**, & S. Sarkar (2015), Effect of external turbulence on the evolution of a wake in stratified and unstratified environments. *J. Fluid Mech.*, 772, 361-385. The thesis author was the primary author of this paper.

The contents of Chapter 4 are submitted in the following journal: **A. Pal** , S. Sarkar, A. Posa & E. Balaras (2016), DNS of stratified flow past a sphere at a Reynolds number of 3700., *J. Fluid Mech.*. The thesis author was the primary author of this paper.

Chapter 5 is a reprint of the material published in the following journal: **A. Pal** , S. Sarkar, A. Posa & E. Balaras (2016), Regeneration of turbulent fluctuations in low Froude number flow over a sphere at a Reynolds number of 3700. *J. Fluid Mech.*, 804, R2, 1-11. The thesis author was the primary author of this paper.

The contents of Chapter 6 are in the process of preparation for submission in the following journal: **A. Pal** & S. Sarkar (2016)., Internal waves generated by flow past a sphere at a Reynolds number of 3700 in a stratified fluid. (in preparation for *J. Fluid Mech.*). The thesis author is the primary author of this paper.

VITA

2007	B. Tech. in Mechanical Engineering, Kalyani Government Engineering College, West Bengal, India
2010	M. Tech. in Mechanical Engineering (Fluids and Themal Sciences), Indian Institute of Technology Kanpur, India
2016	Ph. D. in Engineering Sciences (Mechanical Engineering), University of California, San Diego, USA

PUBLICATIONS

JOURNAL PAPERS

1. **Pal A.** and Sarkar S. (2016), "Internal waves generated by flow past a sphere at a Reynolds number of 3700 in a stratified fluid." *J. Fluid Mech. in preparation.*

2. **Pal A.**, Sarkar S. Posa A., and Balaras E. (2016), "DNS of stratified flow past a sphere at a Reynolds number of 3700" *J. Fluid Mech. submitted.*

3. Chongsiripinyo K., **Pal A.**, and Sarkar S. (2016), "On the vortex dynamics of flow past a sphere at Re = 3700 in a uniformly stratified fluid" *Phys. of Fluids. in revision.*

4. **Pal A.**, Sarkar S., Posa A. and Balaras E.(2016) , "Regeneration of turbulent fluctuations in low-Froude-number flow over a sphere at a Reynolds number of 3700." *J. Fluid Mech.*, 804, R2, 1-11 .

5. **Pal A.** and Sarkar S. (2015), "Effect of external turbulence on the evolution of a wake in stratified and unstratified environments" *J. Fluid Mech.*, 772, 361-385.

6. Y Bazilevs, A Korobenko, J Yan, **A. Pal**, SMI Gohari, S Sarkar. (2015), "ALE-VMS formulation for stratified turbulent incompressible flows with applications," *Mathematical Models and Methods in Applied Sciences*, 25(12), 2349-2375 .

7. **Pal A.**, deStadler M.B. and Sarkar S. (2013), "The spatial evolution of fluctuations in a self-propelled wake compared to a patch of turbulence," *Phys. of Fluids.*, 25 (9), 095106 .

8. **Pal A.**, Bandyopadhyay D., Biswas G. and Eswaran V. (2012), "Enhancement of heat transfer using delta-winglet type vortex generators with a common-flow-up arrangement," *Numerical Heat Transfer, Part A: Applications.*, 61(12), 912-928.

ABSTRACT OF THE DISSERTATION

Dynamics of stratified flow past a sphere: simulations using temporal, spatial and body inclusive numerical models.

by

Anikesh Pal

Doctor of Philosophy in Engineering Sciences (Mechanical Engineering)

University of California, San Diego, 2016

Professor Sutanu Sarkar, Chair

Wakes of bluff bodies in a stratified environment are common in oceanic and atmospheric flows. Some examples are marine swimmers, underwater submersibles, flow over mountains and around islands. The first part of the present research in stratified wakes concerns temporal/spatial simulations of turbulent self-propelled/towed wakes without including a body. Direct numerical simulations are performed to contrast the influence of the mean velocity profile with that of the initial turbulence on the subsequent evolution of velocity and density fluctuations in a stratified self-propelled wake. It is also verified that results of temporal simulations matches with that of the spatial simulations when the initial near-wake condition of the temporal approximation is chosen to match the inflow of the spa-

tially evolving model. Typically, the wake of a body develops in the presence of external fluctuations, motivating a study of wake evolution under the influence of various intensities of external turbulence. Simulations and theoretical arguments show an increase in the decay of wake deficit when the external turbulence level exceeds that in the wake. Nevertheless, stratification prolongs wake lifetime, irrespective of external turbulence.

The second part of this research focuses on flow past a sphere in a stratified fluid at a sub-critical Reynolds number of 3,700 and for a range of Froude numbers $Fr = U/ND \in [0.025, \infty]$. The conservation equations are solved in a cylindrical coordinate system and an immersed boundary method is employed to represent the sphere. The high resolution enables closure of the turbulent kinetic energy budget. The domain extends into the far wake (x/D = 80) enabling, for the first time, simulation of the transition from the near wake through the non-equilibrium region into coherent, primarily horizontal motions. Buoyancy decreases the recirculation length, inhibits the vertical rollup of the separating shear layer, promotes steady lee waves and unsteady turbulence-generated waves and, most importantly, increases the mean wake lifetime by decreasing the loss to turbulence. A novel finding of this research is the *regeneration* of turbulent fluctuations in the near wake when the stratification increases beyond a critical level (Fr decreases beyond a critical value) which is in contrast to the previous results at lower Re that suggest suppression of turbulence with increasing stratification. Vorticity evolution, energy spectra and the turbulence energy equation help explaining turbulence regeneration. The simulations also enable us to quantify the distinction between the body and turbulence generated internal waves, in terms of the amplitude, frequency, potential energy distribution and propagation angles. With a decrease in Fr, the body generation mechanism become stronger and waves exhibit upstream propagation.

Chapter 1

Introduction

Wakes in the natural environment are associated with engineered devices, e.g., ships, underwater submersibles, aircraft, unmanned aerial vehicles (UAVs), and wind turbines, with marine swimmers and aerial flyers, and with topographic features such as islands and mountains. Stratification of the environment affects these wakes leading to distinctive features. A comprehensive review of experimental studies prior to 1979 is given by Lin & Pao (1979) while the recent review by Spedding (2014) includes later work with an emphasis on laboratory experiments while also considering wakes of marine animals as well as geophysical examples.

Lin & Pao (1979) reviewed high-Fr wakes with $Fr = O(10 - 1000)$ and concluded that, after $Nt = O(1)$, buoyancy qualitatively changes the structure of the wake through the inhibition of vertical motion. Here, $Fr = U_\infty/ND$ where U_∞ is the speed of the freestream fluid relative to the body, D is the body diameter, N is the background value of the buoyancy frequency and $t = x/U$ is the time that corresponds to streamwise distance x from the body. Their visualizations for slender-body, high-Fr flows show wake collapse, i.e. a decrease of the vertical thickness of the wake, and the formation of large-scale vortices in the horizontal flow. Lin *et al.* (1992*a*) studied the behavior of flow past a sphere for $Re = [5, 10000]$ and $Fr = [0.005, 15]$, finding a turbulent wake for $Re > 2000$ and sufficiently high Fr. They found that the vertical and the horizontal thickness of wakes with $Fr \gtrsim 2$ grow similarly following a $t^{1/3}$ law (the classical self-similar behavior of an unstratified round wake) until $Nt \approx 2$, where the vertical thickness

reaches its maximum. After $Nt \approx 2$, the vertical wake thickness normalized by D becomes $O(1)$, whereas in the horizontal direction it increases as $t^{1/2}$. It is worth noting that the scalings proposed by Lin & Pao (1979) were based on shadowgraph visualizations.

Hanazaki (1988) used DNS to study flow past a sphere at a relatively low $Re = 200$ and $Fr_R = [0.25, 200]$ ($Fr_R = U_\infty/NR$, where R is the sphere radius). He found steady flow with an attached separation bubble and discussed the effect of the steady lee wave pattern on flow separation and drag coefficient. Flow past a sphere at higher Re that allows unsteadiness was investigated experimentally by Lin *et al.* (1992*b*), Chomaz *et al.* (1992) and Chomaz *et al.* (1993a). These authors describe how flow separation, vortex shedding, and the lee wave pattern change significantly as the flow conditions change among the regimes of low Fr, $Fr = O(1)$, and high Fr. Depending on the strength of the stratification, the internal wave field consists of lee waves generated by the body and random internal waves generated by the turbulent wake. Properties of these waves were studied in the laboratory by Hopfinger *et al.* (1991); Bonneton *et al.* (1993); Chomaz *et al.* (1993a); Bonneton *et al.* (1996).

The late-wake evolution in the horizontal center plane of the wake of a sphere towed in a stratified fluid was investigated by Spedding *et al.* (1996a) at $Re = [10^3, 10^4]$ and $Fr_R = [1, 10]$ using digital particle image velocimetry (DPIV). For $Re > 5000$, the streamwise average of quantities such as normalized fluctuation velocity, vorticity magnitude and energy dissipation rate exhibited power-law scalings similar to that of axisymmetric turbulent wakes. The stratified wakes spread horizontally with a growth rate of $t^{1/3}$ similar to the self-similar, unstratified wake while the defect velocity was an order of magnitude larger than the unstratified case. As in previous experiments, the late wake was dominated by coherent vortices. Spedding (1997) expanded the study to the high-Fr regime, $Fr_R = [10, 240]$, and identified a non-equilibrium (NEQ) phase that commences at $Nt \simeq 2$, during which the initial near-wake (NW) turbulence feels the influence of the background density gradient and the mean velocity decay of the wake is substantially reduced by buoyancy to approximately $(Nt)^{-0.25}$. There is an

eventual transition to a quasi two-dimensional (Q2D) phase where the flow is constrained in the vertical direction owing to the effect of buoyancy, pancake vortices emerge and the mean velocity decays as approximately $(Nt)^{-0.76}$, faster than in the NEQ regime. Bonnier & Eiff (2002) experimentally studied sphere wakes at $(Fr_R, Re) = (3, 3400), (6, 6900), (10, 11500)$ and found an "accelerated collapse" phase with an abrupt increase in the centerline defect velocity at $Nt \approx 3$ that lasted for a period of $\Delta Nt \approx 5$.

Numerical simulations performed in the past two decades to study stratified wakes have primarily used the temporally evolving model, commencing with the DNS of Gourlay *et al.* (2001) who simulated a wake at nominal $Re = 10^4$ and $Fr = 10$ on a grid with 162 million grid points. A conclusion was that pancake eddies form in the late wake, independent of the absence in the initial conditions of coherent fluctuations associated with vortex shedding off the body. Later numerical studies of wake statistics, turbulence budgets and vortex dynamics include the LES by Dommermuth *et al.* (2002) at $Re = 10^4, 10^5$ and $Fr = 2$ with improved initial conditions, the DNS by Brucker & Sarkar (2010) of towed and self-propelled wakes at $Re = 10^4$ and $Re = 5 \times 10^4$, using a grid with up to 2 billion grid points, the implicit LES of Diamessis *et al.* (2011) conducted over a wide range of Fr and Re, and DNS of a weakly-stratified wakes by Redford *et al.* (2015). At high Re, the NEQ regime has enhanced turbulence owing to secondary KH instabilities (Diamessis *et al.*, 2011) and the duration of the NEQ regime is extended (Brucker & Sarkar, 2010). By quantifying of the mean wake energetics, Brucker & Sarkar (2010) found that, owing to the buoyancy-induced reduction of Reynolds shear stress of the vertical velocity, the turbulent production responsible for the transfer of energy from mean to fluctuations is reduced, thus leading to defect velocity in the NEQ regime that is substantially higher than in the unstratified wake. This explanation for the longer lifetime of stratified wakes was confirmed by Redford *et al.* (2015) who also found that the robust Reynolds shear stress associated with quasi two-dimensional motions leads to a faster (relative to the NEQ regime) decay of the mean wake velocity in the Q2D regime. Abdilghanie & Diamessis (2013) characterized the internal wave properties and found that the internal wave emission

is prolonged over a longer time interval at high Re. Pal & Sarkar (2015) examined the effect of external fluctuations finding that, although the wake turbulence was enhanced and the decay of the wake defect velocity was somewhat increased, the stratified wake was still long lived relative to its unstratified counterpart.

DNS of the turbulent wake in a computational model which includes the body is relatively recent. The unstratified case was studied using DNS by Rodriguez *et al.* (2011) at $Re = 3,700$ using an unstructured grid. Vortex shedding at a frequency corresponding to $St = 0.215$ occurred at random azimuthal positions leading to a helical-like configuration of the downstream wake. Passive scalar mixing was studied by de Stadler *et al.* (2014) who performed LES of a heated sphere at $Re = 10,000$. Bazilevs *et al.* (2014*b*), in their simulation of flow past a sphere at $Re = 3700$, found that, due to the free-stream turbulence in the inlet conditions, the near-wake turbulence is substantially increased, the recirculation bubble decreases significantly and the drag force on the sphere is increased. Temporal evolution of the far wake of a sphere in a stratified fluid, using the initial condition from a spatially evolving simulation, was carried out by Pasquetti (2011) at $Re = 10^4$ and $Fr = 25$. Orr *et al.* (2015) numerically investigated flow over a sphere at $Re = 200, 1000$ and $1 \leq Fr \leq \infty$ using body-fitted grids. They provided a parametrization of the near wake based on the wake height, the downstream distance and Fr. Simulations of flow past a sphere at $Re = 3700$ in moderate ($Fr \sim O(1)$) to highly ($Fr < O(1)$) stratified environment have been reported by Pal *et al.* (2016*b*,*a*). Buoyancy suppressed turbulence, so that by $Fr = 0.5$, there is negligible unsteadiness in the wake. However, further decrease of Fr below approximately 0.25 results in regeneration of turbulence owing to a new regime of vortex shedding. A discussion of the coherent structures and the enstrophy dynamics in these low-Fr sphere wakes is provided by Chongsiripinyo *et al.* (2016).

In the first phase of the thesis research (Pal *et al.*, 2013), direct numerical simulation is used to contrast the influence of the mean velocity profile with that of the initial turbulence on the subsequent evolution of velocity and density fluctuations in a stratified wake. The evolution of the fluctuations is found to be strongly dependent on the initial energy spectrum, the kinetic energy is sub-

stantially smaller, and the late-wake vortices are less organized. The effect of the mean velocity field is negligible for mean kinetic energy (MKE) of the order 10% of the total kinetic energy and the evolution in this case is similar to a turbulent patch with the same initial energy spectrum. Increasing the MKE to 50% shows significant differences from the turbulent patch with the same initial energy spectrum during the initial stages of the evolution, but at later stages the evolution of turbulence statistics is similar.

In the second phase, the evolution of a towed stratified wake under the influence of external turbulence in the background is investigated using DNS. A series of simulations are carried out at a Reynolds number of 10 000 and Froude number of 3 for external turbulence whose initial level varies between zero and a moderate intensity of up to 7% relative to the free stream and whose initial integral length scale is of the same order as that of the wake turbulence. Background turbulence, especially at a level of 3% or above, is found to have substantial quantitative effects in the stratified simulations. An increase in the turbulence within the wake is observed due to the entrainment of external turbulence, and the energy transfer through turbulent production from mean to fluctuating velocity also increases, leading to reduced mean velocity. A corresponding series of simulations for the unstratified situation is also carried out at the same Reynolds number of 10 000 and with similar levels of external turbulence. Theoretical arguments and additional simulations are provided to show that the level of external turbulence relative to wake turbulence (dissimilar between the this investigation and (Rind & Castro, 2012a) is a key governing parameter in both stratified and unstratified backgrounds.

In the third phase, direct numerical simulation of flow past a sphere in a stratified fluid with the body is carried out at a sub-critical Reynolds number of 3700 and $Fr = U_\infty/ND = 1, 2$ and 3 to understand the dynamics of moderately stratified flows with $Fr = O(1)$. With increasing stratification, the separated shear layer plunges inward vertically and its roll-up is inhibited, the recirculation zone

is shortened, and the mean wake decays at a slower rate of $U_0 \propto (x_1/D)^{-0.25}$ in the non-equilibrium (NEQ) region. The longer lifetime of the mean wake is due to a reduction of turbulent production by buoyancy. The transition from the near wake where U_0 has a decay rate similar to the unstratified case to the NEQ regime occurs as an oscillatory modulation by a steady lee wave pattern with a period of $Nt = \pi$ that leads to a period of accelerated U_0 between $Nt = \pi$ and approximately $Nt = 2\pi$. Buoyancy induces significant anisotropy among the velocity components and between their vertical and horizontal profiles. Spectra of vertical velocity show a discrete peak in the near wake that is maintained further downstream. The turbulent kinetic energy (TKE) balance is computed and contributions from pressure transport and buoyancy are found to become increasingly important as stratification increases.

As a follow-up problem, direct numerical simulations (DNS) are performed to study the behavior of flow past a sphere in the regime of high stratification (low Froude number Fr). In contrast to previous results at lower Re that suggest monotone suppression of turbulence with increasing stratification in flow past a sphere, it is found that, below a critical Fr, increasing the stratification induces unsteady vortical motion and turbulent fluctuations in the near wake. The near wake is quantified by computing the energy spectra, the turbulence energy equation, the partition of energy into horizontal and vertical components, and the buoyancy Reynolds number. These diagnostics show that the stabilizing effect of buoyancy changes flow over the sphere to flow around the sphere. This qualitative change in the flow leads to a new regime of unsteady vortex shedding in the horizontal planes that results in turbulence regeneration.

In the final phase of the thesis, internal waves generated owing to the fluid motion past the body are investigated. There are two kind of waves generated due to the movement of the fluid past a body: (a) lee waves, and (b) random waves. The behavior of these waves in terms of energy content, wavelength, frequency are analyzed with the variation in the intensity of the stratification. It is also found

that the drag coefficient C_d *increases* with the increase in stratification. This finding is in contrast with the previous studies, where a *decrease* in C_d is reported with the increase in stratification irrespective of Re.

Chapter 2

The Spatial Evolution of Fluctuations in a Self-Propelled Wake compared to a Patch of Turbulence.

2.1 Introduction

The turbulent wake behind a body moving under its own thrust in a stratified fluid is of importance in flows associated with underwater submersibles in naval applications and with swimming marine animals. Experimental studies of a turbulent wake have a long history. Lin & Pao (1979), in their review, concluded that turbulent wakes behave differently depending upon whether the environment is stratified or unstratified. Buoyancy eventually controls the wake by inhibiting vertical motion, leading to wake collapse, propagation of internal gravity waves and, finally, the formation of coherent vortices with primarily horizontal motion. Naudascher (1965), Higuchi & Kubota (1990) and Sirviente & Patel (2000) performed experimental investigations of non-swirling, jet-propelled momentumless wakes in an unstratified environment. Higuchi & Kubota (1990) found a higher decay rate of the centerline mean velocity defect in a zero-momentum case. After

a long gap in the published literature, reports of experimental studies of stratified turbulent wakes recommenced in the case of towed bodies using primarily the generic example of a towed sphere, Chomaz *et al.* (1993*b*,*a*); Spedding *et al.* (1996b); Spedding (1997, 2002). Spedding (1997) identified three regimes during the evolution of a stratified wake: (a) a near-wake (NW) region where the velocity fluctuations are three-dimensional and buoyancy effects are negligible, (b) a non-equilibrium region (NEQ) in which the flow is increasingly influenced by buoyancy resulting in a restratification-driven transfer of potential energy to mean kinetic energy, enhanced internal wave radiation and reduction of the vertical component of turbulence, and, (c) a quasi two-dimensional (Q2D) region dominated by pancake-like organized vortices with strong interspersed vertical gradients. Spedding (1997) also proposed a universal decay law for the mean defect velocity in the three regimes with the decay rate in the NEQ regime being significantly smaller than in either the NW regime or the Q2D regime.

All the numerical turbulence-resolving studies of stratified late wakes are based on a *temporally* evolving model of the wake. Canonical profiles for the mean velocity and turbulence are assumed as initial conditions and the subsequent development of the flow is simulated in a streamwise-periodic domain. Gourlay *et al.* (2001) performed the first three-dimensional DNS of initially turbulent wakes with net momentum and found that the formation of coherent structures in the late wake is independent of the initial seeding of the fluctuating fields. Dommermuth *et al.* (2002) computed the late wake of a towed sphere in an unstratified and uniformly stratified fluid at $Re = 10^4$ and 10^5 by using large eddy simulation (LES) and found the three stages (NW, NEQ and Q2D) of the wake evolution and qualitative similarities with laboratory experiments.

Recent simulations of the wake as discussed below clearly show that, at high Re, stratified turbulence exhibits substantial enhancement in transport and mixing as suggested by the simulations of Riley & deBruynKops (2003); Brethouwer *et al.* (2007) which have a different configurations. Brucker & Sarkar (2010) performed DNS at $Re = 10\ 000$ and $50\ 000$ to compare the evolution of self-propelled and towed wakes in a stratified fluid. Their flow initialization was similar to that used

by Dommermuth *et al.* (2002) and, although, their results were similar at $Re = 10$ 000, the NEQ regime was found by Brucker & Sarkar (2010) to be substantially longer at $Re = 50$ 000 including a phase in which the decay rate of the mean velocity was significantly lower relative to the Re =10 000 case. The turbulent dissipation rate, ε, was also found to exhibit inertial scaling during which $\varepsilon \sim u^3/l \propto t^{-7/3}$. Meunier *et al.* (2006) also predicts prolongation of the NEQ regime and the late appearance of the Q2D regime for higher Reynolds number via their analytical model based on the self-preservation of the flow. Diamessis *et al.* (2011) found a longer NEQ regime at higher Reynolds number and secondary Kelvin-Helmholtz vortices up to $Nt = 100$ when they performed spectral multi-domain-based simulations of the turbulent wake of a towed sphere.

Abdilghanie & Diamessis (2013) examined the internal wave field of a stratified turbulent wake, showing that the associated drag increases with increasing Re to about 9% at the highest simulated Re. Interestingly, the radiated waves cluster in a band around approximately 45° propagation angle as in previous laboratory experiments: Sutherland & Linden (1998); Dohan & Sutherland (2003) and numerical simulations Taylor & Sarkar (2007); Pham *et al.* (2009) of waves emitted by broad-band turbulence. The high- and low-frequency components (correspondingly, high and low propagation angles with respect to the horizontal) of the wave field were found to exhibit preferential viscous decay consistent with the model proposed by Taylor & Sarkar (2007).

A body moving at constant velocity in an unstratified fluid under its own power has a momentumless wake (the integral of the momentum is zero) whose behavior is thought to be qualitatively different from towed wakes. The corresponding situation in the stratified case leads to the integrated momentum in the wake deviating from zero by the momentum carried away by the radiated wave field. In the unstratified case, Tennekes & Lumley (1972), on the basis of a self-similarity analysis that assumes constant eddy viscosity, assert that the centerline defect velocity in a momentumless wake decays faster, $U_0 \propto x^{-4/5}$, relative to the $U_0 \propto x^{-2/3}$ decay of towed wakes. The stratified situation of self-propelled wake evolution into the far wake has been studied only recently: Meunier & Spedding

(2006); Brucker & Sarkar (2010). Unlike prior findings in the unstratified case, the laboratory data of Meunier & Spedding (2006)(available only for $Nt > 50$) showed an irregular mean velocity profile. This finding prompted Meunier & Spedding (2006) to conjecture that that the momentumless wake could have a null mean velocity (mean defect velocity is negligible compared to r.m.s. velocity fluctuation). These authors also reported that, relative to the towed wake, the momentumless wake had smaller horizontal spacing between vortices, significantly slower decay of horizontal velocity fluctuations, and a higher sensitivity to the initial conditions such as propeller width. Brucker & Sarkar (2010) performed the first turbulence-resolving simulation of the momentumless wake, employing the canonical axisymmetric mean profile (see figure 2.2(a) of the present paper) having positive and negative velocity lobes that was found in the unstratified situation: Naudascher (1965); Higuchi & Kubota (1990); Sirviente & Patel (2000). The momentumless wake was found by Brucker & Sarkar (2010) to decay faster than the corresponding towed wake. The reason was that the momentumless wake with the same defect velocity and wake radius as a towed wake has larger mean shear due to the multi-inflectional velocity profile leading to a larger shear production and conversion to turbulence. The authors also found the existence of NW, NEQ and Q2D regime in the momentumless wake, similar to the towed wake. Voropayev *et al.* (1999) studied the wake of a maneuvering body in a stratified fluid experimentally and established that the acceleration of the body transfers significant momentum to the surrounding fluid leading to the formation of coherent dipoles, much larger and different from the ones that form in the late wake at steady state. Pasquetti (2011) simulated the far wake of a sphere at Pr=7, Re=10,000 and Fr=25 by using a temporal approximation, but used initial conditions from a spatially evolving simulation of flow past a sphere. The NW, NEQ and Q2D regimes in these simulations were found to be compatible with previous experimental results.

de Stadler & Sarkar (2012) performed a DNS to predict the effect of excess momentum (up to 40%) on an initially momentumless wake in a stratified fluid. They found that a propelled wake with small to moderate excess momentum causes small to moderate change in the wake development. This result was in contrast to

the result of Tennekes & Lumley (1972), derived on the basis of a self-similarity analysis that assumes constant eddy viscosity, that addition of even a small amount of excess momentum to the momentumless wake leads to a disproportionate change towards the longer life time of a towed wake. It is worth noting that the DNS of de Stadler & Sarkar (2012) showed that an eddy viscosity cannot parametrize vertical mixing in the stratified wake where the vertical transport of momentum is oscillatory in space and time. Also of interest is the role of mean flow instabilities in the evolution of the coherent structures in the Q2D regime. As discussed earlier, Meunier & Spedding (2006) found the momentumless wake to exhibit substantial differences during its development relative to the towed case. They also found that a propelled wake with net momentum as small as 2% of the body velocity momentum differs qualitatively from a momentumless wake.

From the preceding discussion of differences among numerical simulations, laboratory experiments and theory with respect to the evolution of self-propelled wakes, it is clear that the role of a canonical mean profile requires systematic study. These issues motivate us to examine a limiting situation where the mean velocity profile is removed from the initial velocity field while keeping the same initial turbulent fluctuations, and to compare the subsequent evolution of the turbulent patch with that of the original wake. Small-scale turbulence in the near-wake of a body can exhibit differences, for instance, because of differences in boundary layer characteristics. In order to ascertain the impact of the details of the near-wake turbulence, we also perform additional simulations with a different energy spectrum. Since all previous simulations of a stratified wake into the late wake stage have utilized a temporal approximation, we take the opportunity to relax this assumption and instead employ a spatially evolving model with prescribed conditions for near-wake turbulence at the inflow.

Section 2.2 provides the formulation, numerical method and the initial and boundary conditions employed in the problem. Section 2.3 describes the methods utilized to analyze the DNS data. Section 2.4 summarizes the evolution of a spatially evolving self-propelled wake and its comparison with a temporal simulation. Section 2.5 present the results from the the primary part of this work: comparison

among a spatially evolving self-propelled wake and turbulent patches with different spectra. Section 2.6 is an evaluation of the effect of increasing the amount of fluctuation energy residing in the small scales on the subsequent evolution of the self-propelled wake. Conclusions drawn from the present study are given in section 2.7.

2.2 Formulation

There are two ways of modeling the self-propelled turbulent wake computationally: in a frame where the flow statistics evolve temporally or in a frame where they evolve spatially. The temporally evolving model, universally adopted in past simulations of the stratified turbulent far-wake, approximates the spatially evolving model by neglecting the streamwise evolution of the mean velocity and is often made because the periodic boundary conditions that can then be used significantly lower the simulation time (equivalently computational cost) of calculating Reynolds averages. In the present paper, we will employ the spatially evolving model to understand the role of mean velocity profile and turbulent spectra. We will also show a comparison of results from one spatially evolving model of a self-propelled wake with those from a corresponding temporally evolving model. In the wake simulated here, the downstream distance x relative to the body in the spatially evolving model is related to time t in the temporally evolving model by $x = U_\infty t$ where U_∞ is the background velocity of the fluid. As in previous studies of the far-wake, the body and the details of boundary layer separation are not simulated.

2.2.1 Governing equations

The three dimensional conservation equations for mass, momentum and density subject to the Boussinesq approximation for an unsteady incompressible flow are

continuity:

$$\frac{\partial u_k^*}{\partial x_k^*} = 0, \tag{2.1}$$

momentum:

$$\frac{\partial u_i^*}{\partial t^*} + \frac{\partial (u_k^* u_i^*)}{\partial x_k^*} = -\frac{1}{\rho_0}\frac{\partial p^*}{\partial x_i^*} + \nu \frac{\partial^2 u_i^*}{\partial x_k^* \partial x_k^*} - \frac{\widetilde{\rho^*}}{\rho_0} g \delta_{i3}, \tag{2.2}$$

density:

$$\frac{\partial \rho^*}{\partial t^*} + \frac{\partial (u_k^* \rho^*)}{\partial x_k^*} = \kappa \frac{\partial^2 \rho^*}{\partial x_k^* \partial x_k^*}. \tag{2.3}$$

The * subscript denotes dimensional quantities. The density is decomposed into a background density, ρ_0, a linear variation in the x_3 direction, $\bar{\rho}^*(x_3)$ and a fluctuation, $\tilde{\rho}^*(x_i, t)$:

$$\rho^* = \rho_0 + \bar{\rho}^*(x_3) + \tilde{\rho}^*(x_i, t), \tag{2.4}$$

where $\bar{\rho}^*(x_3) + \tilde{\rho}^*(x_i, t) \ll \rho_0$. Density variation enters the momentum equation only through the buoyancy term. These equations are non-dimensionalized using U_∞ (the body velocity), D (the body diameter), $\rho_0 . C^* = \mid \partial \bar{\rho}^*(x_3)/\partial x_3^* \mid_{(t=0)}$ that denotes the constant vertical gradient of background density. The new non-dimensional variables are:

$$t = \frac{t^* U_\infty}{D}, \quad x_i = \frac{x_i^*}{D}, \quad u_i = \frac{u_i^*}{U_\infty}, \quad \rho = \frac{\rho^*}{\rho_0}, \quad \tilde{\rho} = \frac{\tilde{\rho}^*}{DC^*}, \quad p = \frac{\tilde{p}^*}{\rho_0 U^2}. \tag{2.5}$$

Substituting equation (2.5) into (2.1)-(2.3), we obtain the non-dimensionalized form as:

continuity:

$$\frac{\partial u_k}{\partial x_k} = 0, \tag{2.6}$$

momentum:

$$\frac{\partial u_i}{\partial t} + \frac{\partial (u_k u_i)}{\partial x_k} = -\frac{\partial p}{\partial x_i} + \frac{1}{Re}\frac{\partial^2 u_i}{\partial x_k \partial x_k} - \frac{1}{Fr^2}\widetilde{\rho}\delta_{i3}, \tag{2.7}$$

density:

$$\frac{\partial \rho}{\partial t} + \frac{\partial (u_k \rho)}{\partial x_k} = \frac{1}{RePr}\frac{\partial^2 \rho}{\partial x_k \partial x_k}. \tag{2.8}$$

The relevant non-dimensional parameters are as follows: the Reynolds number, $Re = U_\infty D/\nu$, the Prandtl number, $Pr = \nu/\kappa$, and the body Froude number, $Fr = U_\infty/(N^* D)$ where N^* is the $Brunt - V\ddot{a}is\ddot{a}l\ddot{a}$ frequency or buoyancy frequency defined as $N^* = [-gC^*/\rho_0]^{1/2}$. The non-dimensional buoyancy frequency is $N \equiv Fr^{-1}$. Equations (2.6)-(2.8) are solved using DNS to capture the full dynamic range of velocity and density fields.

2.2.2 Numerical scheme and simulation parameters

Results from the different cases listed in table 2.1 will be discussed in detail. The self-propelled wake, case SP50, was simulated using both the temporally evolving model and the spatially evolving model. The turbulent patch (cases TP1 and TP2) was simulated using the spatially evolving model. A fractional step method is used for integrating the Navier-Stokes equation as briefly described by Brucker & Sarkar (2010) and de Stadler & Sarkar (2012). Brucker & Sarkar (2010) and de Stadler & Sarkar (2012) used Red-black Gauss-Seidel method as a smoother for the multigrid method for solving the Poisson equation for pressure whereas in this study we use the same smoother with successive over relaxation (SOR) (Yavneh, 1996) to accelerate the convergence of the pressure Poisson equation on stretched grids in all three directions.

The temporally evolving model

The computational domain has dimensions of $102.5 \times 19.75 \times 12.31$ (excluding the sponge region in x_2 and x_3) with mesh size of $2048 \times 384 \times 256$. A constant

$\Delta x_1 = 0.05$ is used in the streamwise direction. A value of $\Delta x_2 = 0.031$ is used for the central lateral region ($-2 < x_2 < 2$), followed by a block with 10 points that blends into a grid with 1.25% stretching, $\Delta x_{2,min} = 0.0326$ and $\Delta x_{2,max} = 0.14$. The central vertical region, $-1 < x_3 < 1$, has a uniform grid with $\Delta x_3 = 0.031$, followed by a block with 10 points that blends into a grid with 1.5% stretching, $\Delta x_{3,min} = 0.0326$ and $\Delta x_{3,max} = 0.12$. Periodic boundary conditions are imposed in the streamwise direction and far field boundary conditions in the spanwise and cross stream direction. After the initial velocity is imposed as described below, the Navier-Stokes equations are advanced in time.

The initial mean velocity profile used for the self-propelled wake cases SP50 and SP10, is identical to the canonical momentumless profile with positive and negative velocity lobes used in the previous work (Brucker & Sarkar, 2010; de Stadler & Sarkar, 2012). The defect velocity, U_0 for case SP50 is 0.3 whereas for case SP10, $U_0 = 0.11$, implying that SP50 has $\sim 50\%$ mean kinetic energy of the total in comparison to $\sim 10\%$ in SP10. As in our previous work, the initial velocity fluctuations are allowed to evolve during an adjustment period while the mean velocity profile is held fixed until the maximum value of $\langle u_1' u_r' \rangle / K \simeq -0.25$, signifying that the cross-correlation has increased to a level typical of turbulent shear flow. The velocity fluctuations at the beginning of the adjustment period are generated as an isotropic divergence-free velocity field in spectral space (Rogallo (1981)) which satisfies the spectrum given by

$$E(k) = (k/k_0)^4 e^{-2(k/k_0)^2}. \tag{2.9}$$

In order to localize the initial turbulence, the fluctuating velocity field u_i' is multiplied by a radial damping function function defined as

$$g(r) = a \left[1 + \left(\frac{r}{r_0} \right)^2 \right] e^{-\frac{1}{2}\left(\frac{r}{r_0}\right)^2}, \tag{2.10}$$

where $a = 0.055$ is the maximum initial value of the fluctuation at the centerline, $r = \sqrt{x_2^2 + x_3^2}$ and $r_0 = 0.5$ (half the body diameter).

The spatially evolving model

The computational domain has dimensions of $240.38 \times 19.75 \times 12.31$ (excluding the sponge region in x_2 and x_3) with mesh size of $4096 \times 384 \times 256$. We choose the mesh size so that the turbulence energy spectrum is well resolved over the entire domain for all the cases.The streamwise grid is as follows: $\Delta x = 0.045$ until $x_1 = 40$, a 15-point blending region, a stretched grid until $x_1 = 190$ with $\Delta x_{1,min} = 0.0451$ and $\Delta x_{2,max} = 0.0757$ and, finally, a uniform grid with $\Delta x = 0.0757$. The x_1 grid stretching of 0.02% is mild. The grid spacings in the lateral and vertical directions are identical to those in the temporal model.

For the spatially evolving simulations, inflow-outflow boundary conditions are used in the streamwise direction. An auxiliary simulation generates the flow that is advected into the domain at the inflow boundary. The computational domain for the auxiliary simulation is identical to that employed for the temporally evolving model. The fluctuations for case SP50 are initialized, utilizing divergence-free initial conditions followed by an adjustment to mean shear, as explained in section 2.2.2. An additional time period of 1.2 D/U_∞ allows for development of buoyancy effects. The turbulent patch cases, TP1, TP2 and TP10, have a constant background flow without shear. The initial velocity fluctuations for the auxiliary simulations in cases TP1 and TP10 are generated by choosing $k_0 = 4$ and by taking $k_0 = 8$ for TP2, in (3.2), followed by spatial localization using (3.3). Equations (2.6)-(2.8) are solved in their unstratified form for the turbulent patch TP1 for a sufficient amount of time so that its energy spectrum B evolves so as to match the energy spectrum of the self-propelled wake, SP50 (analogous procedure is followed for SP10 and TP10). During this period of adjustment, the spatial profile of the fluctuations is kept fixed. The other turbulent patch simulation, TP2, is also adjusted in a similar manner as TP1 until higher energy is accumulated at smaller scales owing to nonlinear transfer. The initial velocity fluctuations and the initial energy spectrum after the end of the adjustment period for SP50, TP1 and TP2 are shown in figure 2.1(a) and (b), respectively. Spectrum A is for SP wake with 50% MKE, spectrum B is for turbulent patch TP1, spectrum is C for TP2, spectrum D is for SPwake with 50% MKE and has the same spectrum as TP2.

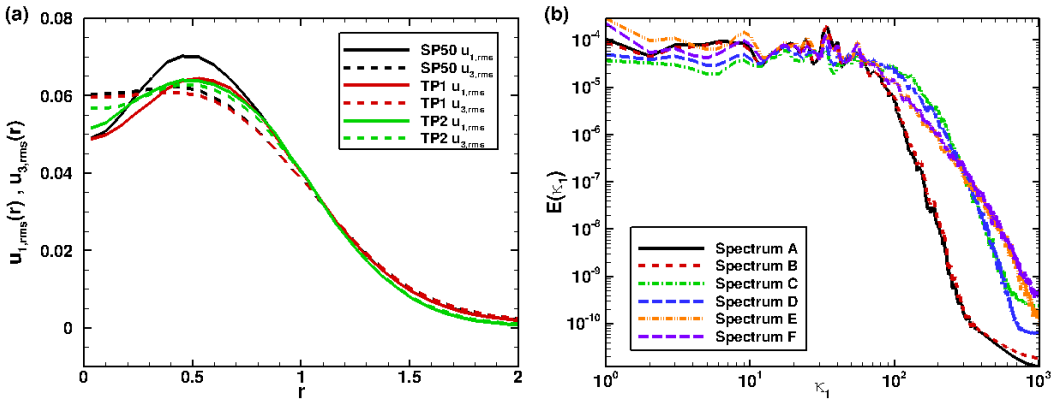

Figure 2.1: (a) Radial profiles of streamwise (u_1) and vertical (u_3) $r.m.s.$ velocity, $u_{2,rms}$ matches $u_{3,rms}$. (b) *Initial* energy spectra for various cases.

Two-dimensional (x_2 and x_3) data planes generated from the auxiliary simulation are advected into the domain to provide inflow conditions. Successive planes from the auxiliary simulation are taken to be the inflow plane of the spatially evolving simulation at successive times with $\Delta t = \Delta x_{auxiliary}/U_\infty$.

The simulation in the spatially evolving domain is initialized as follows: SP50 with a mean wake profile and divergence-free fluctuations, and TP1 and TP2 with divergence-free fluctuations. At the outflow, an extrapolation boundary condition is used for u, v, w and ρ and a homogeneous Neumann boundary condition is used for pressure. The extrapolation boundary condition uses 2^{nd} order extrapolation to extrapolate the value of the flow variables from the interior of the domain to the outflow boundary, i.e., $\phi^n_{i+1} = 2\phi^n_i - \phi^n_{i-1}$, where 'i' is the x-coordinate index and 'n' is the time-level.

In order to control spurious reflections from internal gravity waves and other disturbances propagating out of the domain, we use sponge regions near the x_2 and x_3 boundaries, where damping functions gradually relax the value of the variable to its corresponding value at the boundary. These damping functions are added on the right hand side of equations (2.7) and (2.8) as explained in Brucker & Sarkar (2010). Note that no sponge layer is used at the outflow as it has been found that the extrapolation boundary condition is sufficient in the present flow to propagate any disturbances out of the domain smoothly. At the spanwise (x_2) and vertical

Table 2.1: Parameters for the simulations.

Case	N_1	L_1	k_0	*Spectrum*	*Simulation type*
1. SP50	4096	240.38	4.0	A	Spatial
2. TP1	4096	240.38	4.0	B	Spatial
3. TP2	4096	240.38	8.0	C	Spatial
4. SP50	2048	102.5	4.0	A	Temporal
5. SP50C	2048	102.5	7.0	D ($\sim$ C)	Temporal
6. SP10	4096	240.38	4.0	E	Spatial
7. TP10	4096	240.38	4.0	F	Spatial

(x_3) boundaries of the sponge region, far-field boundary conditions are used:

$$\frac{\partial u_i}{\partial x_2} = 0 \quad (x_2 = \pm L_2/2), \quad \frac{\partial u_i}{\partial x_3} = 0 \quad (x_3 = \pm L_3/2), \tag{2.11}$$

$$p = 0 \quad (x_2 = \pm L_2/2), \quad p = 0 \quad (x_3 = \pm L_3/2), \tag{2.12}$$

$$\frac{\partial \rho}{\partial x_2} = 0 \quad (x_2 = \pm L_2/2), \quad \frac{\partial \rho}{\partial x_3} = -\frac{\rho_0 C^*}{D} \quad (x_3 = \pm L_3/2). \tag{2.13}$$

2.2.3 Simulation parameters

SP50 denotes the self-propelled wake with 50% mean kinetic energy and energy spectrum A, TP1 denotes the turbulent patch with spectrum B and TP2 denotes the turbulent patch with spectrum C. Case SP10 is a self-propelled wake with 10% mean kinetic energy and case TP10 corresponds to a turbulent patch with a similar energy spectrum (spectra E and F respectively). Cases TP1, TP2 and TP10 do not have a initial mean velocity profile. N_1, N_2 and N_3 represents the number of grid points in the x_1, x_2 and x_3 directions respectively. $N_2 = 384$ and $N_3 = 256$ for all the present cases. L_1, L_2 and L_3 are the length of the domain excluding the sponge region in the respective directions. $L_2 = 19.75$ and $L_3 = 12.31$ for all the present simulations. Spectra A and B are approximately the same. Spectra C and D are similar and have more energy in the small scales as compared to A and B as shown in figure 2.1(b). The Reynolds number Re, the

Froude number Fr and the Prandtl number Pr for all the cases are $15000, 3$ and 1 respectively.

Table 2.1 shows the simulation parameters for this study. The wake is simulated up to $x_1 \sim 240$, equivalently $Nt \sim 80$. Approximately 400 million grid points are used for the simulations. A three-dimensional domain decomposition method is used to distribute the sub-domains into 96 and 192 processors for the auxiliary and main simulations respectively. Exchange of the data between the processors is performed through the message passing interface (MPI) library. The main simulations required approximately 20 000 CPU h on a Cray XE6.

Note that a temporal simulation is additionally performed for SP50 to compare with is spatial counterpart. The dimensions of the computational domain and the mesh size for this simulation is the same as that of the auxiliary simulation for the generation of the inflow boundary condition.

2.3 Data analysis method

Since we are computing a spatially evolving stratified wake, we have inhomogeneous boundaries in every direction. Therefore spatial averaging of the variables in a particular direction, as can be done for temporally evolving simulations, is infeasible. We perform temporal averaging of the variables for calculating the statistics. The simulations are run for a sufficiently long time $(1.5L_1/U_\infty)$ to reach a statistically homogeneous state for performing a temporal averaging as follows

$$\langle \phi(x_1, x_2, x_3) \rangle = \frac{1}{T_2 - T_1} \int_{T_1}^{T_2} \phi(x_1, x_2, x_3, t) dt \tag{2.14}$$

where the angle brackets represents temporal averaging, T_1 is the start and T_2 is end of time averaging and $T_2 - T_1$ is $\sim 0.8L_1/U_\infty$. The Reynolds decomposition of the flow variables is

$$u_i = \langle u \rangle + u_i^{'}, \quad \rho = \langle \rho \rangle + \rho^{'}, \quad p = \langle p \rangle + p^{'}. \tag{2.15}$$

The integrated turbulent kinetic energy, $TKE = \int_A \langle u_i^{'} u_i^{'} \rangle / 2 dA$, is a measure of the kinetic energy of the fluctuations. The evolution of the pointwise turbulent kinetic energy, $K = \langle u_i^{'} u_i^{'} \rangle / 2$ is given by

$$\frac{DK}{Dt} = P + B - \varepsilon - \frac{\partial T_i}{\partial x_i}, \tag{2.16}$$

where P is the production is given by

$$P = -\langle u_i^{'} u_j^{'} \rangle \frac{\partial \langle u_i \rangle}{\partial x_j}, \tag{2.17}$$

and ε is the turbulent dissipation rate given by

$$\varepsilon = \frac{2}{Re} \langle s_{ij}^{'} s_{ij}^{'} \rangle, \qquad s_{ij}^{'} = \frac{1}{2} \left(\frac{\partial u_i^{'}}{\partial x_j} + \frac{\partial u_j^{'}}{\partial x_i} \right). \tag{2.18}$$

Here, $\partial T_i / \partial x_i$ is the turbulent transport and is defined as

$$T_i = \frac{1}{2} \langle u_i^{'} u_j^{'} u_j^{'} \rangle - \langle u_i^{'} p^{'} \rangle - \frac{2}{Re} \langle u_j^{'} s_{ij}^{'} \rangle, \tag{2.19}$$

while B, the buoyancy flux that transfers energy between the turbulent kinetic and potential energy modes, is given by

$$B = -\frac{1}{Fr^2} \langle \rho^{'} u_3^{'} \rangle. \tag{2.20}$$

For the comparison of the wake dimensions, we calculate the wake thickness in the horizontal and vertical based on the wake kinetic energy. The horizontal thickness, R_{E2} is obtained by fitting a Gaussian profile to the horizontal variation of KE and computing its width at 1% of the maximum, centerline value. The variation in the vertical is more complex with auxiliary off center lobes and, therefore, the vertical thickness is calculated by using a second central spatial moment of the KE in the vertical direction as done by Brucker & Sarkar (2010).

$$R_{X\alpha}^2 = A_1 \frac{\int_A (x_\alpha - x_\alpha^c)^2 (X) dA}{\int_A (X) dA}. \tag{2.21}$$

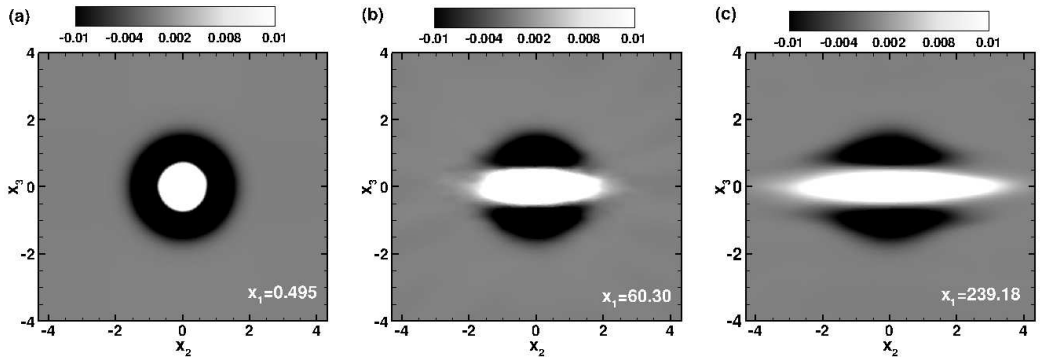

Figure 2.2: Mean velocity contours for the self propelled wake (SP50) at various x_1 locations. Case SP50.

Here, $x_\alpha^c(t) = \frac{\int_A (x_\alpha)(X)dA}{\int_A (X)dA}$, $A_1 = 2$ is a normalization factor to set the initial wake dimensions, A is the area of the $x_2 - x_3$ plane excluding the sponge region and $\alpha = 3$. The choice of $X = \langle u_i \rangle \langle u_i \rangle / 2 + \langle u_i' u_i' \rangle / 2$ corresponds to spatial extent of wake kinetic energy.

The energy flux radiated to the background by internal waves is given by

$$T_p = \int_C \langle p' u_n' \rangle dC, \tag{2.22}$$

where C denotes the closed curve corresponding to the $x_2 - x_3$ plane excluding the sponge region and u_n' is the velocity fluctuation in the direction normal to the boundary.

2.4 Summary of a spatially evolving self-propelled wake

As mentioned in section 2, we perform a spatial simulation of a stratified wake with specified turbulent inflow conditions. The stratified wake consists of various flow regimes whose duration is typically given in terms of buoyancy period, Nt. The period $Nt < 2$ is the near wake region (NW) where the wake evolves as an unstratified flow. The regime $2 < Nt \approx 50$ is the non-equilibrium regime (NEQ), which is further split into an accelerated collapse (AC) region,

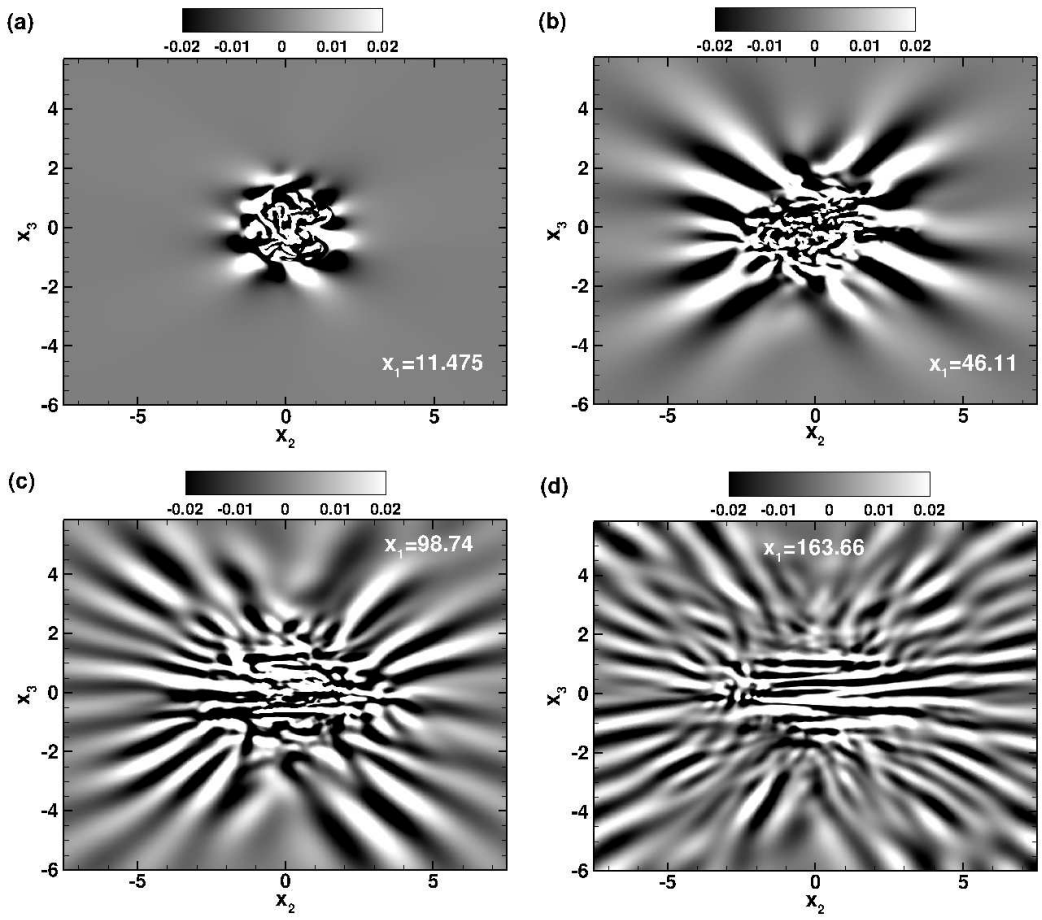

Figure 2.3: Internal gravity wave field visualized by snapshots of ω_1 at various x_1 locations. Multiple horizontal layers, a manifestation of the dislocations between pancake eddies, can also be seen in (d). Case SP50.

$2 < Nt < 7$, and a transition region, $7 < Nt \approx 50$. The $Nt > 50$ regime is referred to as the quasi-two dimensional ($Q2D$) stage of the late wake. In the NW regime, the wake expands in both x_2 and x_3 directions mixing up the background density field by displacing heavy fluid up and light fluid down. When the wake enters the AC regime,the stabilizing effect of buoyancy becomes significant and the kinetic energy is sustained at the expense of the potential energy. The density perturbations are no longer supported by the kinetic energy, due to which the fluid seeks equilibrium and the flow is suppressed in the vertical direction whereas in the lateral direction, the wake expands. This effect also slows down the decay of the horizontal mean velocity and radiates energy in the form of internal gravity waves into the background. Figure 2.2 illustrates the contours of the evolution of the mean velocity $\langle u_1 \rangle (x_2, x_3)$ at various x_1 locations. Figure 2.2(a) shows the initial mean velocity profile with the presence of initially axisymmetric positive velocity lobes (thrust lobes) and negative velocity lobes (drag lobes) whereas figures 2.2(b) and (c) depict the subsequent anisotropic growth of the wake that occurs primarily in the horizontal direction. The negative velocity lobes eventually vanish in the horizontal direction but remain in the vertical direction over the entire downstream extent. The reason for the survival of the negative lobes is the effect of buoyancy that inhibits vertical mixing of momentum.

Internal gravity waves carry horizontal vorticity. The wave field associated with the self-propelled wake is shown via the contours of ω_1 in figure 2.3 at various downstream locations. In addition, Figure 2.3(d) shows that, at late time, the central region of the wake has multiple coherent layers of streamwise vorticity. These correspond to regions of large vertical shear between adjacent pancake eddies.

Figure 2.4 shows the instantaneous vertical vorticity field at the center-plane in the horizontal direction. Small vortices merge to form large vortices in the downstream directions. These vortices ultimately take the form of coherent pancake eddies as shown in earlier laboratory experiments and temporally evolving simulations. The frequency spectra at various downstream locations is shown in figure 2.5. Kolmogorov scaling (ω^{-2}) is found over a short range of wavenumbers at the locations $x_1 = 2.25, 47.36$ and 98.91; however, spectra at locations further

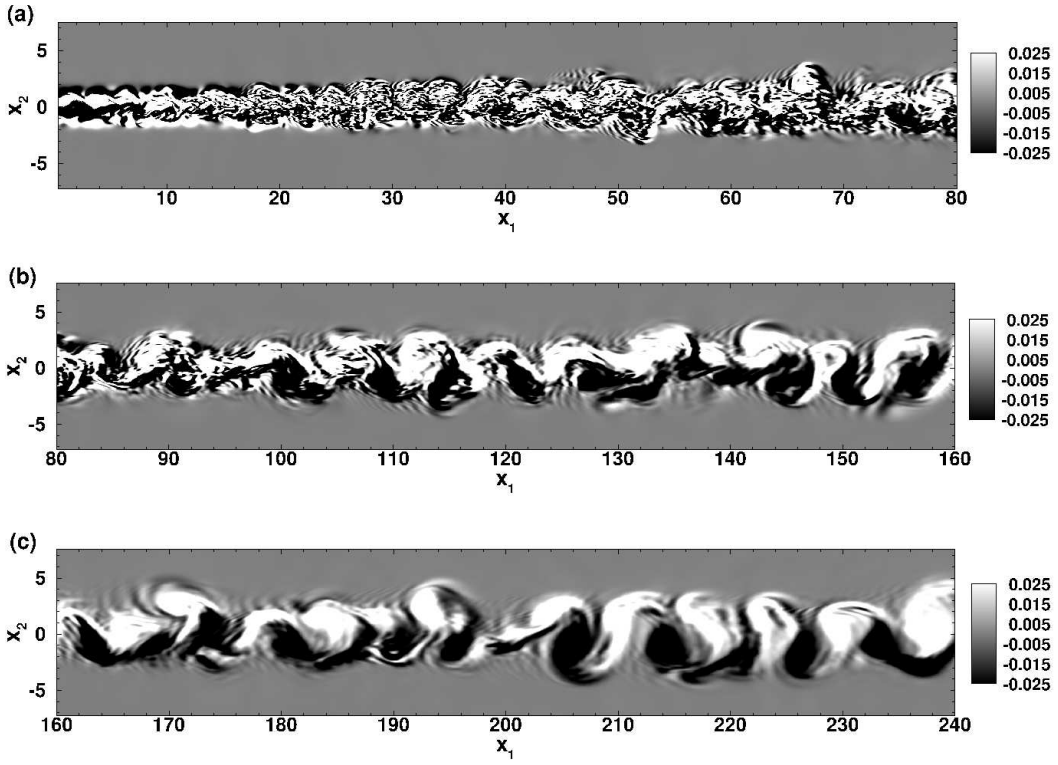

Figure 2.4: Instantaneous ω_3 at the horizontal centerplane, $x_3 = 0$ (a) $0 < x_1 < 80$, (b) $80 < x_1 < 160$, (c) $160 < x_1 < 240$. Case SP50.

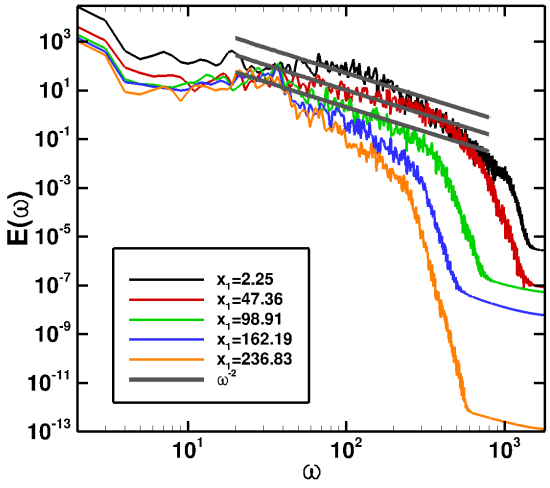

Figure 2.5: Frequency spectra at various downstream locations. Case SP50.

downstream with lower turbulent Reynolds number exhibit a decay faster than ω^{-2}.

Figures 2.6 (a) and (b) show Reynolds stresses, $\langle u_1' u_2' \rangle$ and $\langle u_1' u_3' \rangle$, respectively, at the location $x_1 = 75.18$. The horizontal fluctuations have a Reynolds stress, $\langle u_1' u_2' \rangle$, that is antisymmetric and with a sign (positive/negative) consistent with co-gradient turbulent transport by the mean velocity. However, $\langle u_1' u_3' \rangle$ shows little coherence with the mean field. The spatial evolution of $\langle u_1' u_3' \rangle$ also exhibits a rapid decrease followed by oscillation around a value of zero. The faster decay of $\langle u_1' u_3' \rangle$ relative to $\langle u_1' u_2' \rangle$ occurs because buoyancy inhibits the magnitude of vertical fluctuations as well as their correlation with horizontal fluctuations, whereas the mean velocity shear in the horizontal plane is able to maintain $\langle u_1' u_2' \rangle$ that is associated with fluctuations that are not directly affected by buoyancy. This behavior of the Reynolds shear stresses is similar to that found by Jacobitz & Sarkar (1998) in uniform shear flow who examined the effect of changing the inclination of mean shear plane so that the ratio of vertical mean shear to horizontal mean shear progressively changed from unity to zero. However, there is an important difference with the previously studied situation with uniform shear. The follow up study of Jacobitz & Sarkar (1999) found that the growth rate of the turbulent kinetic energy in the case of horizontal mean shear decreased with increasing gradient Richardson number, Ri, as in vertically sheared flow until, at a critical Richardson number $Ri_{cr} \sim 1.5$, the kinetic energy of fluctuations asymptotically decayed to zero instead of growing. In contrast, the inflectional nature of the mean horizontal shear in the present case of a wake ensures that shear instabilities continually maintain velocity fluctuations.

2.4.1 Comparison between a spatially and a temporally evolving self-propelled wake

The validity of the temporally evolving approximation given an initial field corresponding to a spatially evolving model is of interest. Therefore, we simulate the SP50 case with a temporally evolving model and compare the various statistics from the two simulations in figure 2.7. Results for the temporal simulation are

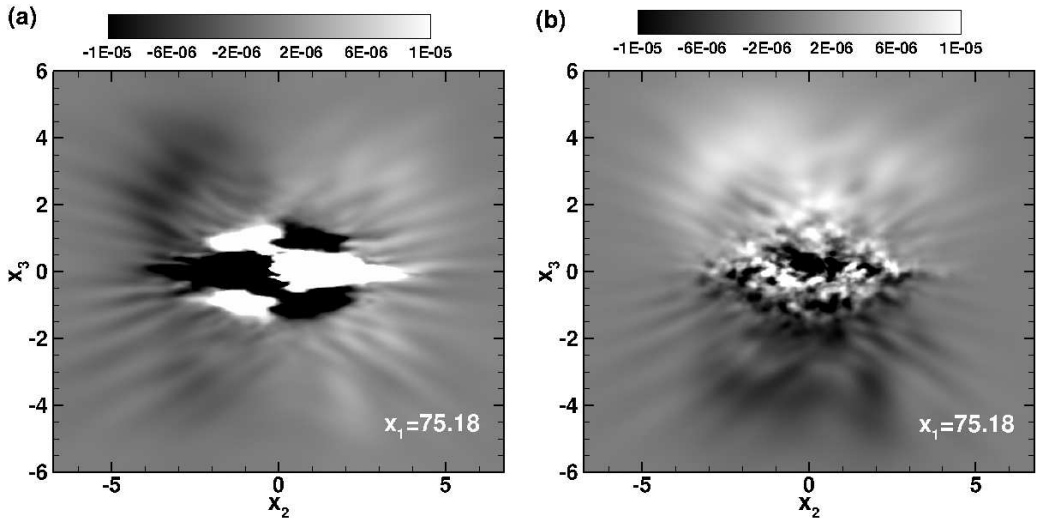

Figure 2.6: Reynolds stresses (a) $\langle u_1' u_2' \rangle$, (b) $\langle u_1' u_3' \rangle$. Case SP50.

plotted as a function of time, t, and for the spatial simulation as a function of x_1. The simulations have a virtual origin of $t = 7$ and $x_1 = 7$, based approximately on measured turbulence levels in wakes. The waveflux and the integrated production (figures 2.7 (c) and (d), respectively) between the spatial and temporal simulations are similar. Although there is similarity in the behavior of the integrated dissipation (figure 2.7 (d)) between both types of simulations, there are some differences which could be due to the somewhat higher grid spacing (owing to grid stretching) in the spatial simulation. Figure 2.7(e) shows that the buoyancy flux is similar between the temporal and spatial models. We also observe a similar distribution of waves and vortical structures (not shown) in contour plots.

2.5 Comparison between a spatially evolving self-propelled wake and a patch of turbulence

The initial energy spectra used for the simulations of a self-propelled wake with 50% MKE and the turbulent patches were shown in figure 2.1(b). Comparison between case SP50 (with mean shear) and case TP1 (without mean shear but with inlet turbulence similar to SP50) allows us to make precise the role of mean

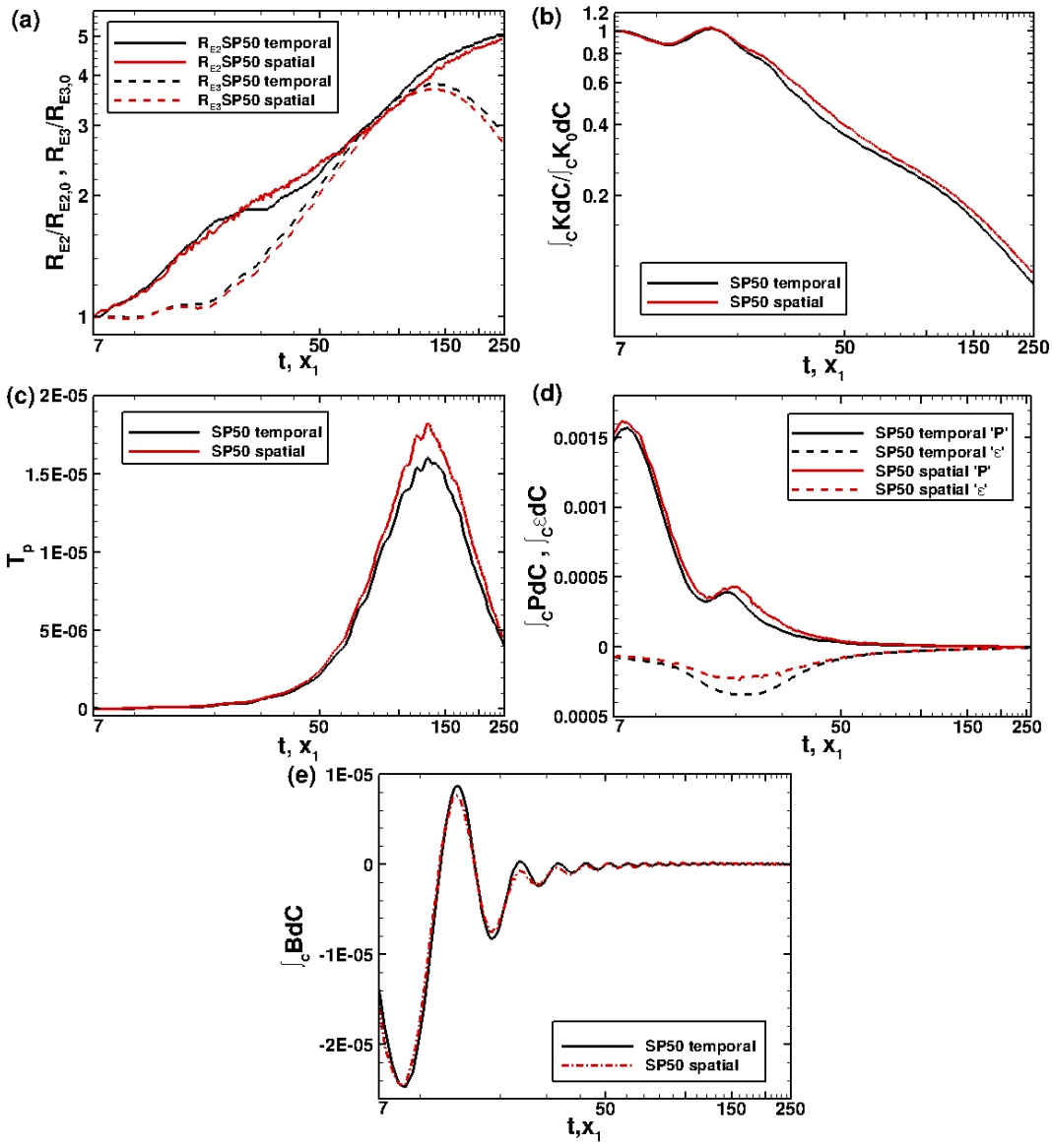

Figure 2.7: Comparison between temporal and spatial simulations: (a) Wake dimensions, (b) Integrated turbulent kinetic energy, (c) Waveflux, (d) Integrated production and dissipation, (e) Integrated buoyancy flux.

shear in the flow evolution while comparison between case TP1 and TP2 (different energy spectrum with more small-scale contribution) allows us to explore the influence of initial fluctuations in the near wake.

Figure 2.8 show the evolution of the integrated TKE normalized by its inlet value for different cases. It can be observed that the integrated TKE of SP50 exhibits an initial decay that is small relative to TP1 & TP2. This difference occurs because of the presence of shear production of TKE in case SP50 that extracts energy from the mean and transfers it into the fluctuations. The production not only restrains the TKE from decaying during the initial stages but increases it until $x_1 \sim 18$. As the production starts decreasing, the extraction of energy from the mean decreases and the TKE in case SP50 also starts decaying. Note that the shear production is identically zero in the TP cases. The decay of TKE in cases SP10 and TP10 (they are the analogous cases to SP50 and TP1, i.e., SP10 has 10% MKE and TP10 has the same initial spectrum as SP10) as shown in figure 2.8 are found to be almost similar in contrast to the differences between SP50 and TP1. The reason for the similar decay of TKE between cases SP10 and TP10 is the small percentage of MKE in SP10, which leads to a smaller production than in SP50 and, therefore, a smaller counter to dissipative effects on TKE.

After the slight initial decay of TKE in SP50, it increases up to a peak value and starts decaying again as seen in figure 2.8. We see an increase in integrated TKE as well for TP1 but the increase is not as large as SP50. This increase of the TKE in case TP1 is due to the buoyancy flux being positive at this time as shown in figure 2.10 (b). The TKE in case TP2 decays in a similar manner as in TP1 up to $x_1 \sim 11$, but instead of an increase at $x_1 \sim 11$ the TKE decays at a slower rate because of the positive buoyancy flux.

Figure 2.9(a) shows the evolution of integrated production (already discussed) and integrated dissipation. Case TP2 has larger turbulent dissipation rate relative to SP50 and TP1 because of the higher small-scale energy content. Going downstream, the turbulent dissipation for SP50 increases, increases slightly for TP1 and decreases for TP2. The increase in the dissipation of SP50 is due to the transfer of energy from the mean shear into the fluctuating components. The

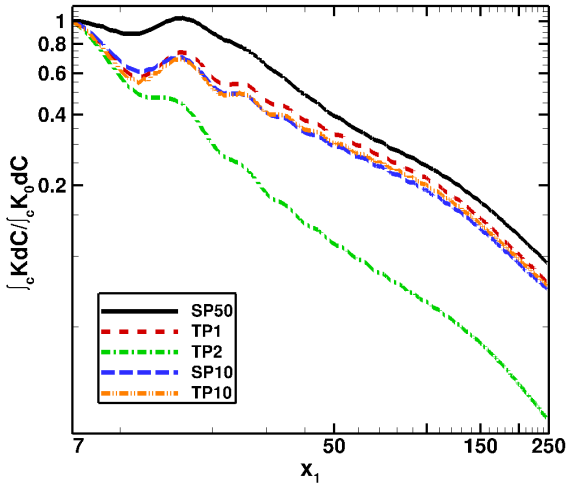

Figure 2.8: Integrated turbulent kinetic energy SP50, TP1, TP2, SP10 and TP10.

dissipation increases until $x_1 \sim 20$, as the production and buoyancy flux achieves a second peak value at the same location. For $x_1 > 20$ both the production and dissipation decrease in case SP50. The components of integrated production, P_{12} and P_{13}, are shown in figure 2.9(b). P_{12} decreases monotonically but remains positive whereas P_{13} decreases and becomes negative at $x_1 \sim 16$. For $x_1 > 16$, P_{13} increases to a positive value and then decreases again to a negligible value. Recall that the mean velocity contours of figure 2.2 shows that the initial lobes of negative velocity disappeared in the horizontal axis but were maintained in the vertical axis. The reason is that P_{12} (always positive) is able to continuously extract energy from the mean shear to fluctuations and continuously reduce the mean shear in the horizontal x_2 direction. P_{13}, on the other hand, extracts energy from the vertical mean shear initially but then returns a part of the extracted energy to the mean, and eventually oscillates between positive and negative values with little mixing of momentum. At the end there is a residual of mean energy thus maintaining the negative lobes in the vertical profile of mean velocity.

Figures 2.10(a) and (b) show the x_1 and x_3 component of the integrated TKE and the integrated buoyancy flux, respectively. There is oscillatory behavior of integrated K_{33} and buoyancy flux in all the cases owing to the reversible exchange between potential and kinetic energy in stratified flow. We also find

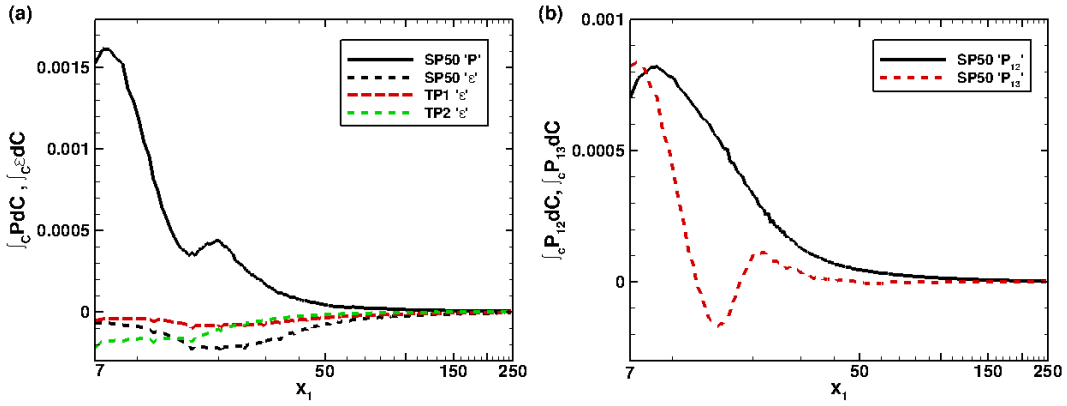

Figure 2.9: (a) Production and dissipation integrated over the cross-section area. Note that production is identically zero for TP1 and TP2, (b) Components of production integrated over the cross-section area.

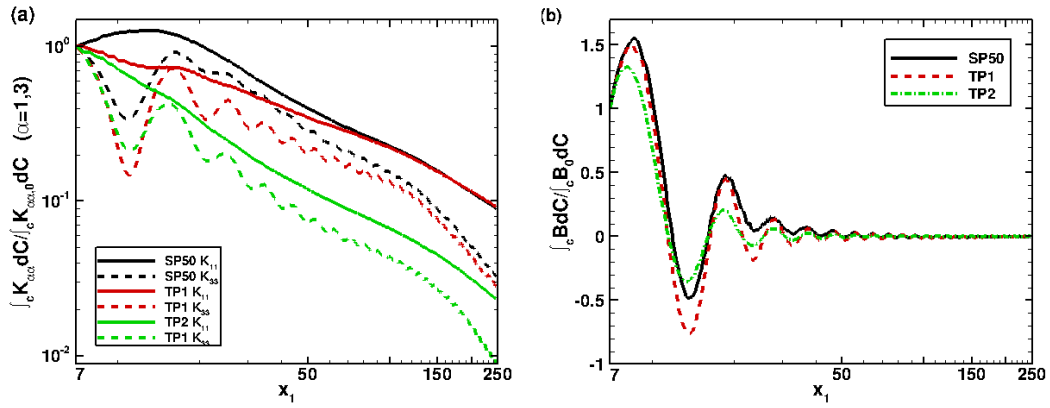

Figure 2.10: (a) x_1 and x_3 component of integrated $t.k.e$, (b) Integrated buoyancy flux.

from figure 2.10 (a) that K_{11} increases for SP50 in the near wake and decays at downstream locations whereas for TP1 and TP2 it decreases monotonically from the initial value. The rate of decay of K_{11} in case TP2 is steeper than for TP1. K_{22} (not shown here) behaves identically as K_{11} for TP1 and TP2, but for SP50 it shows a smaller increase at initial stages and slower rate of decay at later stages as compared to K_{11}. The oscillations in the vertical component, K_{33}, lead to an increase in the integrated TKE of SP50 and TP1 in the initial stages as was evident from figure 2.8(b). Figure 2.10(a) shows that K_{33} decreases by almost 50% before it regains the initial value at $x_1 \sim 18$. This is supported by the large values of the integrated buoyancy flux in the near wake as shown in figure 2.10(b).

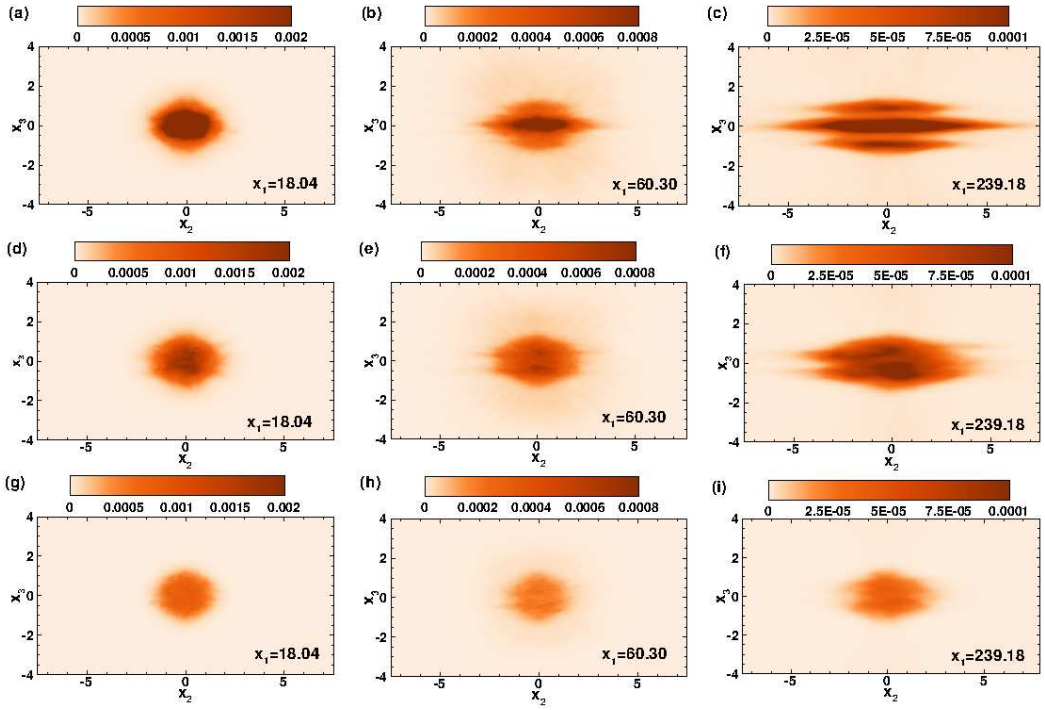

Figure 2.11: Evolution of TKE contours at different locations for various cases. The top row (a, b and c) correspond to the self propelled wake with 50% mean (SP50), the middle row (d, e and f) to TP1, and the bottom row (g, h, i) to TP2.

Figure 2.11 show contours of the TKE of the self-propelled wake with 50% mean and the two patch-of-turbulence cases with different spectra at various x_1 locations. At $x_1 \simeq 18$, the distribution of TKE is already different among cases. The shear production transfers energy into the fluctuating components of velocity in case SP50 and therefore we see a higher concentration of TKE in the core of the SP50 case (figure 2.11(a)) as compared to TP1 and TP2 (figures 2.11(d) and (g)). The difference in the TKE between cases TP1 and TP2 is due to the higher initial dissipation rate of TP2. As we move downstream, the TKE in SP50 expands preferentially in the horizontal direction because of entrainment that is not directly inhibited by buoyancy. TKE in case TP1 decays in a manner that is qualitatively similar to SP50 whereas in case TP2 the TKE decays much faster.

This can again be related to the fact that the dissipation of TP2 is higher than SP50 and TP1 initially and there is no energy transfer into the fluctuations because of the lack of mean shear. The distinctive feature of SP50 relative to TP1

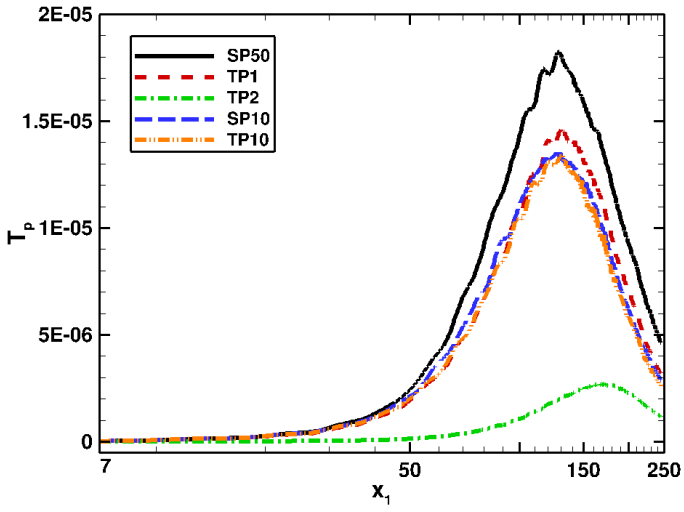

Figure 2.12: Internal wave flux for SP50, TP1, TP2, SP10 and TP10.

and TP2 is the presence of lobes in the vertical direction as shown in figures 2.11 (c), (f) and (i). The presence of lobes can be explained in a similar manner as done earlier for the presence of the negative lobes in the mean velocity profile. The reversible energy transfer by P_{13} leaves fluctuating energy lobes in the vertical direction as residual.

The evolution of internal wave flux is shown in figure 2.12. We notice that SP50 shows a higher wave flux compared to TP1, whereas TP2 has a substantially smaller wave flux amongst all of the cases. This happens because the flow in case SP50 inherits more TKE than TP1 which in turn has higher TKE than TP2 as depicted in figure 2.8(a). The higher the fluctuation energy in the core of the wake, the higher will be the energy propagated into the background during the suppression of the wake growth in the vertical direction. Furthermore, TP2 has less energy in the low-wave numbers that drive the wave flux. SP10 and TP10 show similarity in the evolution of wave flux. Higher values of TKE in SP50 leads to higher waveflux as compared to SP10.

Figures 2.13 (a) and (b) represent the evolution of wake dimensions in the horizontal and the vertical directions calculated using the total kinetic energy. The variation in the lateral direction is well-fitted by a Gaussian profile whose radius, R_{E2}, is computed based on the 1% of maximum, centerline value. The variation

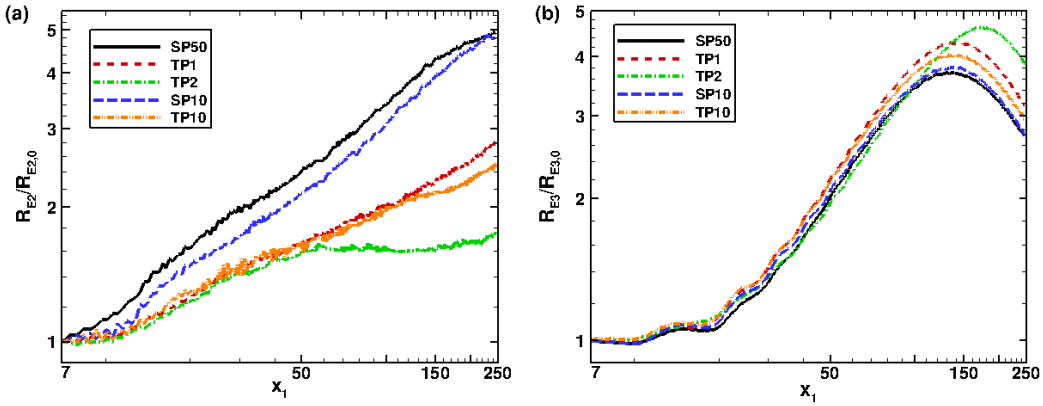

Figure 2.13: Wake dimensions based on the kinetic energy for SP50, TP1, TP2, SP10 and TP10: (a) Wake width, (b) Wake height.

of kinetic energy in the vertical direction exhibits auxiliary peaks on each side in addition to the central peak. Therefore, the vertical radius, R_{E3}, is calculated using equation (4.10), an expression based on the second central moment of the kinetic energy. The horizontal wake thickness expands at different rates that decreases from SP50 to TP1 to TP2. Similarly, the horizontal wake thickness is lower in TP10 relative to SP10. At further downstream locations, the expansion of case TP2 in the horizontal direction is very small relative to the other cases. A possible reason is that the coherence of the vertically oriented late-wake vortices is much less in TP1 as will be shown shortly. The vertical thickness, R_{E3}, does not increase intially because buoyancy suppresses turbulent entrainment. After $x_1 \sim 30$, the vertical thickness exhibits an increase in cases SP50 and TP1 up to $x_1 \sim 130$ and until $x_1 \sim 180$ in case TP2. All cases show an eventual contraction in the vertical thickness, an unusual occurrence in turbulent flows. The increase in R_{E3} occurs because the fluctuation energy deposit in the regions adjacent to the wake core by the internal wave flux. But eventually the wave flux decreases leading to the downstream decrease in R_{E3}. We note that the increase and subsequent decrease of R_{E3} occurs because of the choice of KE (dominated by fluctuation KE) to evaluate the vertical extent of the wake. For instance, R_3 in the wake (case SP50) based on the mean velocity shows little increase in the downstream direction.

The spatial structure of the internal wave field is similar between the two turbulent patch cases shown in figure 2.14 and similar to that for the SP50 case

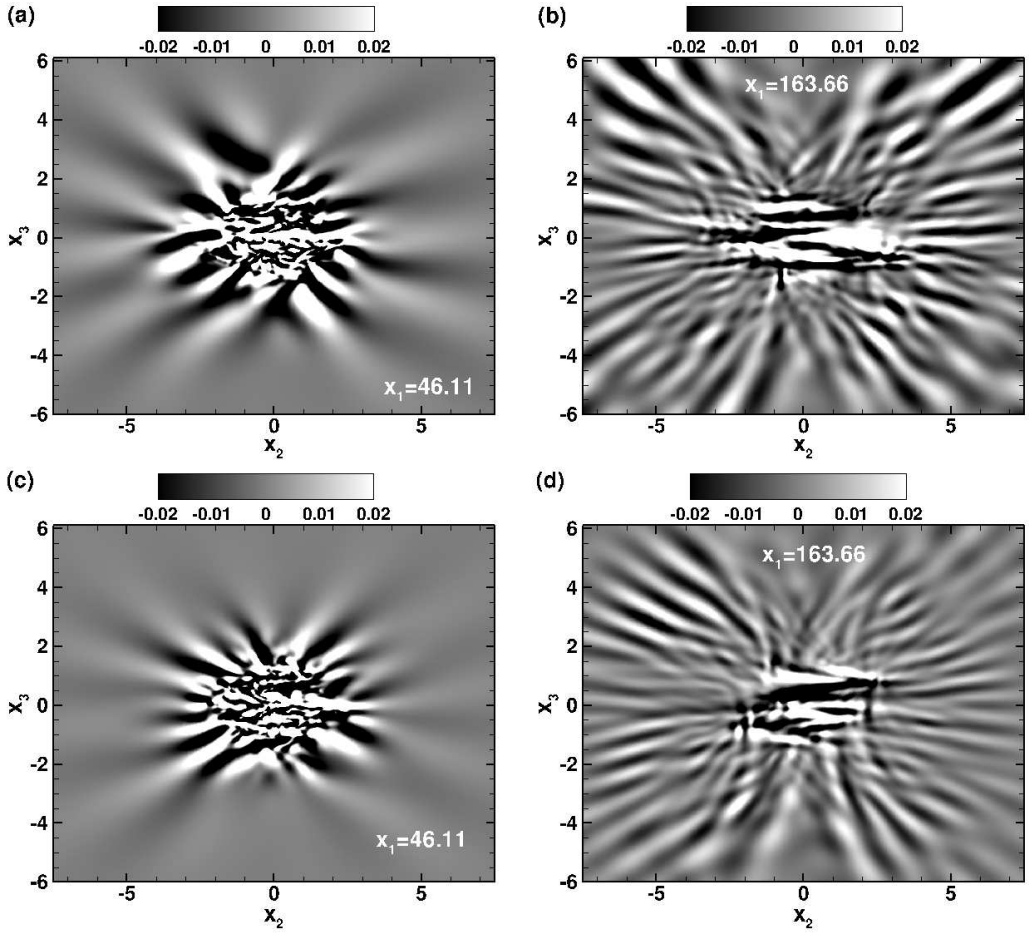

Figure 2.14: Internal gravity wave field visualized by contours of ω_1 at various x_1 locations for cases TP1 (upper row) and TP2 (lower row).

that was shown earlier in figure 2.3. One difference is that the magnitude of ω_1 outside the core of the wake is smaller in TP2, consistent with the smaller wave flux T_p. The organization of the streamwise vorticity into coherent horizontal layers spanning the wake width that was seen earlier in SP50 is seen in the turbulent patches too.

The vertical vorticity in the late wake region of case SP50 exhibited large coherent vortex dipoles as was shown in figure 2.4. Figure 2.15 shows that the vertical vorticity is less organized in the turbulent patches without mean shear. Especially, in case TP2, the vortical structures are much smaller and do not show clear vortex dipoles. Evidently, the initial presence of a larger fraction of fluctuation energy of TP2 in smaller length scales further inhibits the coherence of the

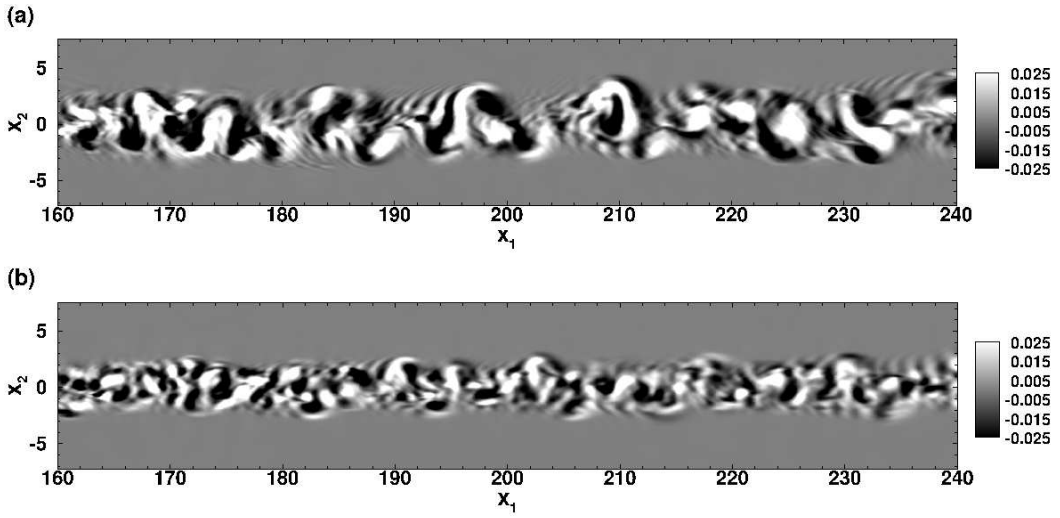

Figure 2.15: Vertical vorticity shown far downstream ($160 < x_1 < 240$) in the turbulent patch simulations: (a) Turbulent patch TP1, (b) Turbulent patch TP2. Instantaneous ω_3 at the horizontal centerplane is shown for both cases.

vortices. At much later time, $t > 400$, larger coherent vortices do emerge in cases TP1 & TP2, but they are significantly weaker than the vortices at corresponding time in the wake with mean shear.

2.6 Effect of initial energy spectrum on the wake evolution

In order to evaluate the effect of the initial spectrum on the evolution of the wake, we compare temporal simulations of cases SP50 and SP50C. Both cases have the same initial TKE but SP50C has higher energy at smaller scales, similar to TP2, as shown in figure 2.1(b). The simulation parameters for SP50C are given in table 2.1. Figure 2.16 (a)-(d) shows a comparison of various statistics between SP50 and SP50C. In figure 2.16(a), we find that the integrated turbulent kinetic energy decays faster in case SP50C as compared to SP50 because of the higher integrated turbulent dissipation in figure 2.16(b), consistent with the the higher initial fluctuation energy at the small scales (figure 2.1(b)) in SP50C. The values of the integrated production are similar between the two cases. The mean kinetic

energy (MKE) plotted in figure 2.16(c) is similar in the two cases except for a somewhat smaller value in SP50 relative to SP50C during $20 < t < 200$. During this time period, the internal wave flux is larger in SP50 as shown in figure 2.16(d) and, consistent with the stronger waves, the wave transport $\langle u'w' \rangle \langle U \rangle$, is larger in case SP50 leading to lower mean velocity and lower MKE. It is worth noting that the larger internal wave flux in case SP50 is consistent with higher fluctuation energy, relative to SP50C, in figure 2.16(a).

Similar to TP2, case SP50C was initiated with the fluctuation energy distributed preferentially at smaller scales relative to case SP50 and TP1. Unlike TP2, case SP50C has an initial mean velocity profile that influences the large scales of the fluctuating energy through horizontal instabilities. Consequently, there is a major difference with respect to TP2: case SP50C exhibits large coherent structures of vertical vorticity that are similar to those in SP50, shown previously in figure 2.4, and the horizontal extent of the wake in SP50C also evolves similarly so as to reach values that are substantially larger than in case TP2.

2.7 Discussion and conclusions

DNS of a spatially evolving self-propelled wake with zero integrated momentum and a patch of turbulence has been performed at Re=15 000 in a stratified fluid to examine the influence of the canonical self-propelled mean velocity profile on the evolution of the wake. The mean velocity affects the evolution of the wake depending upon the amount of mean kinetic energy present in the wake. If the mean kinetic energy is of the order of 10% of the total kinetic energy, the wake evolves similarly to a patch of turbulence with the *same* initial energy spectrum of the fluctuations. But if the mean kinetic energy is increased to 50% in case SP50 we find significant differences in the turbulence statistics for the near to early intermediate wake, moderate differences for the intermediate wake and minor difference for the late wake with respect to a patch of turbulence, TP1. Both the wake and turbulent patch show similar spatial features in the internal wave field but the dipole pattern of the late-wake vortices is more evident in the wake relative to the

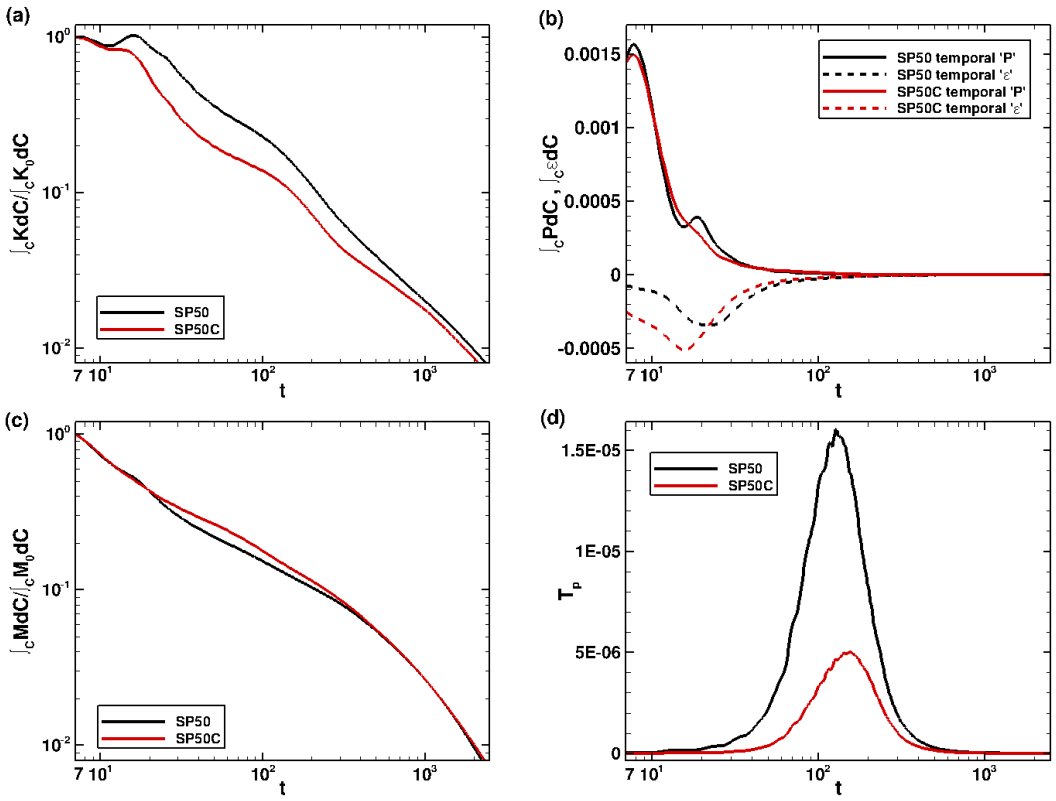

Figure 2.16: Comparison between SP50 and SP50C: (a) Integrated turbulent kinetic energy, (b) Integrated production and dissipation, (c) Integrated MKE, (d) Wave flux

turbulent patch. Strongly stratified flows are known to exhibit vertical layering of the vorticity field. Such layering is found in both the wake and the turbulent patch.

The spectral content of the near wake can differ between cases owing to factors such as different boundary layer characteristics. The influence of spectral distribution of fluctuation energy is studied here by simulating a turbulent patch case, TP2, that has substantially higher energy content at smaller length scales compared to case TP1 although the initial $r.m.s.$ fluctuations are the same. Case TP2 with higher small-scale energy exhibits changes in its evolution relative to case TP1: the TKE is significantly smaller during the evolution, the internal wave radiation is weaker, and the late-wake vortices are smaller and less coherent. In order to evaluate the effect of initial energy spectrum on the wake evolution, case SP50C with the same initial TKE as SP50 but higher small-scale energy content was simulated. Relative to SP50, the evolution of case SP50C exhibits significantly smaller TKE, weaker internal wave flux consistent with the difference that TP2 has with respect to TP1. However, large coherent structures that were seen to form in case SP50 also form in case SP50C and, similar to case SP50, the stratified wake of SP50C also has a substantially larger horizontal extent than the turbulent patches. Evidently, the presence of mean horizontal shear influences the low-wave number part of the energy spectrum resulting in large coherent vortices with enhanced horizontal entrainment.

Another objective of the present DNS study of stratified wakes was to compare the accuracy of the temporally evolving approximation that is often made because of the considerable savings in computational cost. We find that the temporal approximation, when provided with initial conditions that match the inflow conditions of a spatially evolving computational model, leads to mean and turbulent statistics that agree well with those in the spatially evolving flow. The reason is that the approximation of linearizing the nonlinear advection term in the averaged equations around uniform flow is small in the case of a wake since the wake deficit velocity is small compared to the uniform flow. Even when the initial value of the mean kinetic energy in the wake is as large as 50% of the total (mean plus

fluctuation), its relative contribution decreases rapidly ensuring the validity of the temporal approximation.

2.8 Acknowledgements

Chapter 2, in full, is a reprint of the material as it appears in Physics of Fluids 2013, coauthored by Dr. Matthew B. de Stadler and Professor Sutanu Sarkar. A. Pal, M. B. de Stadler & S. Sarkar, The Spatial Evolution of Fluctuations in a Self-Propelled Wake compared to a Patch of Turbulence, *Phys. of Fluids*, *25*, 095106, (2013). The thesis author was the primary author of this paper.

Chapter 3

Effect of External Turbulence on the Evolution of a Wake in Stratified and Unstratified Environments

3.1 Introduction

Wakes of bodies often develop in the presence of external (background) turbulence, e.g. propelled bodies, marine animals, wind turbines, and particles in multiphase flow. Furthermore, the environment may be stratified in applications of interest. The effect of external turbulence on stratified wakes is poorly understood, motivating the present DNS study of the intermediate-to-far wake. We also perform simulations of unstratified wakes to provide a baseline for comparison.

Much of our current knowledge regarding the evolution of axisymmetric unstratified wakes in the presence of external turbulence is derived from work related to multiphase particulate flows. Thus, the body Reynolds number $Re = UD/\nu \approx O(100-1000)$ was small, the background turbulence integral length scale l_{int} was large relative to the body leading to $l_{int}/D \approx O(10-100)$, and the far

wake was not measured in those studies. Here, U is the freestream velocity and $D = 2r_0$ is the body diameter. The level of external turbulence measured by the normalized root mean square (r.m.s.) of the streamwise velocity fluctuation, u'_{ext}, ranged from low to high values of u'_{ext}/U. Although we study the intermediate-to-far wake properties as well as larger bodies with larger Re and $l_{int}/D \approx O(1)$, we briefly review the literature in that different regime in the following paragraphs.

Wu & Faeth (1994) experimentally studied a sphere placed at the axis of turbulent pipe flow over the range $Re = 135-1560$ and $u'_{ext}/U = 4\%$, making measurements up to $x/D \approx 20$. They found that, despite being turbulent, the wake has a self-preserving behavior with a laminar-like scaling law: the mean maximum defect velocity, $U_0(x) \propto x^{-1}$, and the mean wake half width $r \propto x^{1/2}$. The x^{-1} scaling was attributed to a constant (radially and axially) turbulent eddy viscosity and the wake spread rate was found to increase with increasing level of external turbulence. Wu & Faeth (1995) explored stronger external turbulence levels (u'_{ext}/U up to 9%) finding that the wake decayed faster than x^{-1}, but did not further quantify the power law exponent. Bagchi & Balachandar (2004) performed DNS of flow past a sphere embedded in a frozen realization of homogeneous, isotropic turbulence. The level of free stream turbulence ($u'_{ext}/U = 10 - 25\%$) was high, and the sphere was relatively very small so that $l_{int}/D = 52 - 333$ and $Re = 50 - 600$. The wake, simulated until $x/D = 15$, was found to exhibit $U_0 \approx x^{-1}$ decay of the mean defect velocity and a wake spreading rate that increased with the level of external turbulence, similar to Wu & Faeth (1994). Legendre *et al.* (2006) simulated flow past a bubble and a solid sphere placed in turbulent pipe flow. The simulations were at low $Re = 200 - 500$, $u'_{ext}/U = 4\%$, and $l_{int}/D = O(10)$. The mean wake was found to decay as $U_0 \propto x^{-2}$, faster than the wake decay in all previous studies, when the streamwise distance ($x/D > 13$ for the sphere) became sufficiently large. This effect was attributed to a crossover point when the evolving defect velocity decreased to the same order as r.m.s of external turbulent fluctuations and a supporting theoretical analysis was provided. Different from the aforementioned studies, Amoura *et al.* (2010) elected to consider external turbulence with

$l_{int}/D = O(1)$ while, similar to previous work, they considered $Re = 100 - 1000$. High intensity turbulence was generated by a series of jets upstream of a water channel and the sphere, placed on the axis of the channel, was exposed to approximately homogeneous, isotropic turbulence with $u'_{ext}/U = 15 - 26\%$. The wake deficit velocity became smaller than the free-stream velocity by $x/D = 3$ and was found to subsequently exhibit $U_0 \propto x^{-2}$ scaling, much earlier than in the lower-intensity turbulence case of Legendre *et al.* (2006). Furthermore, Amoura *et al.* (2010) found that the r.m.s of external turbulence (it did not axially decay over the range of measurements) was the appropriate normalization velocity scale for similarity profiles and not the defect velocity.

Recently, Rind & Castro (2012*a*,*b*) studied the influence of external turbulence on intermediate-to-far wake behavior at $Re = O(10,000)$, higher than in the previous studies. The DNS of Rind & Castro (2012*a*) adopted the temporally evolving model customary in simulations of the far wake, e.g. the planar wake of Moser *et al.* (1998) and the axisymmetric wake of Gourlay *et al.* (2001). A background field of homogeneous, isotropic turbulence was combined with an initial field having mean and turbulent velocity profiles representative of a turbulent wake, and the subsequent evolution was tracked as a function of time, a quantity that is analogous to downstream distance in the spatially evolving wake. Rind & Castro (2012*a*) simulated three cases with initial $u'_{ext}/U_0 = 0.09$, 0.17 and 0.36 corresponding to $Re \approx 10,000$ and $u'_{ext}/U \approx 1$, 2 and 4%. The wake deficit velocity, $U_0(t)$, was found to decay substantially faster in the cases with 2 and 4% external turbulence, approaching a x^{-1} law for the 4% case. The turbulence profiles in these cases deviated from the self-similar profiles found in the pure wake. The companion experimental study by Rind & Castro (2012*b*) of the $Re = 15,000$ wake of a disc placed in decaying grid turbulence also found that external turbulence disrupted self-similarity in turbulence profiles. The profiles of normal stresses became flatter across the wake. Turbulence levels in the far wake were found to be larger in some cases and it was suggested that the level of external turbulence relative to the wake turbulence could be a differentiating factor. It is worth noting that external

turbulence was found to affect the near-wake, e.g. reduction of recirculation zone and change in drag. Direct simulations of the unstratified flow past a sphere in a computational model that includes the body have been recently performed in the turbulent regime, e.g. by Rodriguez *et al.* (2011) at $Re = 3700$. Bazilevs *et al.* (2014*a*) compared the effect of uniform and turbulent inflow conditions on the computation of the flow over a sphere at $Re = 3700$. They reported an increase in the drag force on the sphere, dramatic reduction in the length of the recirculation bubble and significantly stronger near-wake turbulence as a consequence of adding free-stream turbulence of moderate intensity. Very low frequency modes, known to occur at moderate Re, were absent when free-stream turbulence was added to the inflow. The evolution of the flow into the intermediate and far wake was not possible in these body-inclusive simulations.

Stratification of the environment qualitatively changes the evolution of the intermediate-to-far wake as shown by laboratory experiments of both self-propelled and towed wakes, e.g. (Lin & Pao, 1979; Gilreath & Brandt, 1985; Spedding *et al.*, 1996a) as well as simulations (Ghosal & Rogers, 1997; Moser *et al.*, 1998; Gourlay *et al.*, 2001; Dommermuth *et al.*, 2002) that have recently been extended to higher Reynolds number (Brucker & Sarkar, 2010; Diamessis *et al.*, 2011). The value of $Fr = U/ND$ where N is the background value of the buoyancy frequency determines buoyancy effects. At low Fr less than O(1), the body generates internal gravity waves and the recirculation region lengthens as discussed, e.g., by Chomaz *et al.* (1993a), Bonneton *et al.* (1993) and Bonneton *et al.* (1996). At higher $Fr = O(1)$ corresponding to the present work, the wake is longer lived than its unstratified counterpart, has primarily horizontal motion at late time that is organized into coherent vortices, and radiates internal gravity waves. A stratified wake exhibits different stages in its evolution: a near wake where the decay rate is initially close to the unstratified case, a plateau corresponding to the onset of buoyancy effects that starts at $Nt = Nx/U \approx 2$, a nonequilibrium (NEQ) regime starting at $Nt \approx 5$ wherein the wake decays at a rate that is slower than in the unstratified case and, finally, a quasi-2D regime where the decay rate is higher than

Table 3.1: Parameters of the unstratified and stratified wake simulations.

Case	*Re*	*Fr*	u'_{ext}/U	$Re_{\lambda,ext}$	$L_{int,ext}/L_{int,cl}$	$L_{int,cl}/2r_0$
1. $EXT0_{unst}$	10,000	∞	-	-	-	4.405
2. $EXT1_{unst}$	10,000	∞	1%	≈ 41	≈ 0.47	4.130
3. $EXT3_{unst}$	10,000	∞	3%	≈ 115	≈ 1.21	4.118
4. $EXT4_{unst}$	10,000	∞	4%	≈ 150	≈ 1.56	4.1
5. $EXT0_{st}$	10,000	3	-	-	-	4.405
6. $EXT1_{st}$	10,000	3	1%	≈ 41	≈ 0.47	4.130
7. $EXT3_{st}$	10,000	3	3%	≈ 115	≈ 1.21	4.118
8. $EXT4_{st}$	10,000	3	4%	≈ 150	≈ 1.56	4.1

in the NEQ regime. The NEQ regime lasts longer with increasing Re (Brucker & Sarkar (2010); Diamessis *et al.* (2011)). Internal gravity waves generated by a turbulent wake are of interest and have been recently studied by Abdilghanie & Diamessis (2013) over a wide range of Re and Fr. Interestingly, the internal wave emission is prolonged to a longer time interval at high Re.

It is clear from the preceding literature survey that external turbulence may have important consequences for wakes. The evolution of a wake under the influence of a free-stream turbulence in a stratified medium has not been reported in the literature. We are thus motivated to explore the behavior of a stratified towed-wake in a disturbed ambient. The intensity of external turbulence is varied while the integral length scale remains at $l_{int}/D = O(1)$. Unstratified cases are also simulated for comparison. Several of the previous studies of unstratified wakes show a faster decay of the mean defect velocity in the presence of external turbulence.We revisit this question within the framework of wake energetics. DNS of the Navier-Stokes equations in a temporally evolving model, a tool that has been used in our past studies of the wake (Brucker & Sarkar, 2010; de Stadler & Sarkar, 2012; Pal *et al.*, 2013), is employed here too.

3.2 Problem formulation

The level of external turbulence is systematically varied from zero to 4% of the freestream mean velocity as shown in table 6.1. The ratio of the initial integral

length scale of the external turbulence, $L_{int,ext}$, to that of the wake turbulence at the centerline, $L_{int,cl}$, also increases while remaining $O(1)$. The microscale Reynolds number of the external freestream turbulence, $Re_{\lambda,ext} = \frac{20}{3}(\frac{k^2}{\epsilon\nu})^{1/2}$ is moderate. Here, k and ϵ are the turbulent kinetic energy and dissipation rate, respectively. All simulations were performed with $N_1 = 2048$, $N_2 = 512$ and $N_3 = 384$ grid points in the x_1 (streamwise), x_2 (spanwise) and x_3 (vertical) directions, respectively. $L_1 = 81.92$, $L_2 = 18.84$ and $L_3 = 13.72$ are the computational domain lengths normalized by the body and excluding the sponges.

The problem formulation and the numerical model of the towed wake are similar to those used by Brucker & Sarkar (2010). The background surrounding the turbulent wake in Brucker & Sarkar (2010) was quiescent whereas we introduce background fluctuations external to the wake in the present problem. A temporally evolving model without the body and with streamwise periodicity in the flow field is adopted as in several previous studies (Gourlay *et al.*, 2001; Dommermuth *et al.*, 2002; Brucker & Sarkar, 2010; Diamessis *et al.*, 2011). The initial velocity prescribed in the temporally evolving model has mean and r.m.s velocity profiles taken to approximate statistics at location x_0 behind the body in the laboratory wake. The distance from the body (x in the laboratory frame) that is equivalent to clock time t in the temporally evolving model can be computed by $x = x_0 + Ut$ where U is the constant towing velocity of the body in the laboratory wake. The temporally evolving model allows simulation into the far wake without the computational cost of resolving the boundary layer at the body. It is worth noting that, once the temporal approximation is made, the actual value of U does not influence the evolution in temporal model. The value of U determines only the temporal to spatial transformation of the statistics. Pal *et al.* (2013) showed that the results from a spatially evolving simulation match with those of a temporal simulation initialized with conditions at $x/D \approx 7$ if the inflow conditions for the spatial model match the initial conditions employed for the temporal model. The defect velocity, approximately 10% of the body velocity, is sufficiently small at $x/D \approx 7$, allowing the temporal approximation. The initial density perturbations in the wake and the background for all the simulations are set to zero. However, if the simulations

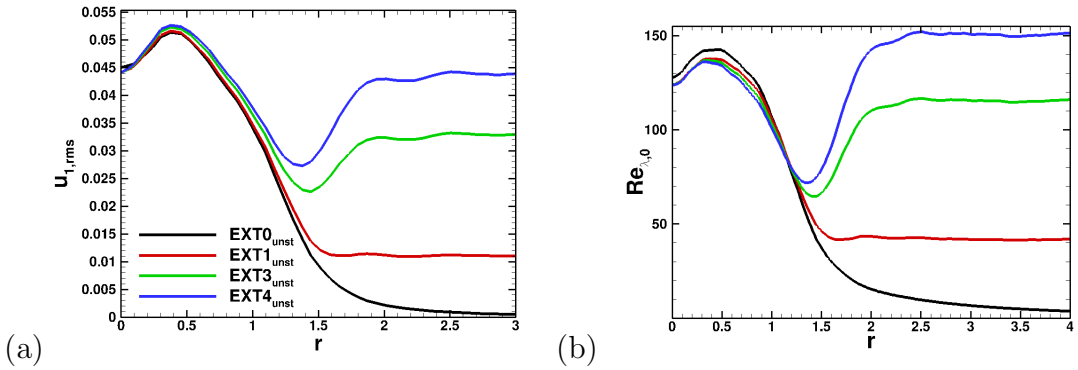

Figure 3.1: (a) Initial profile of root mean square (r.m.s) velocity, $u'_{1,rms}$. (b) Initial profile of Taylor microscale Reynolds number, Re_λ.

are initialized with some density perturbations of small amplitude, the statistics are not expected to show significant difference after an initial transient, based on the results of Brucker & Sarkar (2007) for a temporally evolving stratified mixing layer. The three-dimensional, incompressible, unsteady form of the conservation equations for mass, momentum and density subject to the Boussinesq approximation for buoyancy are numerically solved as discussed by Brucker & Sarkar (2010). The governing equations are nondimensionalized using the uniform body velocity, U, and the body diameter, D.

3.2.1 Towed wake initialization

The mean and fluctuating fields are initialized with profiles that are characteristic of the near wake (Bevilaqua & Lykoudis, 1978; Uberoi & Freymuth, 1970) for the entire domain in both the unstratified and stratified cases. The initial mean velocity profile is given by

$$\langle u_1(r) \rangle = U_0 e^{\left(-\frac{1}{2}\left(\frac{r}{r_0}\right)^2\right)} , \tag{3.1}$$

where U_0 is the centerline defect velocity and $r_0 = D/2$. The initial value of U_0 is taken to be 0.11 corresponding to an initial distance behind the body of $x_0/D \approx 7$. The initial velocity fluctuations are generated as an isotropic solenoidal velocity

field in spectral space satisfying the following spectrum,

$$E(k) = (k/k_0)^4 e^{-2(k/k_0)^2}, \tag{3.2}$$

where $k_0 = 4$. The fluctuating field is localized to the wake by multiplying it with the following function,

$$g(r) = a\left[1 + \left(\frac{r}{r_0}\right)^2\right] e^{-\frac{1}{2}\left(\frac{r}{r_0}\right)^2}, \tag{3.3}$$

where a is the amplitude, $r = \sqrt{x_2^2 + x_3^2}$ and $r_0 = 0.5$ is the normalization parameter. The choice of the function $g(r)$ (Dommermuth *et al.*, 2002; Brucker & Sarkar, 2010) is consistent with laboratory measurements of *r.m.s.* turbulence profiles, e.g. Bevilaqua & Lykoudis (1978). This initial fluctuating field is allowed to evolve, keeping the mean velocity profile given by (3.1) fixed until the maximum value of $\langle u_1' u_r' \rangle / K \cong -0.25$, ensuring that the fluctuations establish a cross-correlation that is typical of turbulent shear flow. Here, K is the turbulent kinetic energy. Azimuthal and streamwise averaging are performed to obtain the time-evolving statistics during this adjustment period.

3.2.2 External turbulence

Equation (3.2) is employed to generate the initial level of background fluctuations but, instead of using the damping function (3.3) to localize the fluctuations to the wake, a case-dependent constant value is used for the amplitude a (a is chosen so as to obtain the required ratio of u'_{ext}/U). The pre-simulations for the external turbulence are performed in a triply periodic box and allowed to evolve as an isotropic turbulent field until the required ratio of u'_{ext}/U is achieved. The background turbulence decays as time advances in the simulations.

3.2.3 Calculation of statistics

Mean statistics are computed using streamwise averaging over the computational domain length, L_1. The streamwise average in the temporally evolving

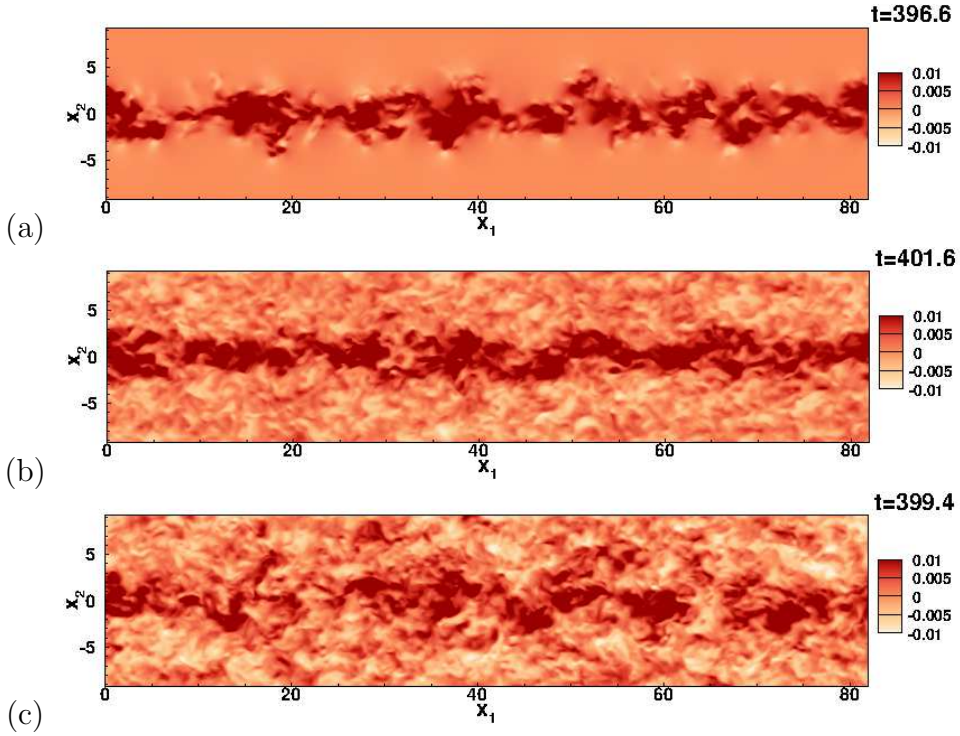

Figure 3.2: Instantaneous streamwise velocity at time, $t \approx 400$, in the unstratified cases: (a) $EXT0_{unst}$, (b) $EXT1_{unst}$, and (c) $EXT4_{unst}$.

model is equivalent to time averaging in the laboratory frame. The Reynolds decomposition into mean and fluctuations is

$$u_i = \langle u_i \rangle + u_i^{'}, \rho = \langle \rho \rangle + \rho^{'}, p = \langle p \rangle + p^{'} \, . \tag{3.4}$$

Statistics in the stratified wake are a function of time (t) as well as the spanwise (x_2) and vertical (x_3) directions. Although statistics in the unstratified wake are a function of the radial coordinate (r) and t, we do not present profiles as a function of r and, therefore, do not perform additional azimuthal averaging.

3.2.4 Simulation parameters

The parameters of the different cases are summarized in Table 6.1. The intensity, u'_{ext}/U, of the external fluctuations is varied between 0 and 4% in both unstratified and and stratified ($Fr = 3$) situations. The ratio of the initial integral

length scale of the external fluctuations ($L_{int,ext}$) to the corresponding value at the centerline ($L_{int,cl}$) is $O(1)$ as shown in table 6.1. The initial value of microscale Reynolds number is moderate with a value of $Re_\lambda = 150$ at the highest turbulence intensity of 4%. For the stratified cases, the initial density field has a linear gradient in the vertical direction corresponding to $Fr = 3$ ($Fr = \frac{U}{ND}$, $N^2 = -\frac{g}{\rho_0}\frac{\partial \rho}{\partial x_3}$, where $\rho_0 = 1$ is the reference density) without superposed fluctuations. Approximately 400 million equispaced grid points are used for the simulations. The simulations are designed with a resolution of $\Delta x_i/\eta < 4$ for all the cases. Here, η is the Kolmogorov length scale calculated as $\eta \equiv (Re^3\varepsilon)^{-1/4}$ with ε denoting the nondimensional turbulent dissipation rate defined by $\varepsilon \equiv \frac{2}{Re_0}\langle s'_{ij}s'_{ij}\rangle$, where $s'_{ij} = \frac{1}{2}(\frac{\partial u'_i}{\partial x_j} + \frac{\partial u'_j}{\partial x_i})$.

The external turbulent field (section 3.2.2) is combined with the towed-wake (section 3.2.1) in the outer region of the wake which, following Redford & Coleman (2007), is taken to be the region where the mean velocity of the towed wake is less than 5% of the maximum defect velocity. The combined field is allowed to adjust for a few time units to smear out the gradients that are initially generated at the interface between the two fields. Figure 3.1(a) shows the initial radial profiles of $u_{1,rms}$ after the adjustment period. The external value of r.m.s. velocity fluctuation vary from small to substantial fractions of the corresponding values at the wake centerline. Profiles of the Taylor microscale Reynolds number, $Re_{\lambda,ext}$, are shown in Figure 3.1 (b). In the stratified cases, the combined field undergoes a further buoyancy adjustment time during which the density fluctuations are allowed to increase from their initial zero value.

3.3 Visualization

Qualitative effects of a turbulent background on the spatial organization of the flow are examined through visualizations of velocity and vorticity. It will be shown below that external turbulence disrupts some features of the organization of the stratified wake, e.g. internal gravity waves, but not others, e.g. coherent

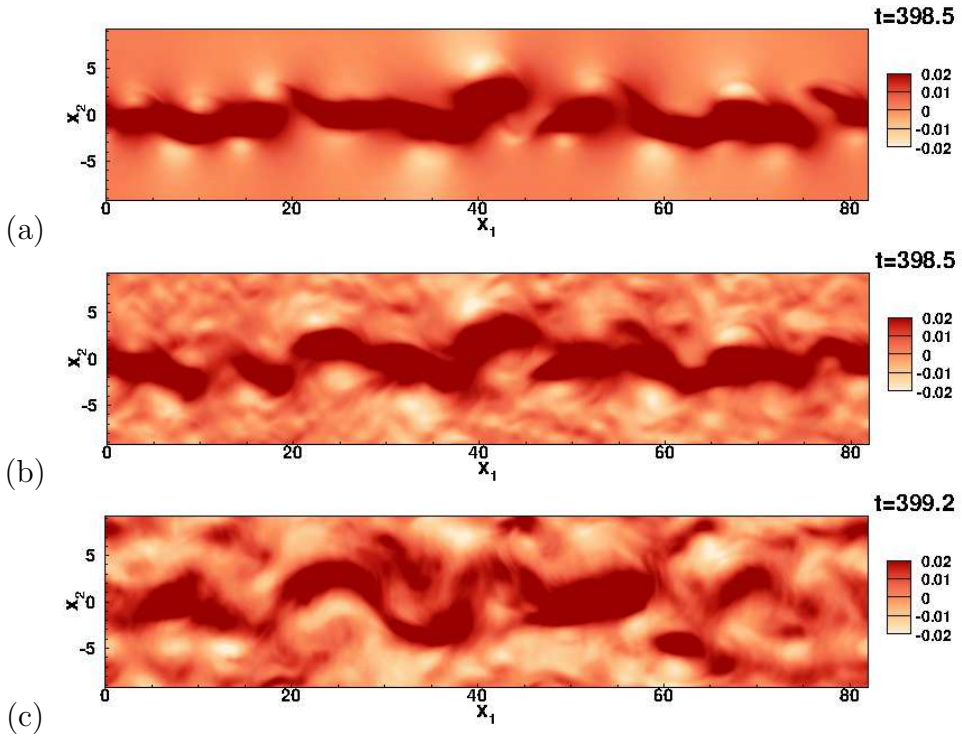

Figure 3.3: Instantaneous streamwise velocity at $t \approx 400$ ($Nt \approx 133$) in the stratified cases at the center plane ($x_3 = 0$): (a) $EXT0_{st}$, (b) $EXT1_{st}$ and (c) $EXT4_{st}$.

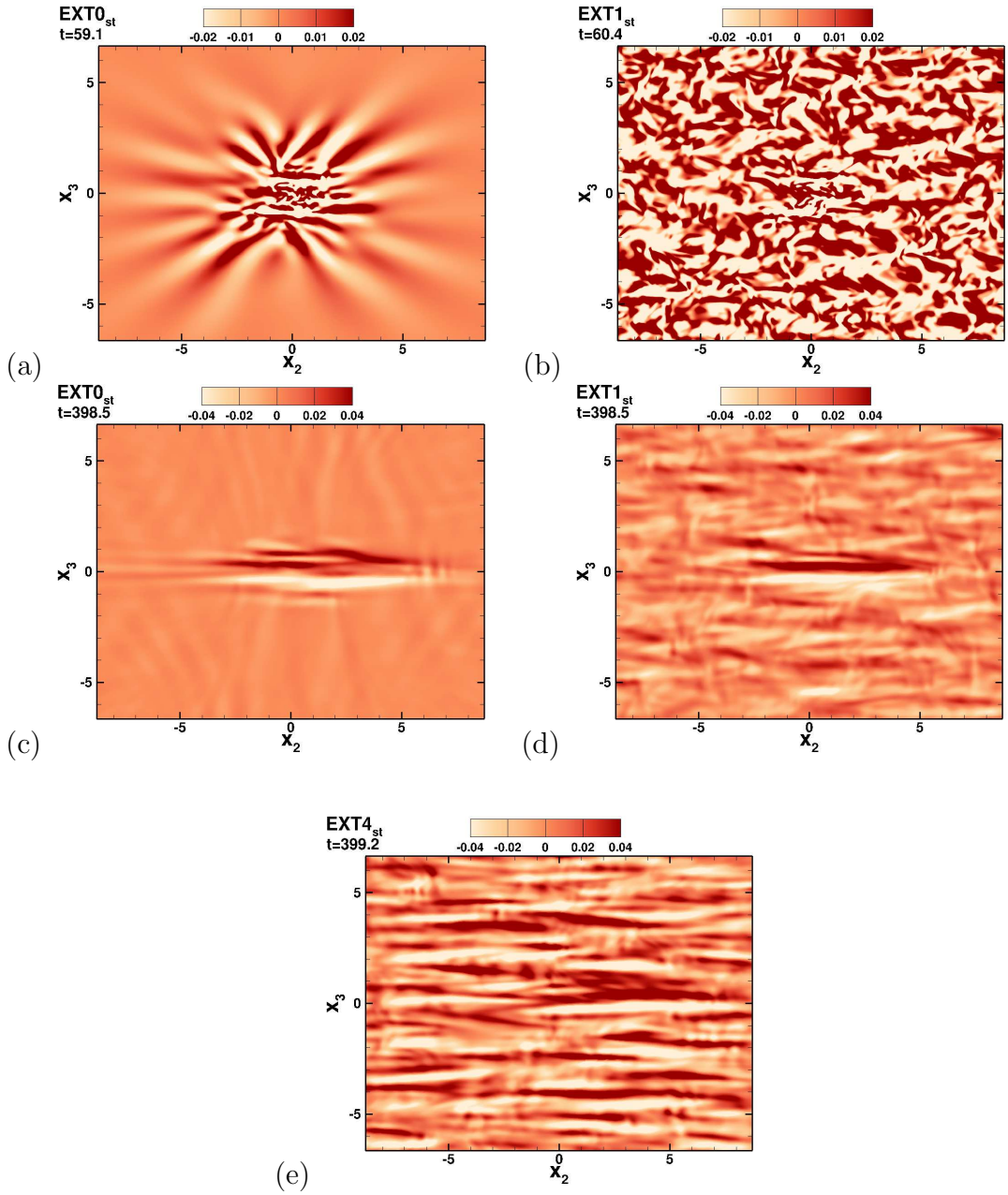

Figure 3.4: Comparison of the instantaneous ω_1 at a x_2-x_3 plane for the stratified cases at $t \approx 60$ (a, b) and at $t \approx 400$ (c, d) between the undisturbed background and 1% external turbulence cases. The bottom snapshot corresponds to 4% external turbulence.

pancake eddies.

The evolution of the instantaneous wake velocity for the unstratified cases and the stratified cases are shown in figures 3.2 and 3.3, respectively. The streamwise velocity for $EXT0_{unst}$ (figure 3.2(a)) shows a recognizable wake pattern. Similarly, the case with 1% external turbulence in Figure 3.2(b) also displays an identifiable wake pattern. However, when the external turbulence level increases to 4%, the wake core is significantly modified by entrainment of background fluid with small-scale turbulence and it becomes more difficult to distinguish the wake from the background in figure 3.2 (c). The evolution of the wake under the influence of 1% free-stream turbulence in a stratified fluid (figure 3.3 (b)) is similar to the stratified case without background turbulence (figure 3.3 (a)). It is noticeable that the wake of case $EXT4_{st}$ evolves into large coherent structures whereas the wake of case $EXT4_{unst}$ has a plethora of small-scale structures. The external turbulence in case $EXT4_{st}$ becomes organized into larger-scale coherent patches by buoyancy, so that entrainment of external fluctuations into the wake at later time does not lead to additional small-scale fluctuations in the wake. Therefore, although the 4% external turbulence diminishes the prominence of the stratified wake relative to the background relative to the "clean" case, it does not disrupt the stratified wake core as much as in the corresponding unstratified case.

External turbulence disrupts the well-known pattern of internal waves. Figure 3.4 shows visualizations of the horizontal vorticity ω_1 in a $x_2 - x_3$ cross section of the flow. At $t \approx 60$, case $EXT0_{st}$ without background fluctuations shows the propagation of internal gravity waves into the background. Even the case with a low level of 1% background turbulence (figure 3.4 (b)) exhibits a chaotic pattern of streamwise vorticity with almost no suggestion of wake-generated internal waves. At a later time $t \approx 398$, $EXT0_{st}$ displays the formation of multiple layered structures (figure 3.4 (c)) which are a defining characteristic of pancake eddies in strongly stratified vortical flows. In contrast to the barely discernible wave pattern at early time, case $EXT1_{st}$ at $t \approx 398$ shows multiple layered structures similar to

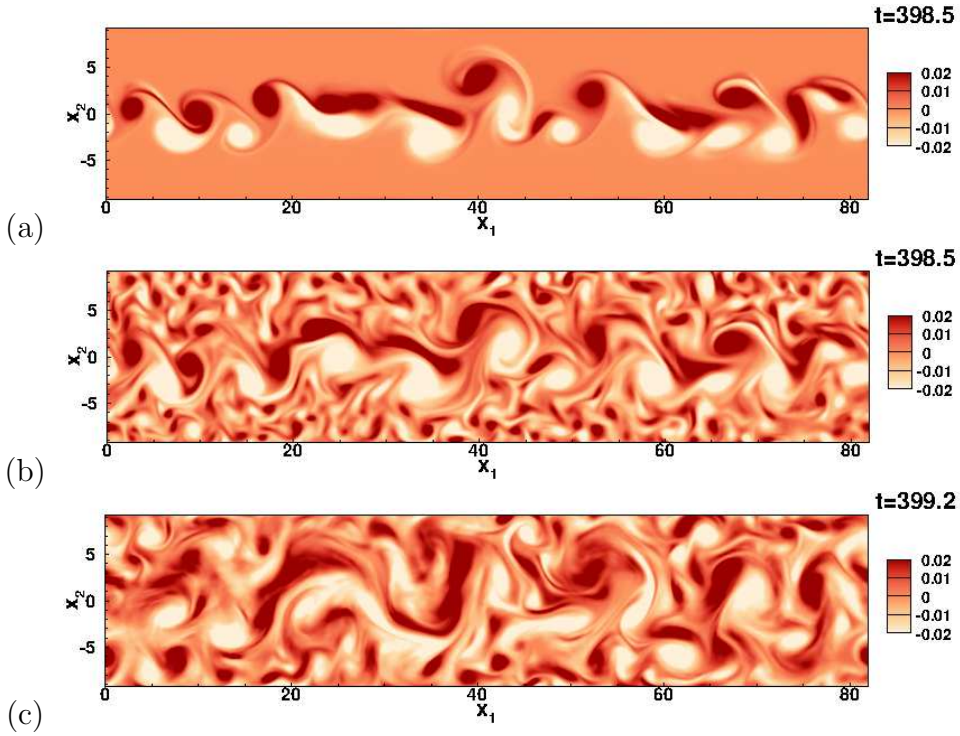

Figure 3.5: Vertical vorticity at a horizontal cross-section in the stratified cases: (a) $EXT0_{st}$, (b) $EXT1_{st}$, and (c) $EXT4_{st}$ at $t \approx 398$ ($Nt \approx 133$).

that of the $EXT0_{st}$ revealing the presence of a wake. Case $EXT4_{st}$ also shows the formation of layered structures at $t \approx 398$ (figure 3.4 (c)); however, the external turbulence also evolves into similar layered structures making it difficult to recognize the wake.

The organization of horizontal motion into coherent eddies is a distinguishing feature of stratified flows. Figure 3.5 shows snapshots of vertical vorticity ω_3 in the x_1 - x_2 plane for the different stratified cases. Large coherent vortices emerge as can be seen at $t = 398$ for case $EXT0_{st}$ (figure 3.5 (a)). Case $EXT1_{st}$ shown in figure 3.5 (b) also displays coherent vortices at this time, similar to case $EXT0_{st}$. These coherent structures are surrounded by the smaller vortices formed by the external turbulence. These small vortices interact and distort the primary vortex structure of the wake. As the external turbulence intensifies (Figure 3.5 (e)), the background fluctuations evolve into larger vortices that interact with the wake and

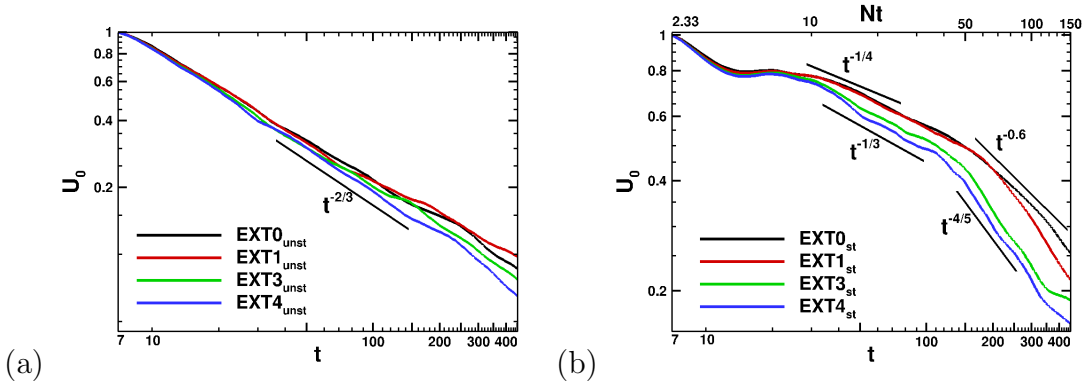

Figure 3.6: Centerline defect velocity normalized by the initial value: (a) Unstratified cases, and (b) Stratified cases.

significantly distort the coherent structures in the wake core. In the unstratified case, the wake does not evolve into coherent horizontally eddying motion. Therefore, it becomes difficult to distinguish the wake at $t \approx 400$ from the background in snapshots of the vertical vorticity, even with 1% external turbulence (not shown here).

3.4 Mean flow characteristics

Figures 4.5 (a) and (b) show the evolution of the mean centerline defect velocity $U_0(t)$ for the unstratified and the stratified cases, respectively. The unstratified cases in figures 4.5 (a) exhibit t^{-n} power law with the classical $n = -2/3$ power law beyond $t \approx 25$. The virtual origin, t_0, of the self-similar law, $U_0 = A(t - t_0)^{-2/3}$ is obtained by the intercept of a linear fit to $U_0^{-3/2}(t)$ (plotted in linear-linear scale) with the t-axis. The velocity, thus plotted, exhibits an excellent fit in the case without external turbulence to a straight line that has $t_0 \approx 10$ while the other cases show adequate straight line fits with non-zero values for t_0. Initial conditions are known to influence the existence of self-similar behavior and the virtual origin of the power laws. For instance, Redford *et al.* (2012) compare two very different initial conditions (equispaced vortex rings versus low-level broadband noise superposed on a mean velocity profile) and find that each case exhibits self-similar power laws relatively early ($t_0 \approx 60$ in the vortex ring case) in the mean defect velocity and

half-width with the expected exponents but the thickness growth rates are different between the two initializations for a long period before eventually approaching a common, possibly universal value. The surprisingly small value of $t_0 \approx 10$ in the present simulations may be due to the precursor adjustment period where the fluctuations are allowed to develop a correlation coefficient of $\langle u_1' u_r' \rangle / K \cong -0.25$, typical of shear flows, before evolving the wake.

The effect of external turbulence on the evolution of centerline mean defect velocity is weak in the unstratified cases relative to the stratified situation (figure 4.5 (b)) where U_0 is reduced by almost a factor of 2 at $t = 300$ in case $EXT4_{st}$ with 4% external turbulence as compared to the$EXT0_{st}$ case. In case $EXT1_{st}$, the mean defect velocity evolves similar to $EXT0_{st}$ until $Nt \approx 70$ when it deviates. Increasing the intensity of the external turbulence to 3% and 4% results in a much earlier ($Nt \approx 10$) deviation of the defect velocity towards smaller values relative to $EXT0_{st}$. Note that $Nt \approx 10$ is approximately the same buoyancy time period where the accelerated collapse phase occurs as reported by Bonnier & Eiff (2002) and Brucker & Sarkar (2010). At $Nt \approx 10$, the wake starts to preferentially expand in the horizontal direction. Background turbulence enhances the expansion leading to values of defect velocity that are smaller relative to the case with quiescent background. The nominal decay rates are found to follow an approximate scaling of $t^{-1/3}$ during $10 < Nt < 50$ for $EXT3_{st}$ and $EXT4_{st}$. During the period $50 < Nt < 120$, all the cases with external turbulence follow an approximately $t^{-4/5}$ scaling for the decay rate of the defect velocity.

It is worth emphasizing that, although the magnitude of U_0 under the influence of the external turbulence is quantitatively reduced with respect to the stratified wake with undisturbed background, the qualitative effects of buoyancy on the evolution of defect velocity are unaltered. The different stages of the evolution of U_0 are preserved, i.e., we find a near wake where the decay rate is initially close to the unstratified case, a plateau corresponding to the onset of buoyancy effects, a nonequilibrium (NEQ) regime where the wake decays at a rate that is

slower than in the unstratified case and, finally, a quasi-2D regime where the decay rate is higher than in the NEQ regime.

The evolution of the mean kinetic energy $m.k.e. \equiv \langle u_i \rangle \langle u_i \rangle / 2$ is given by

$$\frac{D(m.k.e.)}{Dt} = -P + \overline{B} - \overline{\varepsilon} - \frac{\partial T_i}{\partial x_i}\,, \tag{3.5}$$

where P is the production of turbulent kinetic energy, $\overline{B}$ is the buoyancy flux associated with mean fields, $\overline{\varepsilon}$ is the viscous dissipation rate of the mean velocity and T_i is the transport of the $m.k.e.$. Figure 3.7(a) shows that the area-integrated $m.k.e$, similar to the centerline defect velocity, also exhibits enhanced decay in the presence of external turbulence. The area of integration is taken to be the half-width region so as to focus on the wake core. To understand the faster decay of the defect velocity and the $m.k.e.$ under the influence of higher intensities of external turbulence, it is helpful to note the following characteristics of the area-integrated (3.5): the production of the turbulent kinetic energy, P, is the dominant term, the value of P is positive here, as in most turbulent shear flows, and the negative sign preceding P implies the loss of $m.k.e.$ to turbulence. The effect of the turbulent production on the mean wake is presented in figure 3.7(b) by calculating the cumulative integral of production over the half width,

$$Q = \int_0^t \int_C P dC dt\,,$$

normalized by the initial area-integrated value of $m.k.e.$ Figure 3.7(b) shows that, as the intensity of the external turbulence increases, the fraction of initial $m.k.e$ removed by turbulent production diverges from the quiescent freestream case. The higher values of this fraction for $EXT3_{st}$ and $EXT4_{st}$ signify that the external fluctuations enhance the turbulent production term in (3.5), thereby removing energy from the $m.k.e.$ reservoir faster than in the case with undisturbed background. This leads to the faster mean wake decay in the presence of external turbulence as shown by figure 3.7(a) and figure 4.5(b).

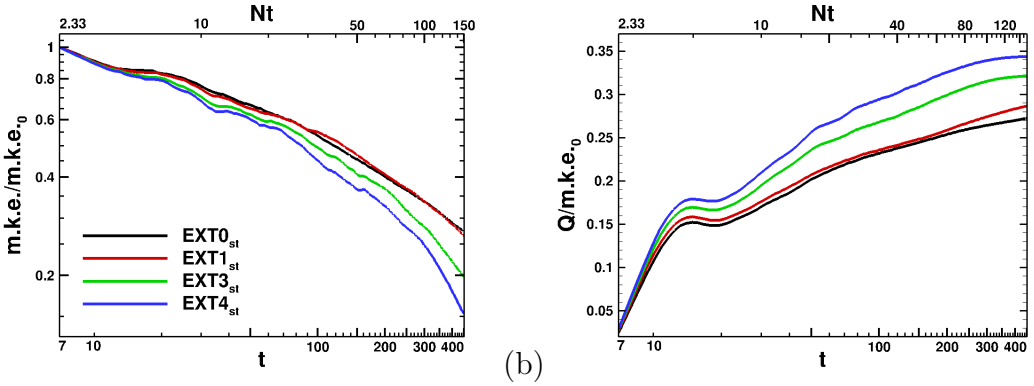

(a) (b)

Figure 3.7: (a) Integrated mean kinetic energy in the stratified cases, and (b) Cumulative integral of turbulent production normalized by the initial integrated mean kinetic energy in the stratified cases.

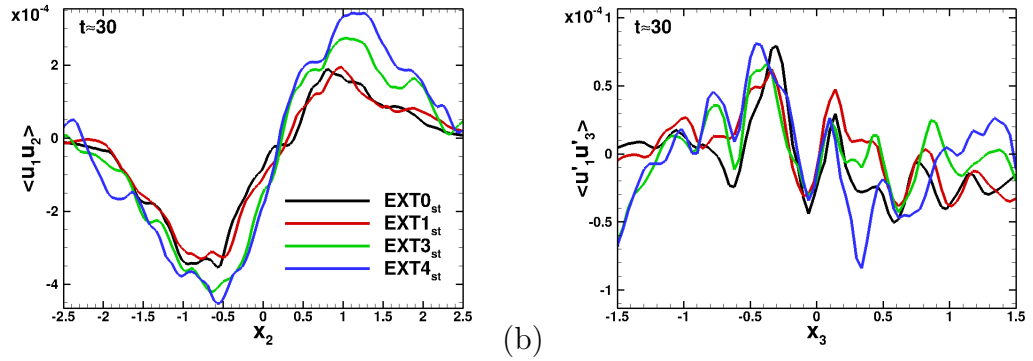

(a) (b)

Figure 3.8: Reynolds stress at $t \approx 30$ in the stratified cases: (a) $\langle u_1' u_2' \rangle$ corresponding to motion in horizontal planes, and (b) $\langle u_1' u_3' \rangle$ corresponding to motion in vertical x_1-x_3 planes.

3.5 Fluctuating flow characteristics

Changes to mean velocity are accompanied by changes to turbulence characteristics, e.g., turbulence levels inside the wake are enhanced, horizontal profiles tend to be flatter, and vertical profiles are unchanged in shape. Figures 3.8 (a)–(b) show Reynolds shear stress profiles at $t \approx 30$. The profiles of $\langle u_1' u_2' \rangle$ for $EXT0_{st}$ and $EXT1_{st}$ are similar. However, the cases with 3% and 4% external turbulence exhibit higher values of Reynolds shear stress associated with horizontal motion as illustrated by figure 3.8 (a). As the intensity of the external turbulence increases to 3% or 4%, the entrainment of external turbulence from the horizontal direction into the wake also increases resulting in the increase of $\langle u_1' u_2' \rangle$. In contrast, the Reynolds shear stress $\langle u_1' u_3' \rangle$, corresponding to vertical motion, does not show clear differences among the different cases, consistent with the effect of external turbulence being more prominent on horizontal motion as was seen in the preceding sections. The Reynolds shear stress, $\langle u_1' u_2' \rangle$, in the wake is correlated to the horizontal mean velocity gradient, $\partial \langle u \rangle_1 / \partial x_2$ (not shown here) similar to the findings of Meunier & Spedding (2006) and de Stadler & Sarkar (2012), irrespective of background turbulence.

The pointwise turbulent kinetic energy, $t.k.e. = \langle u_i' u_i' \rangle / 2$, is obtained by streamwise averaging and is a function of x_2 and x_3. Profiles of K along the horizontal and the vertical centerlines are shown in figures 3.9–3.10 at two different times. At $t \approx 60$, the $t.k.e.$ profile of the $EXT1_{st}$ wake is similar to that of $EXT0_{st}$ wake (figures 3.9 (a) and 3.10 (a)) except at the edges of the wake. With the increase in the intensity of the external turbulence to 3% and 4%, $t.k.e.$ in the wake core exhibits a higher value as compared to case $EXT0_{st}$. Analysis of the $t.k.e.$ budget, discussed later, shows that shear production is enhanced and that turbulent transport from the wake to the background is reduced in the presence of external turbulence, thus keeping $t.k.e.$ larger in the wake core. As time advances, the horizontal expansion of the wake is significantly higher for the cases with 3% and 4% external turbulence as compared to cases $EXT0_{st}$ and $EXT1_{st}$ (Figure 3.9 (b)). The vertical spread of the wake is strongly suppressed by buoyancy in

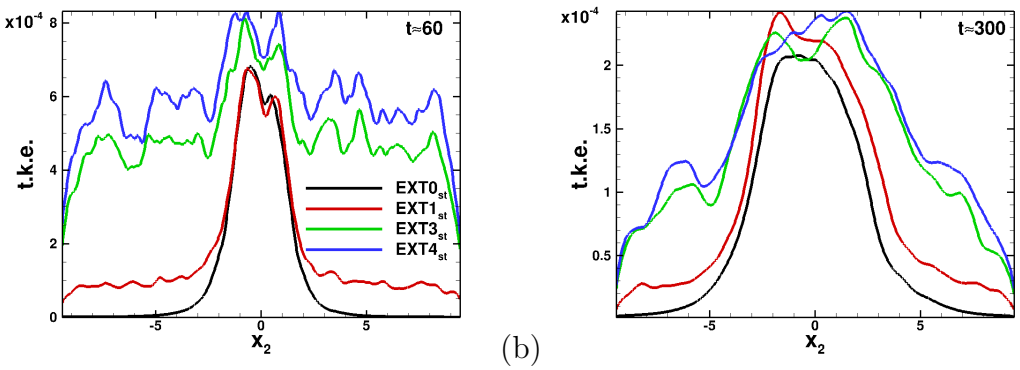

(a) (b)

Figure 3.9: Turbulent kinetic energy at the central line in the *horizontal* direction for the stratified cases: (a) $t \approx 60$ and (b) $t \approx 300$.

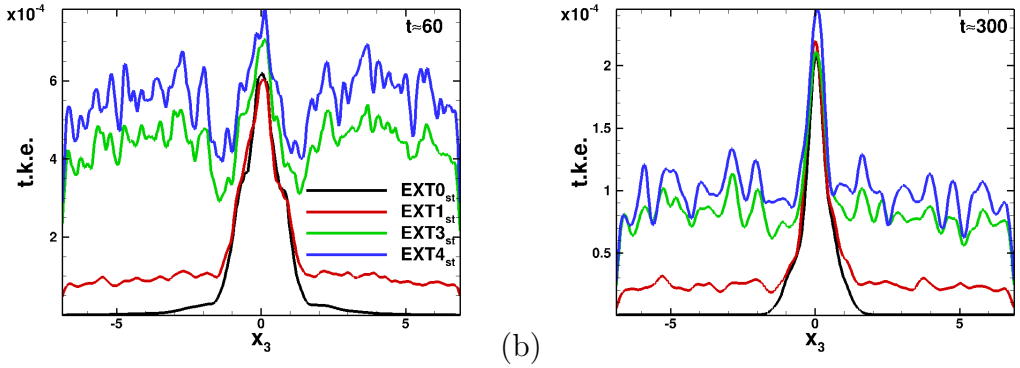

(a) (b)

Figure 3.10: Turbulent kinetic energy at the central line in the *vertical* direction for the stratified cases: (a) $t \approx 60$ and (b) $t \approx 300$.

all cases and is relatively unaffected by the background turbulence. Furthermore, in contrast to the horizontal profiles, the vertical profiles show a distinct break between the almost-uniform level of background turbulence and the higher level of wake turbulence reinforcing the notion that buoyancy strongly inhibits vertical entrainment in the cases simulated here.

Figures 3.11 (a)–(b) show the time evolution of $t.k.e.$, the *area-integrated* turbulent kinetic energy, normalized by its initial values for the unstratified and stratified cases, respectively. The area of integration is again taken to be the half-width region so as to focus on the wake core. The integrated $t.k.e.$ in the unstratified situation (figure 3.11 (a)) increases until $t \approx 18$ at a similar rate among

all cases, commences to decay after $t \approx 18$ with a rate that is again similar among the cases until $t \approx 200$ when some differences appear among cases. In the stratified cases (figure 3.11 (b)), the integrated $t.k.e$ evolves similarly until $Nt \approx 10$ for all the cases. The oscillations observed in the evolution of the $t.k.e.$ are due to the oscillations in the buoyancy flux responsible for reversible exchange between the potential and kinetic energy. Subsequently, the $t.k.e$ for case $EXT1_{st}$ continues to decay at a rate similar to that of the $EXT0_{st}$, but the decay of the $t.k.e$ slows down as the intensity of the background turbulence is increased to 3% and 4%. The reason for this behavior is the enhanced horizontal entrainment of the fluctuating energy from outside the wake which is also consistent with the formation of larger vortices in the NEQ regime in these cases as was seen in the earlier section on visualizations. The increased level of $t.k.e.$ in the cases with higher external turbulence level is also consistent with the increased level of turbulent production, P.

Figure 3.12 (a)–(b) represent the evolution of the half-width area for the unstratified and stratified cases, respectively. Case $EXT0_{unst}$ shows a scaling of approximately $t^{2/3}$ for the half-width area which is in agreement with scaling of $t^{-2/3}$ for the defect velocity. The cases with the external turbulence also follow an approximately similar scaling. In the stratified cases, the half-width area increases similar to the unstratified cases until $Nt \approx 5$. During $5 < Nt < 10$, there is a plateau in the half-width area indicative of the suppression of entrainment in the vertical direction owing to the effect of buoyancy. Beyond $Nt \approx 10$, entrainment resumes in the horizontal direction and the half-width continues to grow. Enhanced horizontal entrainment in the presence of background turbulence leads to an increase in the half-width area for the cases $EXT3_{st}$ and $EXT4_{st}$ as compared to $EXT0_{st}$ and $EXT1_{st}$.

The characteristics of external turbulence relative to wake turbulence during the evolution have been examined (but not plotted here) in the unstratified cases. The external and centerline values of $t.k.e.$ decay initially at different rates but

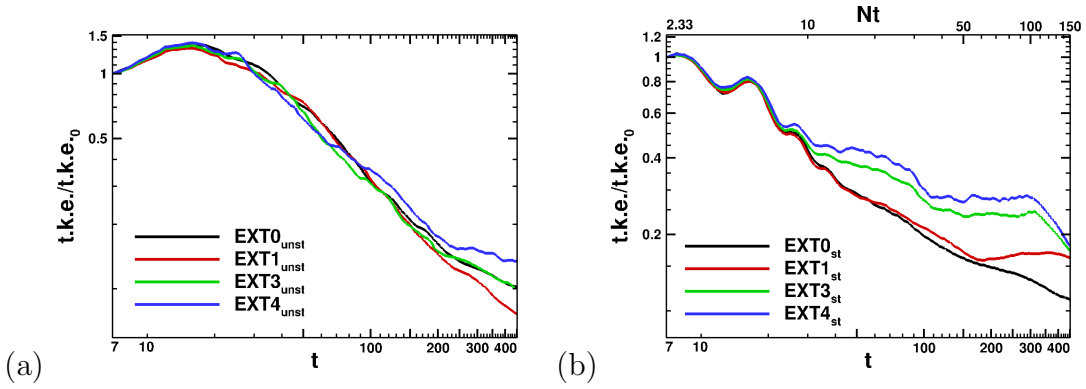

Figure 3.11: Turbulent kinetic energy integrated over the half-width (a) Unstratified cases, (b) Stratified cases.

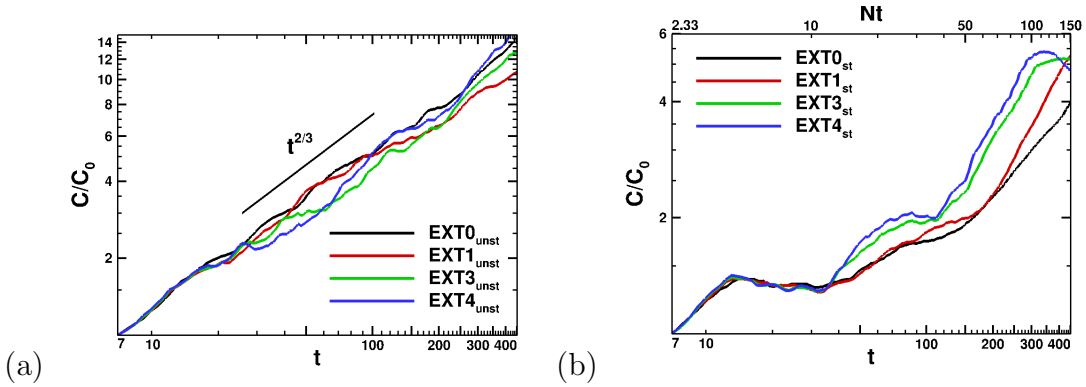

Figure 3.12: Half-width area (a) Unstratified cases, (b) Stratified cases.

eventually decay at a similar rate of approximately $t^{-1.4}$. The ratio, $t.k.e._{ext}/t.k.e_{cl}$, approaches an approximately constant value in each case that varies among cases (from 1.25 in $EXT1_{unst}$ to 2.5 in $EXT4_{unst}$). The relative evolution of integral length scales of turbulence (is also of interest. We find that the integral length scales of both wake turbulence and external turbulence decrease during an initial transient, $t < 50$. Interestingly, as a result of the initial transient, the value of $l_{int,ext}/l_{int,cl}$ which initially varied between 0.47 ($EXT1_{unst}$) and 1.56 ($EXT4_{unst}$) among cases approaches the value of unity. Later, the length scales increase with time and there is some difference in the background/wake turbulence length scale ratio among cases at late time, e.g. $l_{int,ext}/l_{int,cl}$ is ~ 0.5 in $EXT1_{unst}$ and ~ 1 in $EXT4_{unst}$.

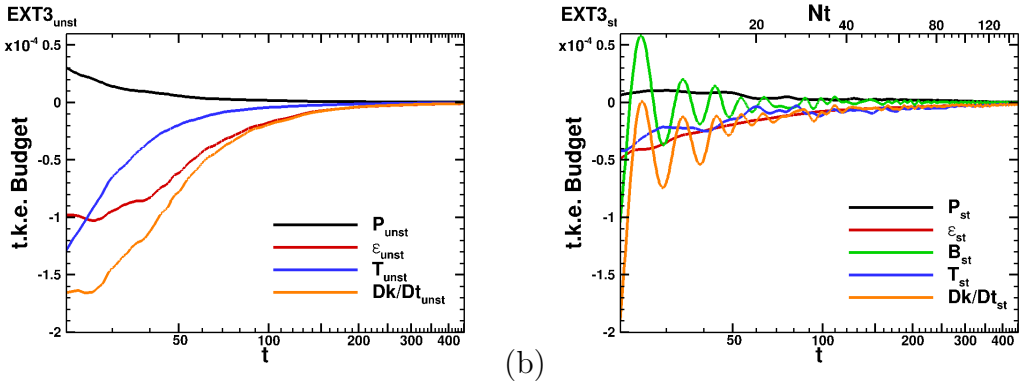

Figure 3.13: TKE Budget integrated over the half-width for the cases (a) $EXT3_{unst}$, (b) $EXT3_{st}$.

3.6 TKE Budget

The evolution of the turbulent kinetic energy $t.k.e. = \langle u_i' u_i' \rangle / 2$ is given by

$$\frac{D(t.k.e.)}{Dt} = P + B - \varepsilon - \frac{\partial T_i'}{\partial x_i}\,, \tag{3.6}$$

where P is the production, B is the buoyancy flux, ε is the turbulent dissipation rate and T_i' is the transport term. The evolution of $t.k.e.$, the turbulent kinetic energy integrated over the half-width area, was shown previously. The balance of terms resulting in the evolution of $t.k.e.$ is of interest and has been obtained by integration over the half-width area of terms in (4.10). Figure 3.13 (a) illustrates the balance for the unstratified case with 3% external turbulence. The production, P, is initially large but soon the spatial transport of $t.k.e.$, $\frac{\partial T_i'}{\partial x_i}$, and dissipation, ε, dominate. By $t = 100$, the turbulent dissipation rate dominates all other terms and is balanced by the time-derivative term. The main differences in the stratified case are as follows: the reduced magnitude of all the terms, the reduced value of shear production relative to other terms, the transport term remains comparable to the turbulent dissipation term beyond $t = 100$, and the presence of the buoyancy term, B which exhibits large temporal oscillations between positive and negative values making it comparable to the other terms in the balance for $t < 50$. The oscillation of B also leads to an oscillatory modulation of $\frac{D(t.k.e.)}{Dt}$ term in the balance. However, the time integrated value of the buoyancy flux is much smaller

than the corresponding value for turbulent dissipation.

Figure 3.14 (a) shows the $t.k.e.$ shear production components, P_{12} and P_{13}, integrated over the half-width area and normalized by their initial values. Here, P_{12} is associated with horizontal mean shear, $\partial\langle U_1\rangle/\partial x_2$, and P_{13} with vertical mean shear, $\partial\langle U_1\rangle/\partial x_3$. P_{12} decreases at a similar rate for all the cases until $Nt \approx 9$. During $9 < Nt < 20$, P_{12} is enhanced in cases $EXT3_{st}$ and $EXT4_{st}$ relative to the other cases. The increased levels of P_{12} in cases $EXT3_{st}$ and $EXT4_{st}$ are consistent with the enhancement of Reynolds shear stress in these cases shown earlier in figure 3.8 (a). An increase in P_{12} also signifies an increase in the extraction of energy from the mean velocity field leading to the faster decay of the mean velocity that was noted earlier for the stratified cases with background turbulence. The evolution of P_{13} shows little difference among cases. The P_{12} component remains positive at all times whereas P_{13} decreases to a negative value at $Nt \approx 4$ indicating a transfer of energy from the fluctuating modes to the mean streamwise velocity. P_{13}, after achieving a minimum value at $Nt \approx 6$, evolves towards zero in all cases. Figure 3.14 (b) compares the turbulent dissipation rate, integrated over the half-width area and normalized by the initial value, among the various stratified cases. During the early evolution until $Nt \approx 10$, case $EXT0_{st}$ exhibits values that are higher than the cases with external turbulence. Beyond $Nt \approx 10$, the dissipation rate for the cases with 3% and 4% external turbulence is larger relative to the cases $EXT0_{st}$ and $EXT1_{st}$. The enhanced values of ε in cases $EXT3_{st}$ and $EXT4_{st}$ are consistent with the entrainment of external fluid with energetic, smaller-scale fluctuations. Case $EXT1_{st}$, owing to lower intensity of external turbulence, shows little change with respect to $EXT0_{st}$.

The horizontal and vertical components of the transport of the $t.k.e.$, again integrated over the half-width area and normalized by their initial values, are presented in Figure 3.14 (c). The sum of the components, i.e., the divergence of the transport term is always negative when integrated over the half width region, which implies the direction of net transport of turbulence is from the core of the

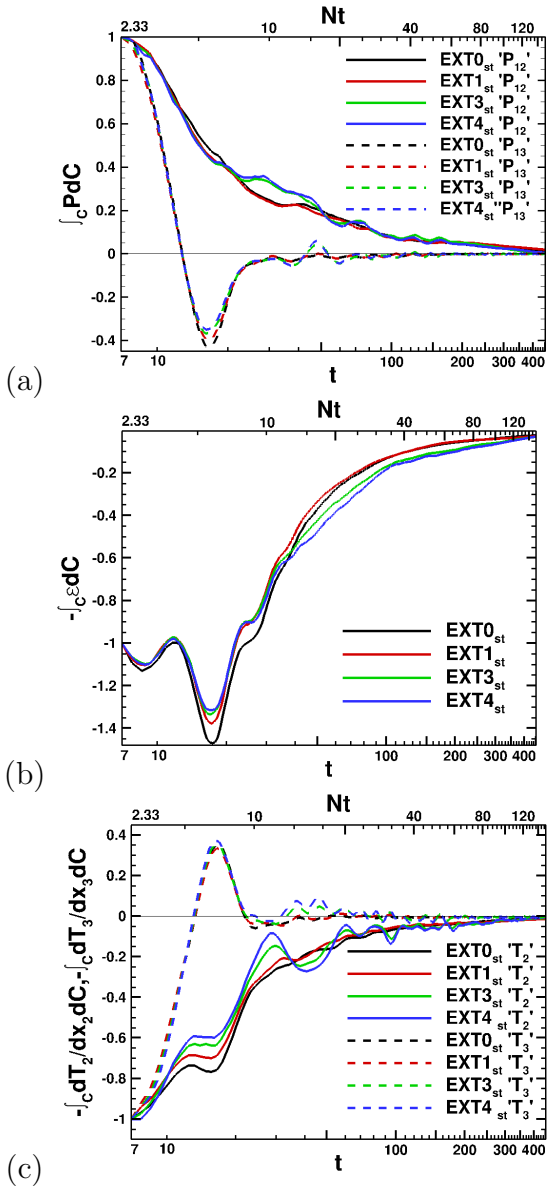

Figure 3.14: TKE Budget terms for the stratified cases integrated over the half-width (a) production components, (b) dissipation and (c) transport components.

wake to its lateral and vertical flanks. The background turbulence in the simulated cases is not strong enough to change this typical feature of turbulent shear flows. Background turbulence has little effect on the contribution of the vertical gradient, integrated over the half-width area. However, turbulent transport by horizontal gradients is diminished in cases $EXT3_{st}$ and $EXT4_{st}$. Entrainment of background fluctuations increases the turbulence level at the outer flanks of the wake (figure 3.9) reducing the net turbulent transport from the wake core to the flank.

3.7 Discussion of the evolution of mean wake velocity

In the present simulations of the unstratified wake, the defect velocity, $U_0(t)$, decays at a rate similar to the classical $t^{-2/3}$ law and the influence of external turbulence is weak. In contrast, Rind & Castro (2012*a*) found a significantly faster decay of U_0 when external turbulence had levels similar to the $u'_{ext} = 3\%$ and 4% cases considered here. The reasons for this difference are examined in the present section.

The primary independent parameters in the present problem are taken to be the levels of external turbulence level, u'_{ext}, the wake deficit velocity, U_0, and wake turbulence, u'_{cl}, all obtained at the time when the combined wake is initialized. The resulting nondimensional parameters are u'_{ext}/U_0 and u'_{ext}/u'_{cl}. As shown by Rind & Castro (2012*a*), the effect of external turbulence on the mean wake velocity strengthens when u'_{ext}/U_0 increases. We hypothesize that u'_{ext}/u'_{cl} is also important because of the following considerations. As discussed in section 3.4, it is the turbulent production, P, that is the dominant sink in (3.5), the transport equation for $m.k.e.$ The Reynolds shear stress appearing in P is quadratic in velocity fluctuations. In the undisturbed wake, $P \propto u'^2$ where u' is the level of wake turbulence. External turbulence provides a turbulence reservoir that can maintain turbulence fluctuations in the wake by decreasing the transport of turbulence away from the wake and increasing shear production. The increase in P owing to external

fluctuations with level u'_e can be estimated for the combined wake as

$$\delta P \approxeq \alpha_1 u' u'_{ext} + \alpha_2 {u'_{ext}}^2 \approxeq u'^2 \left(\alpha_1 \frac{u'_{ext}}{u'} + \alpha_2 (\frac{u'_{ext}}{u'})^2 \right) .$$

Our objective is to understand how the parameters related to mean and fluctuating velocity at the point of initialization of the combined wake change the subsequent evolution of the wake mean field. To do so, we assume that the change δQ in the cumulative integrated production, $Q = \int_0^t \int_C P dC dt$, which was introduced earlier is solely due to δP and estimate u'_{ext}/u'_{cl} using initial values to give

$$\frac{\delta Q}{t.k.e._0} \approxeq \beta_1 \frac{u'_{ext}}{u'_{cl}} + \beta_2 \left(\frac{u'_{ext}}{u'_{cl}} \right)^2 \tag{3.7}$$

In general, the coefficients β_1 and β_2 are *not* universal and, in particular, can depend on the state of development of the wake at the point of initialization of the combined wake. The arguments leading to (3.7) apply to stratified wakes too with the understanding that β_1 and β_2 depend additionally on Fr.

Rind & Castro (2012*a*) combine background fluctuations when the wake is in an approximately self-similar state ($t \approx 60$) while we do so in the near-wake region where the turbulent fluctuations are considerably stronger. Case RC4 (our nomenclature for their case with $u'_{ext}/U_0 = 0.36$) shown in Table 3.2 has a value of u'_{ext}/U_0 similar to our original case $EXT4_{unst}$ where $u'_{ext}/U_0 = 0.4$. However, case RC4 has $u'_{ext}/u'_\delta = 1.25$ which is higher than the corresponding value of 0.87 in $EXT4_{unst}$. This higher level of external turbulence relative to wake turbulence, and the fact that β_1 and β_2 depend on the state of wake turbulence (self-similar in contrast to early time) during combination is perhaps responsible for the substantially larger effect of external fluctuations found by Rind & Castro (2012*a*).

New cases with $Re = 10,000$ are simulated to support the preceding arguments. In order to establish that u'_{cl} plays a role in how the wake evolution is affected by background fluctuations, new simulations (series 2) with the same U_0 as the original series 1 but with lower u'_{cl} are performed. A wake without external

Table 3.2: Parameters relevant to the discussion of section 3.7 on the decay of the mean wake in unstratified flow. $RC4$ denotes a case from Rind & Castro (2012a).

$Cases$	U_0	u'_{cl}	u'_{δ}	u'_{ext}	$\frac{u'_{ext}}{U_0}$	$\frac{u'_{ext}}{u'_{\delta}}$	$\frac{u'_{ext}}{u'_{cl}}$
$RC4$	0.083	-	0.024	0.030	0.36	1.25	-
Series 1	0.1	0.044	0.047	0.01-0.072	0.10-0.72	0.22-1.53	0.23-1.64
Series 2	0.1	0.023	0.029	0.01-0.040	0.10-0.40	0.43-1.72	0.23-1.64

turbulence, $EXT0_{2,unst}$, and the same wake parameters as series 2 is also simulated so as to provide a baseline. In our original series 1 of unstratified wake simulations, the effect of external turbulence was found to be weak. This is somewhat surprising given (3.7) and the results reported by Rind & Castro (2012a). Therefore, we continue series 1 with two new cases where the external turbulence level is raised to 5% and 7% of the freestream velocity.

The velocities given in the columns 2-5 of table 3.2 are normalized with U, the freestream velocity relative to the body. In order to compare with Rind & Castro (2012a) who use the r.m.s. velocity fluctuation at the wake halfwidth, u'_{δ}, to characterize wake turbulence we give values of u'_{δ} in addition to u'_{cl}. Series 1 is the original series of simulations where u'_{ext} = 1 - 4 % of U plus additional simulations with larger u'_{ext} = 5% and 7%. Series 2 is a new series where the wake has a lower level of centerline turbulence, $u'_{cl} = 2.3\%$ relative to the 4.4% of series 1.

Figure 3.15(a) shows that the case $EXT4_{2,unst}$ with 4% external turbulence in the new series exhibits a substantial decrease in wake defect velocity relative to the uniform freestream case $EXT0_{2,unst}$, while the original case with $EXT4_{2,unst}$ with 4% external turbulence that was shown in figure 4.5(a) exhibited a small influence of external turbulence. This result supports the hypothesis that the wake turbulence level, u'_{cl}, plays an important role. It is also of interest to compare the new towed wake with 0% external turbulence case, $EXT0_{2,unst}$ with the original $EXT0_{unst}$. Case $EXT0_{2,unst}$ has smaller u'_{cl} leading to smaller turbulent production, smaller extraction of turbulence from the mean and, therefore, higher defect

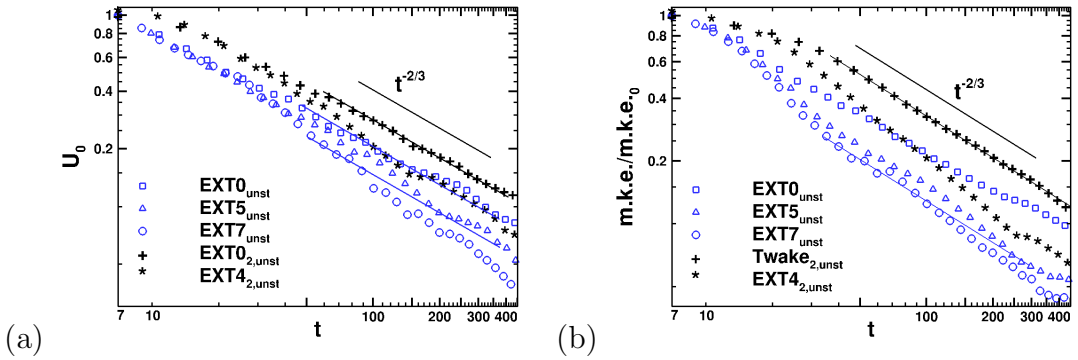

Figure 3.15: Effect of external fluctuations on mean wake velocity in unstratified wakes. (a) Center line defect velocity, and (b) Integrated mean kinetic energy.

velocity relative to $EXT0_{unst}$. Nevertheless, both cases (particularly $EXT0_{2,unst}$) exhibit $U_0 \approx t^{-2/3}$ scaling that is anticipated from similarity theory of the far wake. In contrast to the small change of $U_0(t)$ in the u'_{ext}= 4% case of series 1, the new series 1 cases with u'_{ext}= 5% and u'_{ext}= 7% shown in figure 3.15(a) exhibit lower levels of $U_0(t)$ compared to the uniform freestream case, consistent with the result of Rind & Castro (2012a) that, with increasing u'_{ext}, the decay of $U_0(t)$ is enhanced and deviates from the $t^{-2/3}$ law. The effect of external turbulence on the area-integrated $m.k.e.$ (figure 3.15b) is similar to that on the defect velocity U_0. One difference is that the evolution of $U_0(t)$ deviates later than $m.k.e.$ from the corresponding uniform freestream case, consistent with the expectation that the effect of external turbulence on wake dynamics needs time to propagate from the wake flanks to its core.

External turbulence affects the evolution of mean wake velocity by changing the turbulent production. Results from series 1 ($u'_{cl}/U_0 = 0.044$) are shown using solid lines with black, blue, cyan and orange lines representing 0, 4, 5 and 7 % levels of u'_{ext}, respectively. Results from series 2 ($u'_{cl}/U_0 = 0.023$) are shown using dash-dot lines with black, red, green, magenta and blue lines represent 0, 1, 2, 3 and 4 % levels of u'_{ext}, respectively. Figure 3.16 shows that the cases where the wake mean velocity is reduced by the presence of external turbulence also show an increase in cumulative turbulent production $Q(t)$. It can also be seen that the

effect of external turbulence in increasing $Q(t)$ from the corresponding uniform freestream case becomes significant at $u'_{ext} = 3$ % in series 1 relative to $u'_{ext} = 5$ % required in series 2.

The deviation of the external turbulence cases with respect to the baseline is quantified by the change, δQ_f, of the long-time value of Q_f (evaluated at $t \approx 450$) with respect to Q_f in the corresponding uniform freestream case. The value of $\delta Q_f / t.k.e._0$ depends strongly on u'_{ext}/u'_{cl} in both unstratified and stratified cases as shown by figures 3.17(a) and (b), respectively. In the unstratified cases, there is little change in turbulent production (therefore, mean velocity evolution) until $u'_{ext}/u'_{cl} > 1$. Once the threshold of $u'_{ext}/u'_{cl} \cong 1$ is exceeded, there is strong transport of turbulence from the exterior into the wake allowing δQ to increase sharply. Similar behavior is also observed in the stratified cases with $Fr = 3$. The lines in figures 3.17 (a)-(b) are best fit curves of the quadratic function, (3.7), and provide a reasonable fit to the simulation data. It is worth noting that, in series 1, δQ_f takes small negative values when $u'_{ext}/u'_{cl} < 1$. In all cases, $P(t)$ is enhanced by external fluctuations during the early evolution but, later, $P(t)$ is reduced because of the mean velocity feedback, i.e., the wake spread rate increases, decreasing the mean shear and, eventually, decreasing $P(t)$. In the cases with negative value of δQ_f (figure 3.17 (a)), the late-time reduction of $P(t)$ wins.

Upon normalization by Q_f, the effect of external turbulence becomes even more substantial, e.g. the $EXT4_{st}$ cases in series 1, $Fr = 3$ with $u'_{ext}/u'_{cl} \approx 1$, has $\delta Q_f / Q_f = 0.14$, a higher value than the $\delta Q_f / t.k.e._0 = 0.05$ in figure 3.17 (b). Since Q_f is essentially the change in integrated MKE for the clean wake without external turbulence, it is the value of $\delta Q_f / Q_f$ that effectively measures the relative deviation of mean wake velocity from the clean wake evolution.

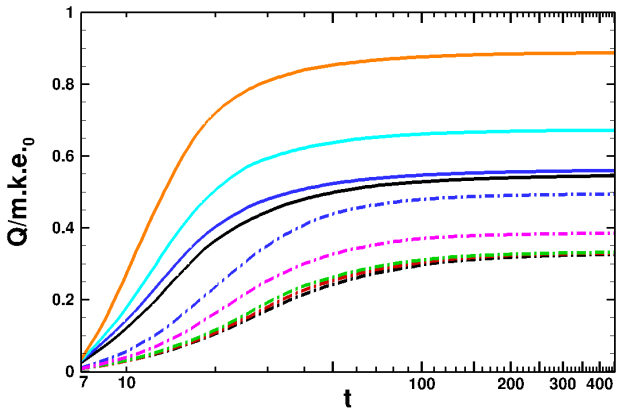

Figure 3.16: Cumulative area-integrated value of turbulent production normalized by the initial integrated mean kinetic energy.

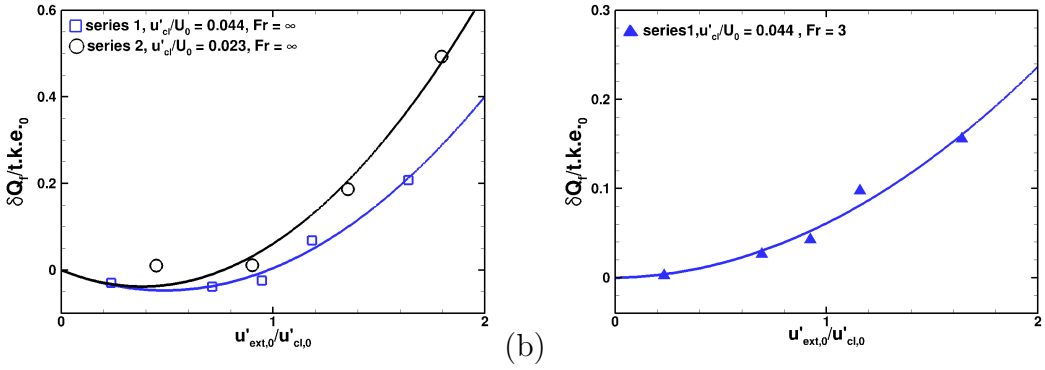

Figure 3.17: The influence of u'_{ext}/u'_{cl} at the initialization of the combined wake on the external turbulence effect: a) Unstratified Cases, (b) Stratified cases.

3.8 Conclusions

Towed wakes at $Re = 10,000$ have been examined using direct numerical simulation in a temporally evolving framework in order to study the influence of background turbulence on the evolution of wakes. Although simulations are conducted for both unstratified and stratified cases, the primary focus is on stratified wakes. The ratio of integral length scale of the external background turbulence to that of the wake turbulence is O(1). The r.m.s. intensity of the background turbulence, u'_{ext}, is systematically varied in the simulations. The effect of background turbulence is discussed using visualizations, turbulence statistics and analysis of the $t.k.e$ (turbulent kinetic energy) balance equation.

Background turbulence at 1% has little effect on the spatial organization of the stratified wake except for one aspect: the spatial pattern of internal waves, an important feature characterizing stratified wakes, is disrupted even at this low turbulence level. However, the organization of horizontal motion into coherent pancake vortices which is a defining characteristic of strongly stratified turbulence is robust to the presence of external turbulence. Owing to buoyancy, the decaying background fluctuations also organize into vortical structures which interact with the wake vortices leading to a larger lateral spread of the wake vortices. Horizontal $x_1 - x_2$ cuts and vertical $x_1 - x_3$ cuts of velocity and the vorticity normal to the plane show large scale coherent structures. It is worth noting that, because the external fluctuations are also organized into pan-cake vortices, planar cuts of normal vorticity do not clearly show the presence of the late time wake when the background turbulence is larger or equal to 4%. In contrast, planar cuts of the velocity show the presence of the late-time wake.

The evolution of the centerline defect velocity in all the stratified wake cases shows the different regimes, namely, near wake (NW), non equilibrium (NEQ) and quasi two-dimensional (Q2D) with their characteristic decay laws that have been found in several previous studies of wakes in a quiescent background. Despite the presence of external turbulence, the centerline defect velocity remains substantially

higher than the corresponding unstratified cases, that is, stratified wakes continue to have longer lifetimes.

External turbulence has an important effect on the mean defect velocity, $U_0(t)$. When u'_{ext} exceeds 3% in the $Fr = 3$ cases, $U_0(t)$ eventually becomes substantially smaller relative to the uniform freestream case. The turbulence production by shear also increases and the consequent enhancement of transfer from mean to turbulent kinetic energy leads to a decrease in mean velocity. The r.m.s fluctuation profiles also become wider in the lateral, horizontal coordinate. There is little change in the vertical centerline profiles of mean and turbulence quantities showing that the stabilizing effect of buoyancy remains dominant. The area-integrated turbulent kinetic energy becomes larger with increasing u'_{ext}.

External turbulence induces a faster decay of the mean wake in both unstratified and stratified wakes. For a given intensity of external turbulence, the stratified cases show a stronger relative change of mean velocity. The discussion of section 3.7 leads to the following conclusion. For both unstratified and stratified wakes, the parameter, u'_{ext}/u'_{cl} which measures the intensity of the external turbulence relative to wake turbulence is the key parameter that governs the influence of external fluctuations. There is a rapid increase in the cumulative turbulent production and, therefore, the mean wake decay when u'_{ext}/u'_{cl} exceeds a value of approximately unity. The present simulations were performed at $Re = 10,000$. However, the finding that external turbulence with length scale similar to wake turbulence substantially affects the wake dynamics when $u'_{ext}/u'_{cl} > 1$ is expected to be true at larger values of Re. The dependence of the cumulative turbulent production at a late time ($t \approx 450$) and, therefore, the decay of area-integrated mean kinetic energy up to that time, was found to have an approximately quadratic dependence on u'_{ext}/u'_{cl} for the cases examined here. u'_{ext}/u'_{cl} and u'_{ext}/U_0 are varied independently in the simulations, and u'_{ext}/u'_{cl} is found to be the key governing parameter. If the external turbulence is added when the wake is already in its self-similar state (when the ratio of centerline $r.m.s.$ velocity fluctuation to mean

defect velocity is constant in time) as in the simulations of Rind & Castro (2012a), then u'_{ext}/U_0 and u'_{ext}/u'_{cl} are not independent parameters.

Future work will be necessary to determine if our finding of $u'_{ext}/u'_{cl} > 1$ as a criterion for external turbulence to substantially change the mean wake velocity carries over to other background configurations. The relative value of turbulence integral scale, $l_{int,ext}/l_{int,cl}$, was O(1) in both the present study and that by Rind & Castro (2012a). Larger and smaller values of this ratio could be the subject of future study. The external turbulence chosen in the present work is isotropic turbulence that decays along with the wake. This simplified case is similar to that in wind tunnel experiments of a wake with grid turbulence providing the background fluctuations. It is possible that, if the background turbulence exhibits a much slower decay than wake turbulence, its effect on the wake would be stronger. The complexity of the flow behind the body where the external turbulent background mixes with the separating boundary layers and the near wake is not included in the present simulations. Therefore, future investigations that include the body will help evaluate the role of near wake dynamics on the effect of external turbulence on the intermediate-to-far wake.

3.9 Acknowledgements

Chapter 3, in full, is a reprint of the material as it appears in Journal of Fluid Mechanics (2015), coauthored by Professor Sutanu Sarkar. A. Pal & S. Sarkar, Effect of external turbulence on the evolution of a wake in stratified and unstratified environments *J. Fluid Mech.*, 772, 361-385 (2015). The thesis author was the primary author of this paper.

Chapter 4

DNS of stratified flow past a sphere at a Reynolds number of 3700.

4.1 Motivation

A temporal approximation requires an approximation of the initial fluctuations some distance from the body where the freestream velocity is much higher than the wake defect velocity. For moderately stratified wakes with $Fr = O(1)$, the transition to the NEQ regimes occurs with a few body lengths and the temporal approximation would require initial conditions very different from the customary choice that is based on unstratified flow. More generally, the somewhat *ad hoc* initial conditions used in the temporal simulations cannot be expected to capture the near-wake characteristics and the early NEQ regime since the details of the near-body flow could affect the vortex dynamics, turbulence and wave emission in that region. In temporal simulations, the results for the defect velocity decay rate in the NEQ regime of temporal simulations have some scatter with respect to the NEQ regime scaling of t^{-n} with $n = 0.25$ proposed by Spedding (1997). This discrepancy can be addressed by spatially evolving simulations that include the sphere. Spatial simulations with proper resolution near the body can also capture

Table 4.1: Simulation parameters.

$Case$	Re	Fr	L_r	L_θ	L_z	N_r	N_θ	N_z
1	3700	1	58	2π	105	692	128	4608
2	3700	2	58	2π	105	692	128	4608
3	3700	3	58	2π	93	692	128	4608
4	3700	∞	16	2π	93	632	128	4608

the boundary layer dynamics, the effect of vortex shedding on stratified wakes and help understand the evolution of the near wake into the NEQ regime, including the possible presence of the accelerated collapse identified by Bonnier & Eiff (2002).

The present study is a numerical investigation of flow over a sphere at moderate Reynolds number, $Re = 3700$, for which both DNS and experimental data is available for validation in the unstratified case. We focus on moderate stratification of $Fr = O(1)$ and simulates flows with $Fr = 1, 2, 3$ and ∞. To the authors best knowledge, this is the first numerical study of turbulent flow past a sphere in a stably stratified environment which resolves small scales near the body and systematically investigates buoyancy effects in the $Fr = O(1)$ regime on near, intermediate and far wake behavior. We simulate the flow up to a downstream length of $x_1/D \approx 80$, and quantify wake characteristics in the near and NEQ regime such as defect velocity and its scaling, turbulence levels and spectra, and compare the time-averaged turbulent kinetic energy TKE budget terms with the benchmark unstratified case. We defer a detailed discussion of internal wave properties to followup work.

4.2 Problem formulation

Turbulent wakes can be simulated either in a temporally evolving or in a spatially evolving model. In a temporal model, the wake is initialized by an assumed mean velocity profile with superposed turbulent fluctuations that satisfy a given spectrum, and the subsequent time evolution of the flow is captured in a domain with periodic boundary conditions in the streamwise direction. This method of simulating wakes is relatively inexpensive since the boundary layer and

its separation are not resolved and, therefore, higher Reynolds number and Froude numbers can be achieved (Brucker & Sarkar (2010); Diamessis *et al.* (2011)). Nevertheless, the flow is dependent on the type of initial conditions (the initial mean wake velocity profiles and the fluctuations), a limitation that can be overcome through spatially evolving simulations that include the body. Such DNS studies are expensive owing to the fine grid required to resolve the boundary layer near the body and are limited in practice to moderate Reynolds numbers and moderate domain size in the streamwise direction.

Table 6.1 shows the various simulation parameters including domain dimensions and grid dimensions. The sphere is embedded at the origin of a cylindrical computational domain, as shown by figure 4.1. High resolution is used at the sphere surface (20 points across the boundary layer thickness at the point of maximum wall shear stress) and in the wake. The radial grid spacing is $\Delta r \simeq 0.0016$ in the cylindrical region ($r < 0.65$) that encloses the sphere, the azimuthal direction has 128 points, and $\Delta z \simeq 0.0016$ near the surface. The grid has mild stretching, radially and streamwise, away from the body. The radial spacing is less than the Kolmogorov scale, η, over the entire wake. The streamwise grid spacing, after reaching about 1.5η near the body decreases to below η after $x_1/D \approx 60$. The azimuthal grid spacing, $r\Delta\theta$, at $r = 0.5$ has a maximum of approximately 4η in the separated shear layer at $x_1/D = 2$; the resolution then improves to 2.7η at $x_1/D = 5$ and to less than 2η by $x_1/D = 10$. Radially outward at $r = 2$, the resolution improves to $r\Delta\theta < \eta$ for all streamwise locations.

The downstream domain length for all the cases is ≈ 80. The domain is extended in the upstream direction to accommodate upstream wave propagation. For $Fr = 1$ and 2, an upstream distance of 25 is used relative to a shorter upstream length of 13 for $Fr = 3$ which has weaker body-generated waves. To prevent spurious reflection back into the domain from these upstream propagating body-generated waves and from the turbulence generated internal gravity waves, we use an inlet sponge and a cylindrical sponge at the domain boundary.

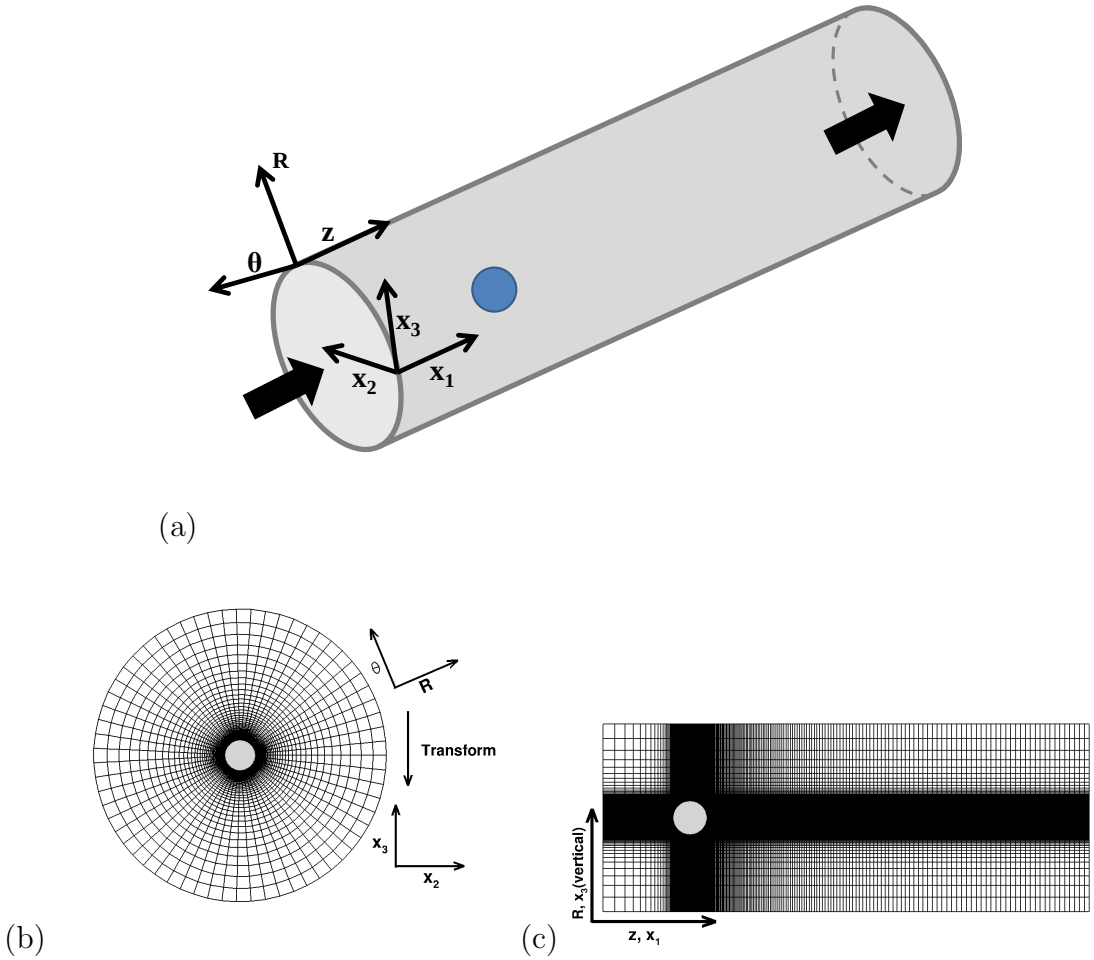

Figure 4.1: Schematic of simulation set up: (a) 3-D cylindrical domain with the sphere at $(0, 0, 0)$ and uniform inflow in the x_1 direction, (b) $R - \theta$ cross-section, skipping 5 points in r and 1 point in θ; (c) $R - z$ cross-section, skipping 10 points in both r and z directions.

4.2.1 Governing equations and numerical method

The governing equations are the three-dimensional incompressible, unsteady form of the conservation equations for mass, momentum and density, respectively, subject to the Boussinesq approximation for buoyancy. They take the following form in a cylindrical coordinate system:

$$\frac{1}{r}\frac{\partial(ru_r)}{\partial r} + \frac{1}{r}\frac{\partial(u_\theta)}{\partial \theta} + \frac{\partial u_z}{\partial z} = 0, \tag{4.1}$$

$$\frac{\partial u_r}{\partial t} + (\mathbf{u} \bullet \nabla)u_r - \frac{u_\theta^2}{r} = -\frac{1}{\rho_0}\frac{\partial p}{\partial r} + \nu(\nabla^2 u_r - \frac{u_r}{r^2} - \frac{2}{r^2}\frac{\partial u_\theta}{\partial \theta}) + \frac{\widetilde{\rho}}{\rho_0}g_r, \tag{4.2}$$

$$\frac{\partial u_\theta}{\partial t} + (\mathbf{u} \bullet \nabla)u_\theta + \frac{u_r u_\theta^2}{r} = -\frac{1}{\rho_0 r}\frac{\partial p}{\partial \theta} + \nu(\nabla^2 u_\theta - \frac{u_\theta}{r^2} + \frac{2}{r^2}\frac{\partial u_r}{\partial \theta}) + \frac{\widetilde{\rho}}{\rho_0}g_\theta, \tag{4.3}$$

$$\frac{\partial u_z}{\partial t} + (\mathbf{u} \bullet \nabla)u_z = -\frac{1}{\rho_0}\frac{\partial p}{\partial z} + \nu(\nabla^2 u_z), \tag{4.4}$$

$$\frac{\partial \rho}{\partial t} + (\mathbf{u} \bullet \nabla)\rho = \kappa(\nabla^2 \rho), \tag{4.5}$$

where u_r, u_θ and u_z are the velocities in the radial, azimuthal and the streamwise directions, respectively, $g_r = gsin\theta$ and $g_\theta = gcos\theta$ are the components of gravity (g) in the radial and azimuthal direction respectively and κ is the molecular diffusivity. The density is given by

$$\rho = \rho_{bg}(x_3) + \widetilde{\rho}(r, \theta, z, t), \tag{4.6}$$

where $\rho_b(x_3)$ is the fixed background density that varies linearly in the vertical direction x_3 and the density deviation, $\widetilde{\rho}(r, \theta, z, t)$, appears in the momentum equa-

tion. In the cylindrical coordinate system, $\rho_{bg}(x_3) = \rho_0 + \rho^*(r, \theta)$.

The governing equations are solved numerically in a cylindrical coordinate system on staggered grids. The sphere inside the domain is represented by an immersed boundary method following Yang & Balaras (2006); Balaras (2004). Use of a cylindrical coordinate system rather than a planar coordinate system improves approximation of the sphere surface and the gradients in the boundary layer. For the time advancement a semi-implicit, Runge-Kutta/Crank-Nicolson formulation is used, where all the terms in the azimuthal direction are treated implicitly to eliminate restrictions to the timestep due to small values of, $r\Delta\theta$ near the axis. All remaining terms are advanced explicitly. All spatial derivatives are discretized using central, second-order, finite difference scheme on a staggered grid. The pressure Poisson equation, which is utilized to project the velocity field into a divergence-free space, is solved using direct methods. In particular, trigonometric transforms in the azimuthal direction are used to reduce the problem into a set of penta-diagonal matrices, which are then solved directly with a divide and conquer strategy (Rossi & Toivanen (1999)). The velocities obtained by solving the governing equations are converted to Cartesian coordinates by using the following transformation:

$$\begin{bmatrix} u_1 \\ u_2 \\ u_3 \end{bmatrix} = \begin{bmatrix} 0 & 0 & 1 \\ \cos\theta & -\sin\theta & 0 \\ \sin\theta & \cos\theta & 0 \end{bmatrix} \times \begin{bmatrix} u_R \\ u_\theta \\ u_z \end{bmatrix} \tag{4.7}$$

where u_1, u_2 and u_3 are the velocities in the streamwise, horizontal and vertical directions respectively. The derivatives of a variable ϕ in the Cartesian coordinate system can be calculated from the corresponding derivatives in the cylindrical coordinate system as follows

$$\begin{bmatrix} \frac{\partial\phi}{\partial x_1} \\ \frac{\partial\phi}{\partial x_2} \\ \frac{\partial\phi}{\partial x_3} \end{bmatrix} = \begin{bmatrix} 0 & 0 & 1 \\ \cos\theta & \frac{-\sin\theta}{r} & 0 \\ \sin\theta & \frac{\cos\theta}{r} & 0 \end{bmatrix} \times \begin{bmatrix} \frac{\partial\phi}{\partial r} \\ \frac{\partial\phi}{\partial\theta} \\ \frac{\partial\phi}{\partial z} \end{bmatrix}. \tag{4.8}$$

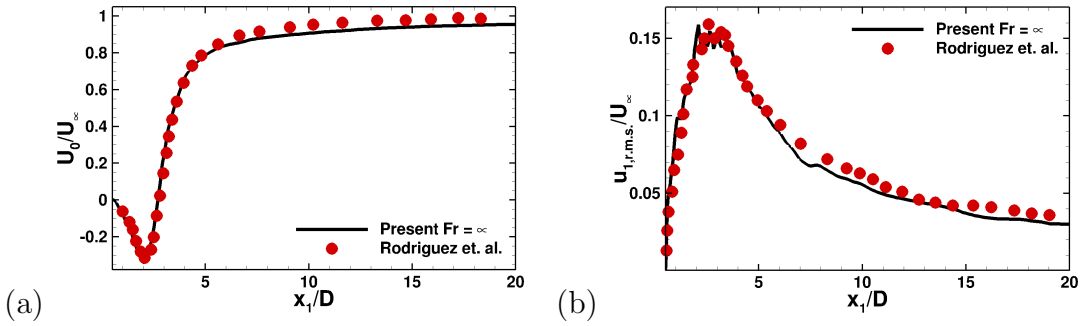

Figure 4.2: Validation of the unstratified wake. Streamwise evolution at the centerline ($x_2 = 0$ and $x_3 = 0$) of: (a) Mean defect velocity, and (b) r.m.s. streamwise velocity.

4.2.2 Calculation of statistics

Statistics are computed using time averaging of the data over an interval that spans approximately 80 non-dimensional time units ($\frac{tU_\infty}{D}$) after the flow has reached statistical steady state at approximately 120 time units. The Reynolds decomposition into mean and fluctuations is

$$u_i = \langle u_i \rangle + u_i^{'}, \rho = \langle \rho \rangle + \rho^{'}, p = \langle p \rangle + p^{'} \,. \tag{4.9}$$

Statistics in the stratified wake are a function of streamwise(x_1), horizontal (x_2) and vertical (x_3) directions. Each simulation is

Validation of the numerical method and grid resolution of the present DNS against previous experimental and numerical results are presented in Pal *et al.* (2016*b*). An excellent match is found for the vortex shedding frequency, $St = fD/U_\infty$, separation angle, φ_s, drag coefficient, C_d, rearward stagnation pressure coefficient, C_{pb}, profiles of the coefficient of pressure, C_p, and shear stress on the surface of the sphere with the previous investigations (Schlichting, 1979; Kim & Durbin, 1988; Sakamoto & Haniu, 1990; Seidl *et al.*, 1997; Tomboulides & Orszag, 2000; Constantinescu & Squires, 2003; Yun *et al.*, 2006; Rodriguez *et al.*, 2011) as discussed in Pal *et al.* (2016*b*). Comparison of the streamwise mean defect and $r.m.s.$ velocity at the centerline with Rodriguez *et al.* (2011) is very good as demonstrated by figure 4.2.

4.3 Visualization of the flow past a sphere

Figures 4.3 (a) and (b) show contour plots of the azimuthal vorticity in the vertical $x_1 - x_3$ centerplane for the $Fr = 1$ case at $0.5 < x_1/D < 30$ and $30 < x_1/D < 80$, respectively. The analogous plots for $Fr = 3$ are shown in figures 4.3 (c) and (d), respectively. The separating shear layer at $Fr = 1$ (figure 4.3 a) remains laminar and plunges towards the centerline at $x_1/D \approx 1.5$ owing to the strong restoring effect of buoyancy resulting in a significantly shorter recirculation region in comparison to the $Fr = 3$ (figure 4.3 c) case. Downstream of $x_1/D \approx 10$, the azimuthal vorticity takes a smooth two-layered form suggesting the decay of broadband fluctuations (confirmed by spectra). The evolution of azimuthal vorticity at $Fr = 3$ is qualitatively different. The shear layer is able to roll up before buoyancy forces a less abrupt but still noticeable plunge of the shear layer towards the centerline which, as shown by figure 4.3 (c), occurs at $x_1/D \approx 4.5$. Interestingly, for both $Fr = 1$ and 3, the curving of the shear layer towards the centerline occurs at the same value of buoyancy time, $Nt \approx 1.5$. Unlike the $Fr = 1$ case, the vorticity in figure 4.3 (c) has small-scale content throughout $0 < x_1/D < 30$. Phase lines indicative of internal wave emission from the wake into the background are seen for both cases. Closer inspection shows that the signature of the internal waves start at $x_1/D \approx 7$ for $Fr = 1$ and $x_1/D \approx 21$ for $Fr = 3$ as shown in figures 4.3 (a) and (c), respectively. In terms of the buoyancy period, this location corresponds to $Nt = 7$ for both $Fr = 1$ and 3, which is near the beginning of the NEQ regime. The properties of these wake generated waves will be described in a followup to the present work.

The azimuthal vorticity contour plots in the horizontal $x_1 - x_2$ centerplane for $Fr = 1$ at $0.5 < x_1/D < 30$ and $30 < x_1/D < 80$ are shown in figures 4.4 (a) and (b), respectively, and the corresponding plots for $Fr = 3$ are shown in figures 4.4 (c) and (d), respectively. The anisotropy of the wake, i.e. larger horizontal spread relative to the vertical spread, is evident in both cases and more so in the $Fr = 1$ case. Figure 4.4 (a) shows that the shear layer rolls up in the horizontal plane and becomes turbulent in contrast to the quasi-laminar behavior in the vertical plane. In general, there is stronger variability in the horizontal

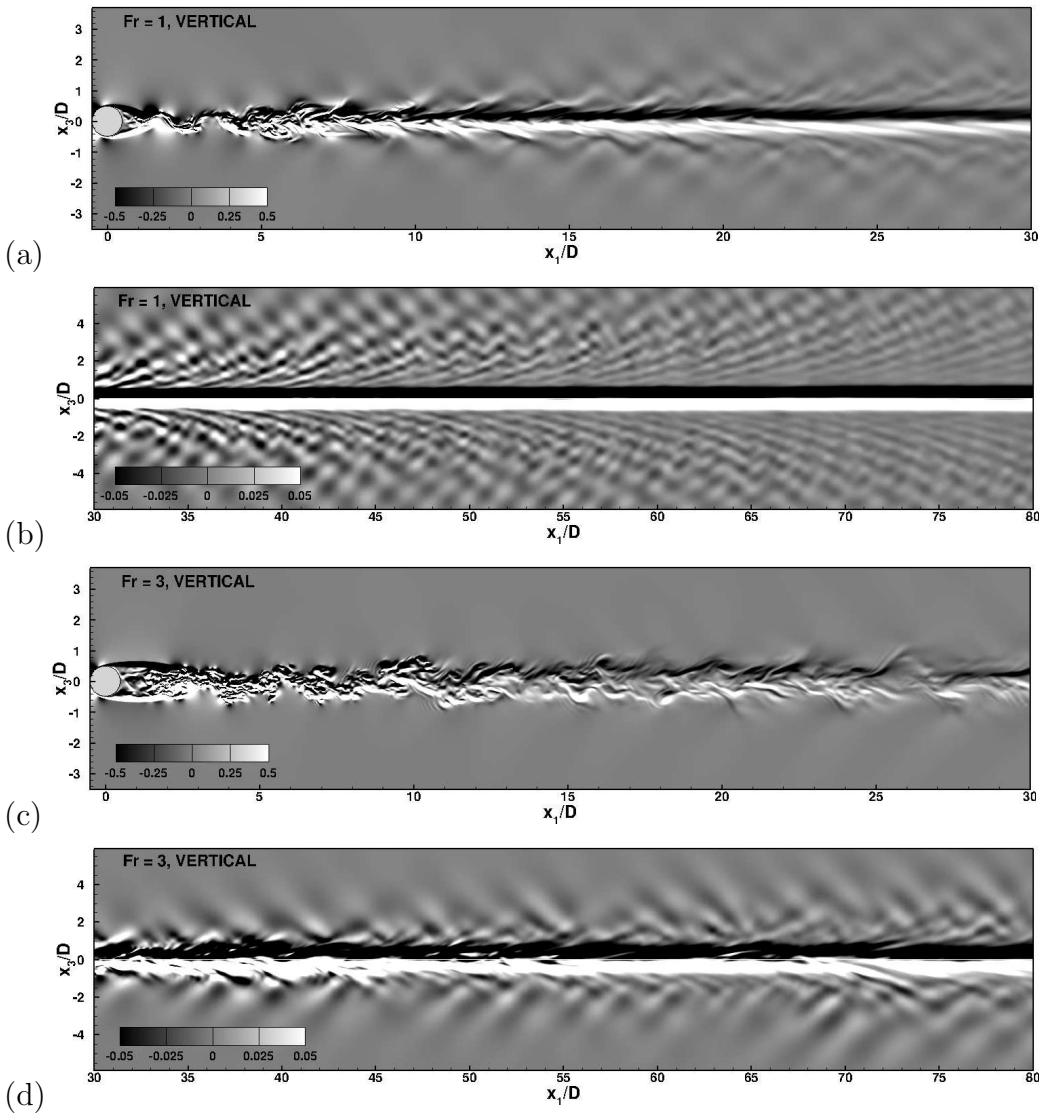

Figure 4.3: Instantaneous azimuthal vorticity on the vertical centerplane: (a) $Fr = 1$, $0.5 < x_1/D < 30$, (b) $Fr = 1$, $30 < x_1/D < 80$, (c) $Fr = 3$, $0.5 < x_1/D < 30$, and (d) $Fr = 3$, $30 < x_1/D < 80$.

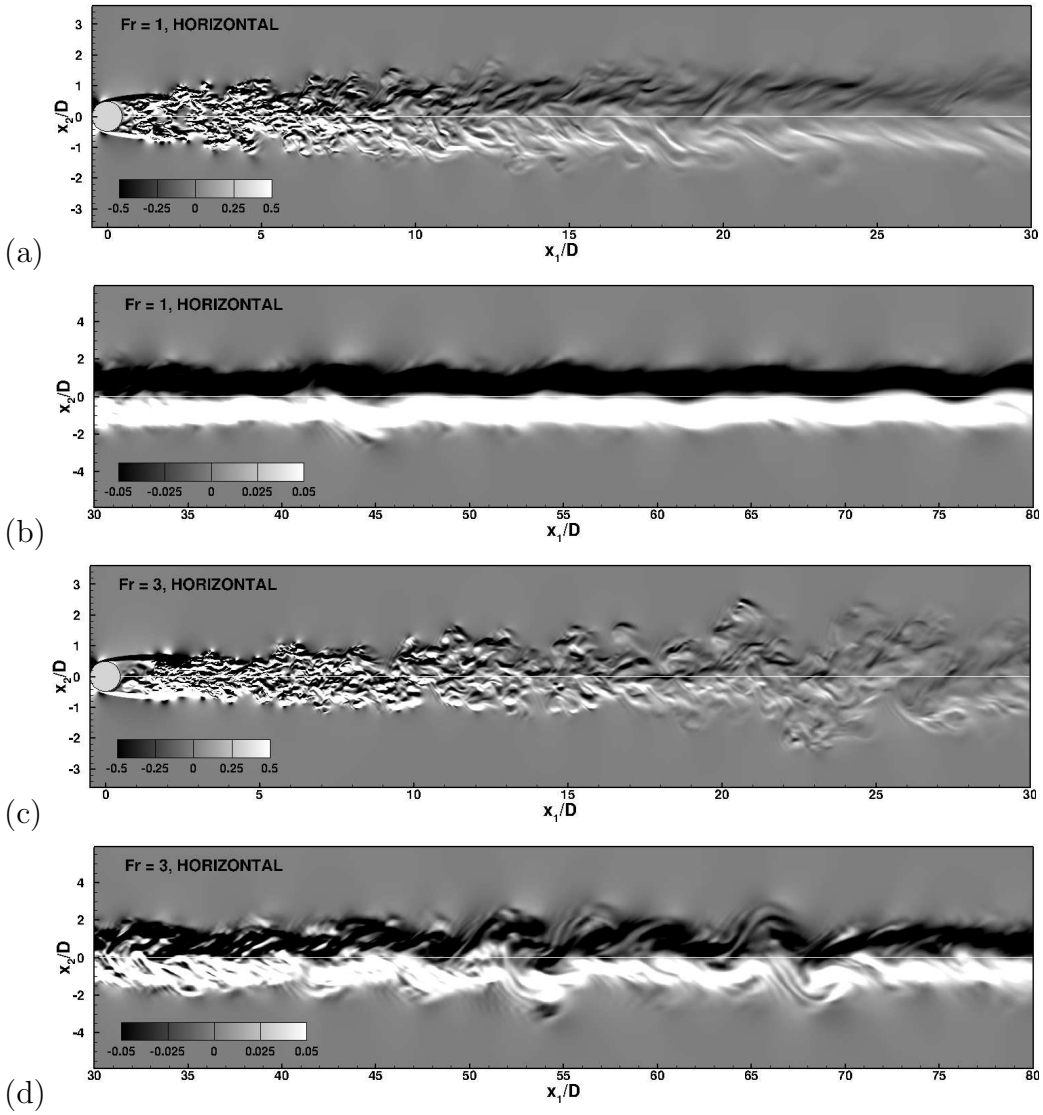

Figure 4.4: Instantaneous azimuthal vorticity on the horizontal centerplane: (a) $Fr = 1$, $0.5 < x_1/D < 30$, (b) $Fr = 1$, $30 < x_1/D < 80$, (c) $Fr = 3$, $0.5 < x_1/D < 30$, and (d) $Fr = 3$, $30 < x_1/D < 80$.

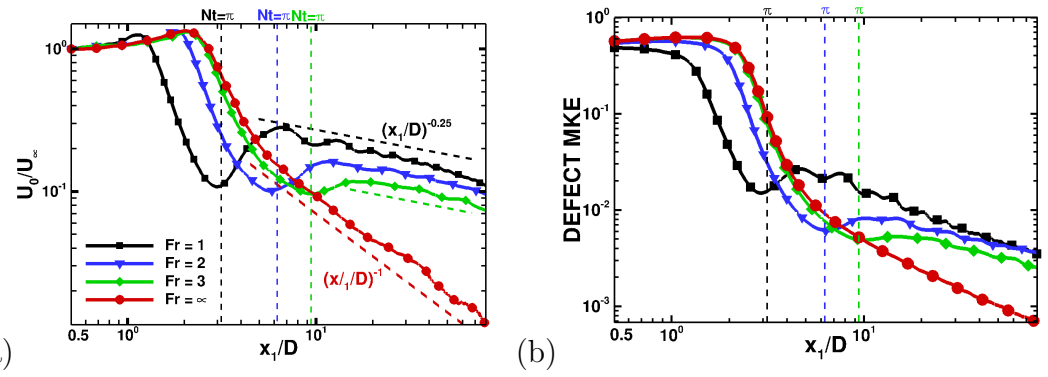

(a) (b)

Figure 4.5: (a) Defect velocity, U_0, at the centerline ($x_2 = 0$ and $x_3 = 0$), (b) Integrated defect mean kinetic energy (MKE).

motion relative to motion in the vertical plane. The vertical vorticity is organized into coherent vortical structures further downstream, $30 < x_1/D < 80$, in the Fr = 3 case. In contrast, the corresponding plot for $Fr = 1$ exhibits a quasi-steady double-layered distribution.

4.4 Mean flow

Figure 4.5(a) compares the evolution among the different cases of the mean defect velocity at the centerline, $U_0 = U_\infty - \langle U \rangle_c$, where U_∞ is the freestream velocity and $\langle U \rangle_c$ is the centerline streamwise velocity. The unstratified wake exhibits a monotone decay of the defect velocity, U_0, after the recirculation region. In the near wake sub-region that extends from the end of the recirculation region up to $Nt \approx \pi$, the stratified wakes also exhibit a decrease of U_0 with a rate that is similar to that in the unstratified case. Although U_0 at $Nt = \pi$ in the $Fr = 3$ case is similar to that of the unstratified case, the $Fr = 1$ and 2 wakes have significantly smaller U_0 at $Nt = \pi$ because the significantly shorter recirculation region in these wakes leads to a longer time interval for the wake deficit to decay. At $Nt = \pi$, as shown by the corresponding dotted lines in figure 4.5(a), we find that for $Fr = 1, 2$ and 3, the defect velocity achieves a local minimum. After $Nt \approx \pi$, U_0 starts increasing in the stratified cases. The acceleration of U_0 lasts until $Nt = \{2\pi, 2\pi, 5\}$ for the cases with $Fr = \{1, 2, 3\}$. The increase of U_0 during

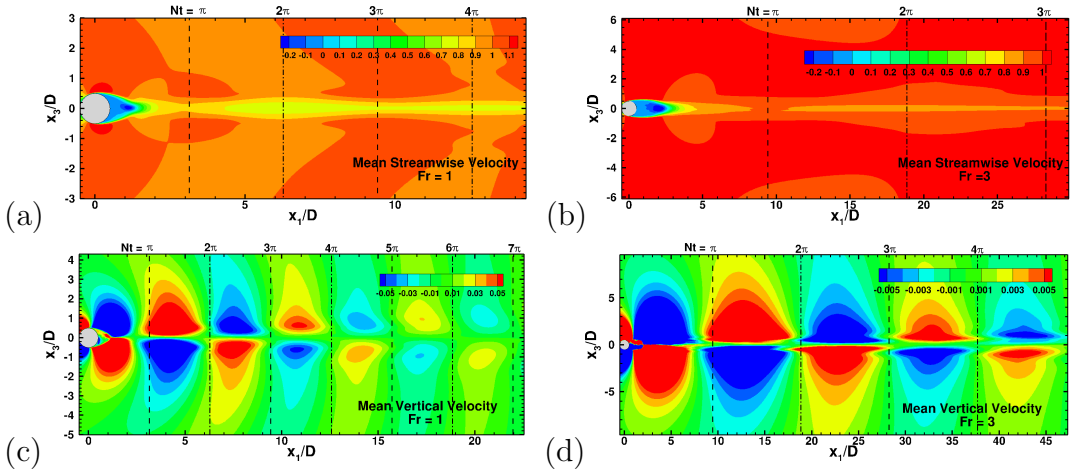

Figure 4.6: Contours of mean velocity on the vertical centerplane. The left column corresponds to $Fr = 1$ and the right column to $Fr = 3$. The streamwise velocity component is shown in parts (a) and (b), while the vertical component is shown in parts (c) and (d).

$\pi < Nt < 2\pi$ is prominent at $Fr = 1$, but becomes less so with increasing Fr. The experiments of Bonnier & Eiff (2002) also show a local minimum of U_0 followed by an abrupt increase. For $Fr = \{1.5, 3, 5\}$ and $Re = \{3400, 6900, 11500\}$, the increase of U_0 commenced at $Nt = \{3, 2.3, 1.8\}$ and lasted until $Nt = \{9, 7, 5\}$ in their experiments. The amplitude of the increase of U_0 is reduced with increasing Fr in the laboratory experiment as in our simulation.

The decrease/increase of defect velocity before/after $Nt = \pi$ occurs because of the imprint of the steady lee wave pattern, which has a wavelength of $Nt = \pi$ according to linear theory, on the stratified wake as explained below. Figures 4.6 (a)-(b) present the streamwise mean velocity $\langle U_1 \rangle$ on the vertical (x_1-x_3) centerplane for $Fr = 1$ and 3, respectively. It can be seen from figure 4.6 (a) that $\langle U_1 \rangle$ exhibits a non-monotone behavior at the centerline: it increases from $x_1/D \approx 1$ up to $x_1/D \approx \pi$, equivalently $Nt = \pi$, and then decreases up to the location of $Nt = 2\pi$. The velocity contour in the central region of the wake in figure 4.6 (a) shows a contraction in its vertical thickness until $Nt = \pi$ followed by an expansion. The contraction and expansion of this central wake region repeats between $2\pi, 4\pi$ and beyond with decreasing amplitude. A similar contraction/expansion is also observed at $Fr = 3$ for the same buoyancy time period, Nt, ranges as shown

in figure 4.6 (b). Thus, in both $Fr = 1$ and 3 wakes, $Nt \in [\pi, 2\pi]$ exhibits a decrease in mean velocity, equivalently an increase in mean defect velocity, as was noted as a wake collapse region with accelerated defect velocity by Bonnier & Eiff (2002) and also present in the simulations as was shown in figure 4.5(a). However, we note that the "collapse" in the sense of decrease in a characteristic vertical thickness occurs prior to the wake defect acceleration. Furthermore, the variation of the thickness of the central high-defect velocity region is oscillatory and is an effect of the body generated lee waves on the wake of the sphere. The background signature of the lee waves is clearly visible in figure 4.6 (a)-(b), particularly for the $Fr = 1$ flow. For the $Fr = 3$ case, the lee waves generated by the body are weak. To further clarify the lee wave effect, contours of mean vertical velocity, $\langle U_3 \rangle$, are shown in figure 4.6(c)-(d). From the edge of the sphere until $Nt \approx \pi$, the sign of $\langle U_3 \rangle$ shows a pattern of mean fluid convergence towards the centerline whereas, for $Nt \in [\pi, 2\pi]$, there is a pattern of fluid divergence, thereby corroborating the fact that the vertical contraction and expansion of the high-deficit velocity region is an imprint of the body generated lee waves. This periodic contraction-expansion behavior in moderate-Fr wakes can be termed as *oscillatory collapse* and occurs at intervals of $Nt \approx \pi$, which coincides with the half-wavelength of the lee waves.

At the end of the accelerated collapse region, the defect velocity for the stratified cases starts decaying again as shown in figure 4.5(a). The rate of decay follows a $(x_1/D)^{-0.25}$ law for the stratified wakes as in the NEQ regime reported by Spedding (1997) where U_0 was found to satisfy a $(x_1/D)^{-0.25}$ power law for wakes with $Fr \geq 5$. The present simulations suggest that the power law is applicable to lower-stratification wakes too with Fr going down to unity. It is worth noting that previous simulations with the temporal flow model have not shown a clear $(x_1/D)^{-0.25}$ power law.

Stratification prolongs the lifetime of the entire wake deficit, not just the centerline value, U_0. The streamwise evolution of the deficit mean kinetic energy (MKE) integrated over a $x_2 - x_3$ cross-section is plotted in Figure 4.5(b). High stratification (low Fr) systematically increases the deficit MKE in the NEQ regime.

The profiles of defect velocity, $U_0 = U_\infty - \langle U_1 \rangle$, in the spanwise and the

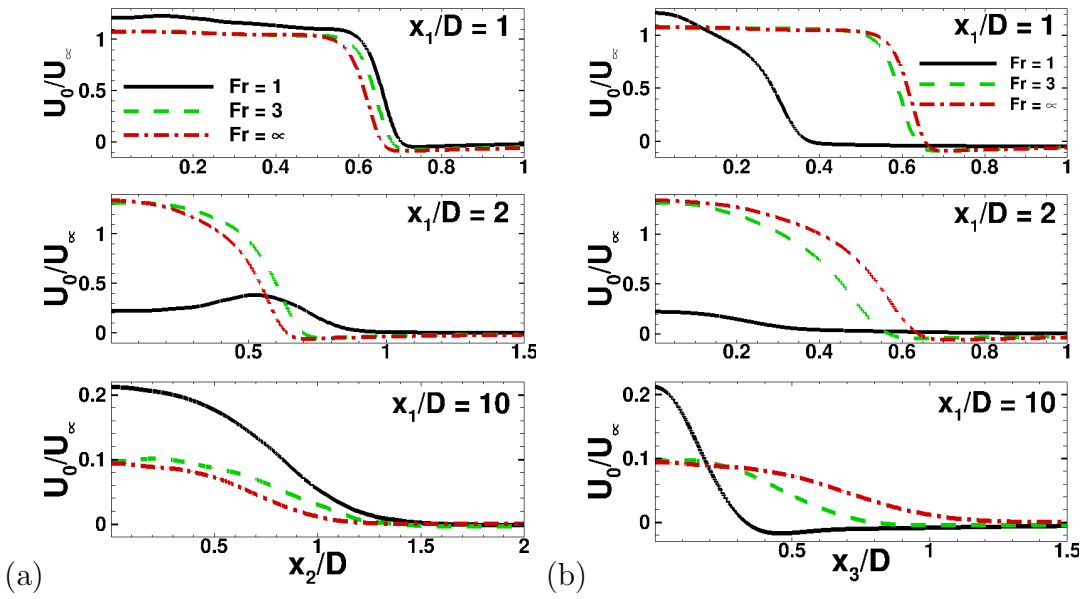

Figure 4.7: Profiles of streamwise defect velocity for the different Fr wakes at various x_1/D locations: (a) spanwise variation, and (b) vertical variation.

vertical directions are shown in figure 4.7 (a) and (b), respectively. The anisotropy between spanwise and vertical distribution of U_0 is significant in the $Fr = 1$ wake but less so in the $Fr = 3$ wake. At $x_1/D = 1$, the vertical profile of defect velocity in the $Fr = 1$ wake shows a suppression of U_0 in comparison to the unstratified case because buoyancy curves the flow towards the centerline bringing in high-momentum fluid. At $Fr = 3$, the buoyancy effect on the near wake is weaker. Notice however that although the defect velocity for $Fr = 3$ is similar in shape to $Fr = \infty$ in the near wake, the effect of buoyancy is unmistakable: the velocity profile exhibits expansion and suppression of its thickness in the horizontal and vertical directions, respectively, as compared to $Fr = \infty$. Further downstream at $x_1/D = 10$, the ordering of U_0 between the cases changes with the $Fr = 1$ wake having a higher value of U_d relative to $Fr = \infty$. The reason is that the defect velocity in the $Fr = 1$ case does not decrease relative to its value at $x_1/D = 2$ as much as the unstratified case because the $Fr = 1$ wake is already in the NEQ regime.

The balance of defect mean kinetic energy, $MKE = (\langle u_i \rangle - U_\infty)(\langle u_i \rangle -$

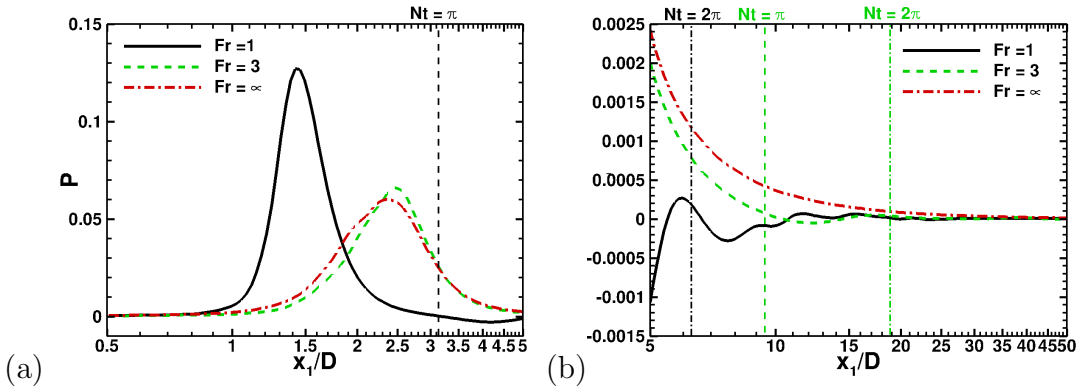

Figure 4.8: Comparison of the integrated turbulent production, P, among the different wakes: (a) $0.5 < x_1/D < 5$, and (b) $5 < x_1/D < 50$.

$U_\infty)/2$, can help better understand wake dynamics in a stratified medium. Consider the defect MKE integrated over the cross-sectional area whose evolution was shown in figure 4.5 (b). The area-integrated turbulent production, $P = -\langle u_i' u_j' \rangle \partial \langle u_i \rangle / \partial x_j$, is the primary term that is responsible for the change in defect MKE (as a function of time in the temporal model and as a function of streamwise distance in the spatial model), with the viscous dissipation of the mean flow playing a secondary role as long as turbulence is present. The entrainment into the wake brings in freestream fluid with zero defect velocity and therefore does not contribute to the balance.

Figure 4.8 shows the streamwise evolution of P integrated over the $x_2 - x_3$ cross-section. At $0.5 < x_1/D < \pi$, the integrated production term is positive for $Fr = 1$ which signifies conversion to turbulence, resulting in the streamwise decrease of area-integrated defect MKE. However, the area-integrated P is negative over $\pi < x_1/D < 2\pi$, leading to a period of increase in the mean defect velocity as observed in figure 4.5. A similar period of negative integrated P is also observed for the $Fr = 3$ wake. The integrated P for $Fr = \infty$ always remains positive, thereby leading to a monotone decay of the mean defect velocity. Integrated P is smaller in the stratified wakes and, therefore, the defect MKE is correspondingly larger in the presence of stratification.

Bonnier & Eiff (2002) measured the evolution of the centerline defect ve-

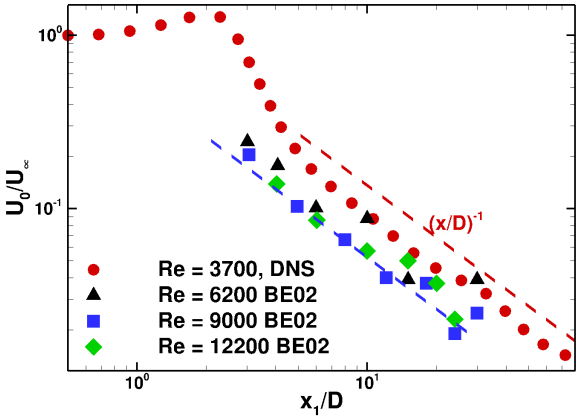

Figure 4.9: Evolution of the centerline defect velocity in the unstratified wake: comparison of present DNS result with experiments of Bonnier & Eiff (2002).

locity, U_0, in unstratified wakes and found that, for $2 < x_1/D < 30$, there is a power law of $U_0 \propto (x_1/D)^\alpha$, where $\alpha \in [-0.9, -1]$. The defect velocity in our unstratified wake simulation approximately follows a power law with $\alpha = -1$ for $5 < x_1/D < 80$ as shown in figure 4.9 (a). Chen *et al.* (1968) found the value of α to be -0.85 for $1.5 < x_1/D < 60$, whereas Uberoi & Freymuth (1970) and Bevilaqua & Lykoudis (1978) measured lower values of $\alpha \approx -0.67$ (recall that, the classical self-similarity value is $\alpha = 2/3$), in the range $50 < x_1/D < 300$ and $10 < x_1/D < 100$, respectively. The presence of the $(x_1/D)^{-1}$ scaling of the centerline defect velocity in the present unstratified axisymmetric wake may be a low-Re regime for the scaling of the dissipation (George, 1989) or could be attributed to the non-equilibrium turbulence dissipation law given by Nedić *et al.* (2013) and Dairay *et al.* (2015) that does not require low Re. According to the non-equilibrium dissipation law, ε depends on the characteristic length scale and relative velocity of the wake generator as well as the local scales for turbulent kinetic energy and wake width. Given the focus of the present paper on stratification effects and the moderate Re of the present DNS, we defer further discussion of the power law scaling to future work that includes simulations at higher Re .

To quantify the thickness of the wake for the stratified cases, half-width in the horizontal (R_2) and vertical direction (R_3) are presented in figure 4.10 (a) and (b), respectively. The half-width is defined as the radial distance to the location

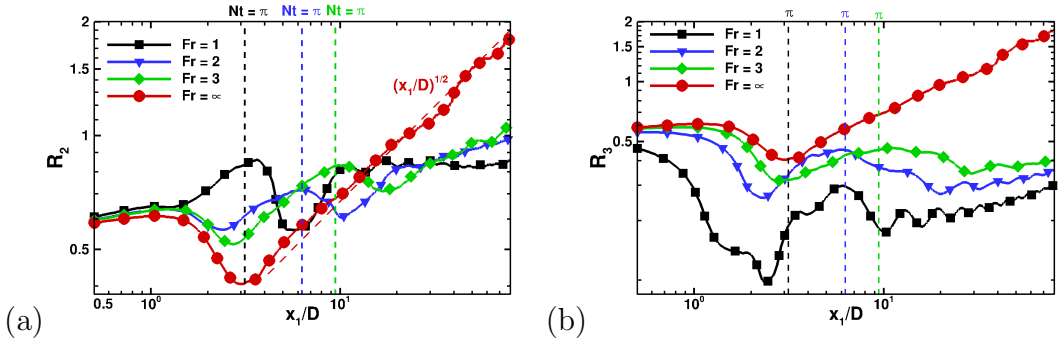

Figure 4.10: (a) Horizontal wake thickness R_2, and (b) vertical wake thickness R_3 for various Fr. Note that the vertical scale in (b) is different than in (a).

where the defect velocity reduces to half of its value at the centerline.

For the unstratified case, azimuthal averaging is performed in addition to time averaging for calculating the half-width. Near the body and in the unstratified case, the half-width of the velocity profile initially decreases in the recirculation zone and then increases as the wake profile forms and progressively thickens by turbulent entrainment. This behavior holds qualitatively for the $Fr = 2$ and 3 cases too. The unstratified axisymmetric wake thickness evolves as $(x_1/D)^{1/2}$ consistent with the $(x_1/D)^{-1}$ scaling of the centerline defect velocity. Buoyancy eventually reduces the horizontal thickness of the stratified wakes relative to the unstratified counterpart. The recirculation region progressively shortens with increasing Fr and the shortening is anisotropic. The separated boundary layer in the $Fr = 1$ case plunges inward in the vertical plane owing to buoyancy and the defect velocity at the centerline drops significantly within a short distance from the sphere. The horizontal half-width does not exhibit an initial decrease in the $Fr = 1$ wake as can also be surmised by comparing the x_2-profiles of U_0 in figure 4.7 between the $x_1/d = 1$ and $x_1/d = 2$ locations. However, comparison of the x_3 profiles between $x_1/d = 1$ and $x_1/d = 2$ suggests a decrease in R_3 for the $Fr = 1$ wake which is confirmed by figure 4.10 (b). The $Fr = 1$ wake shows a substantial decrease in R_2 between $Nt = \pi$ and 2π. This is because, as previously discussed, there is a prominent increase in centerline defect velocity, U_0, during this period owing to the lee wave while the velocity further away from the body is less affected.

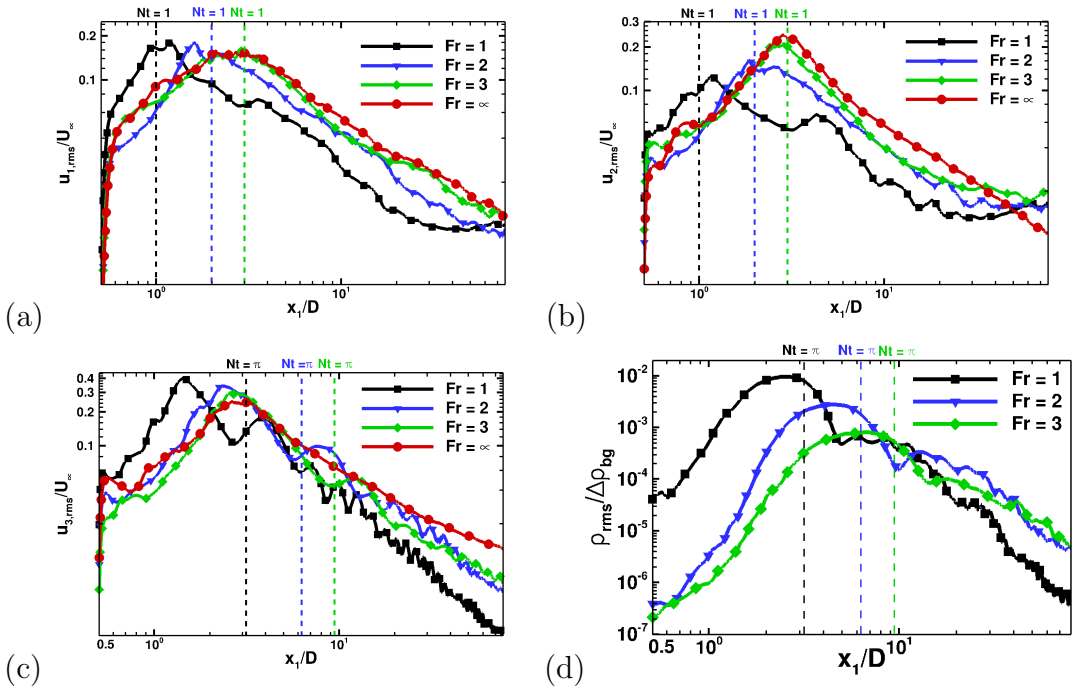

Figure 4.11: Behavior of *r.m.s.* turbulence quantities at the centerline: (*a*) streamwise velocity, (*b*) horizontal velocity, (*c*) vertical velocity, and (*d*) density deviation.

The consequent change of shape of the profile directly results in a decrease in the horizontal half-width. The $Fr = 2$ and 3 wakes also show a decrease of R_2 during this period. The vertical thickness, R_3, of the stratified wakes is generally smaller than R_2.

4.5 Turbulence levels

Buoyancy affects turbulence fluctuations differently near the body relative to locations further away. The effect is also anisotropic as can be seen from figure 4.11 that shows the streamwise evolution at the centerline of the *r.m.s.* of all velocity components, normalized with the body relative velocity U, and the density *r.m.s.*, normalized with $\Delta\rho_{bg} = D(\partial\rho/\partial z)_{bg}$. We elaborate below.

Notably, the peak value of the streamwise component, $u_{1,rms}$ (figure 4.11 a) occurs at a similar buoyancy time, $Nt \approx 1$, in all stratified cases. Also, the peak

values achieved at the stronger stratification of $Fr = 1$ and 2 are similar and are $\approx 10\%$ higher than the values at $Fr = 3$ and the non-stratified case. The inward vertical motion behind the sphere induced by the resorting force of buoyancy brings in high-momentum fluid towards the centerline, thereby increasing $u_{1,r.m.s.}$ for the $Fr = 1$ and 2 wakes. After $Nt \approx 1$, $u_{1,rms}$ decays for all the stratified cases. The value of $u_{1,rms}$ for the $Fr = 1$ case becomes lower than in the other cases for the same x_1/D location. However, the decay of $u_{1,rms}$ for $Fr = 1$ slows down at $x_1/D \sim 20$ and reaches a plateau beyond that location whereas the other cases continue decaying at a similar rate. Figure 4.11 (b) presents the evolution of the spanwise (horizontal) $r.m.s.$ velocity at the centerline for the different cases. $u_{2,rms}$ for all the stratified cases once again peaks at $Nt \approx 1$, however the peak values decrease with increasing stratification unlike $u_{1,rms}$. The maximum value of $u_{2,rms}$ for $Fr = 1$ is $\approx 50\%$, for $Fr = 2$ is $\approx 33\%$ and $Fr = 3$ is $\approx 12.5\%$ less than the peak value of $u_{2,rms}$ for the non-stratified case. The decay of centerline $u_{2,rms}$ for the stratified cases slows down after $x_1/D \sim 9$ as compared to the continuous decay in the unstratified case. By $x_1/D = 10$, there are significant differences in the streamwise $r.m.s.$ profiles among the $Fr = 1, 3$ and ∞ wakes.

The evolution of the centerline vertical $r.m.s.$ velocity (figure 4.11 c) shows that, similar to the streamwise component, the maximum value of $u_{3,rms}$ is higher in the stratified wakes: $Fr = 1$ has $\approx 38\%$, $Fr = 2$ has $\approx 29\%$ and $Fr = 3$ has $\approx 20\%$ higher values relative to the non-stratifed case. The increase in the vertical and streamwise fluctuation is due to the unsteady inward plunging of the flow in the vertical plane after separation that is induced by buoyancy. Oscillations in $u_{3,rms}$ for $Fr = 1$ and $Fr = 2$ are internal wave signatures. Notice that the frequency of oscillations is higher as the background buoyancy frequency increases. With increasing stratification, the decay of $u_{3,rms}$ becomes faster than in the unstratified case. Also, $u_{3,rms}$ becomes progressively smaller relative to the horizontal components showing the eventual dominance of horizontal motions as the stratified wake enters the regime of low local Froude number. The $r.m.s.$ of the normalized density deviation at the centerline is shown in figure 4.11 (d). It peaks shortly before $Nt = \pi$ followed by an oscillatory decay. The peak value is largest

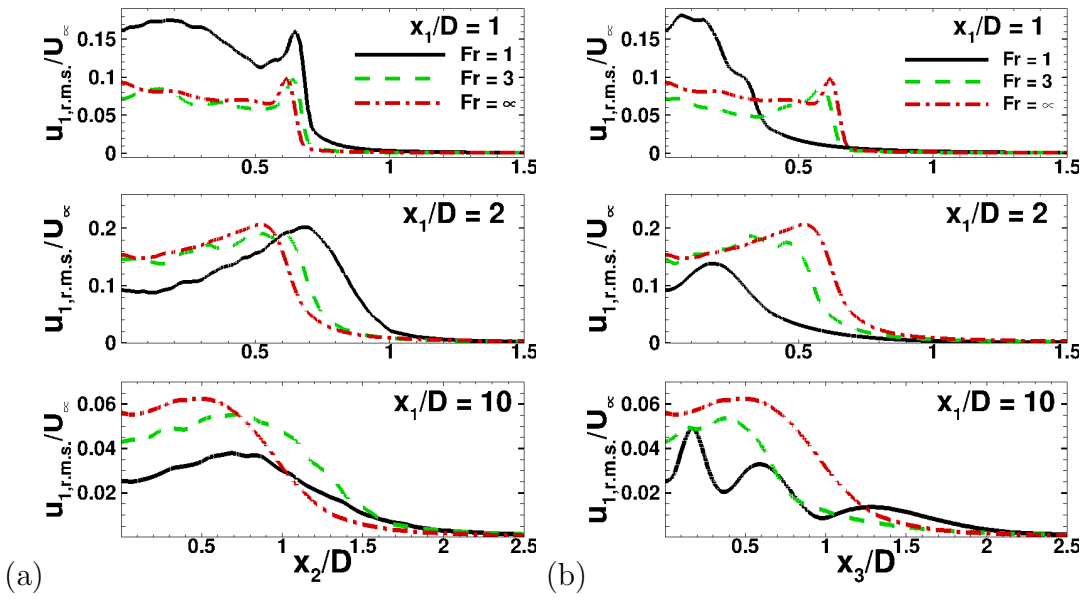

Figure 4.12: Profiles of streamwise $r.m.s.$ velocity at different x_1/D locations as a function of (a) horizontal and (b) vertical direction.

for the highest stratification of $Fr = 1$, consistent with larger vertical fluctuations in this near-body region. The subsequent decay is larger for the $Fr = 1$ wake and eventually the ordering of $\rho_{rms}/\Delta\rho_{bg}$ among the Fr cases is similar to that for $u_{3,rms}$.

The spatial variation of streamwise $r.m.s.$ velocity is compared among cases with horizontal (spanwise) and vertical profiles shown in figures 4.12 (a) and (b), respectively. Close to the body ($x_1/D = 1$), there is an outer peak corresponding to the horizontal shear layer and the $Fr = 1$ case has higher fluctuation levels. By $x_1/D = 2$, turbulence in the $Fr = 1$ wake exhibits significant anisotropy in its spatial variation (shorter in the vertical relative to the horizontal) that results in lower fluctuations at the centerline and along the vertical (x_3) coordinate. At $x_1/D = 10$, even the $Fr = 3$ wake exhibits spatial anisotropy. Oscillations in the vertical profile are noticeable for the $Fr = 1$ wake at $x_1/D = 10$ owing to internal waves.

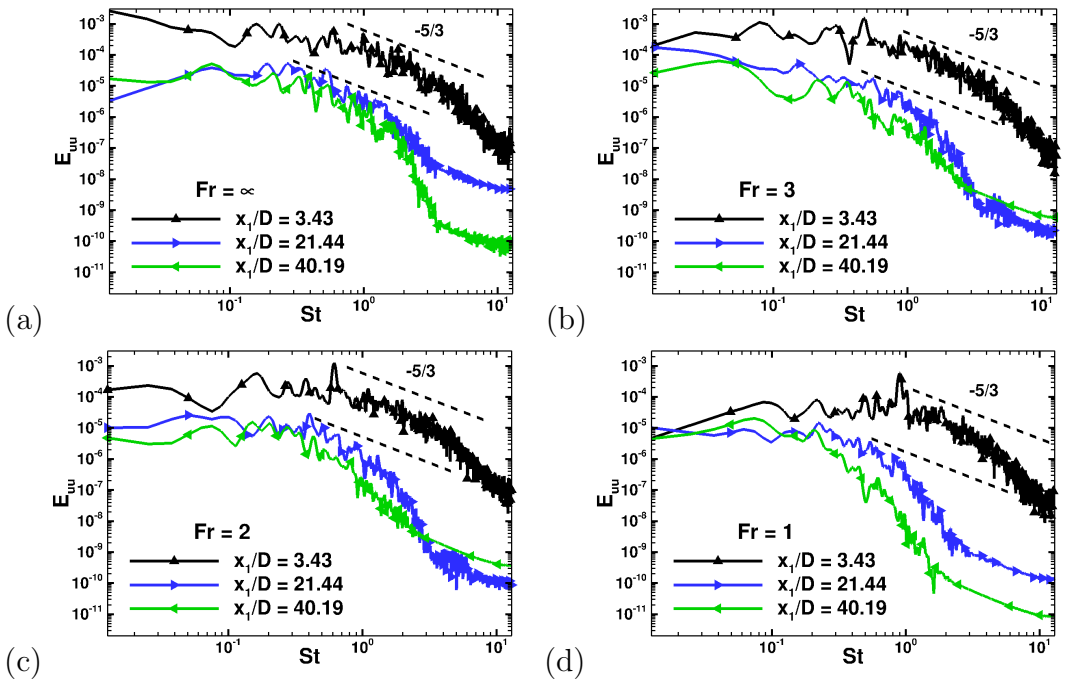

Figure 4.13: Spectra of the streamwise velocity at the centerline: (a) $Fr = \infty$, (b) $Fr = 3$, (c) $Fr = 2$, and (d) $Fr = 1$.

4.6 Spectra

Figures 4.13 (a)-(d) present the u_1-power spectra at different locations on the centerline for the cases simulated here. The $Fr = \infty$ wake has a short range of scales with a slope that is near $-5/3$ at $x_1/D = 3.43$ and 21.44. The spectrum in the $Fr = 3$ case also has a similar range of scales with an approximately inertial scaling at $x_1/D = 3.43$ but, by $x_1/D = 21.44$, it exhibits a steeper scaling. Presumably, at the moderate $Re = 3700$ of the present simulation, buoyancy is already able to alter the energy cascade at $x_1/D = 21.44$ ($Nt = 7.1$). The strong stratification in the $Fr = 1$ case eliminates any resemblance to inertial scaling in the spectra even near the body at $x_1/D = 3.43$.

Figure 4.14 shows spectra of the vertical velocity at different streamwise locations on a horizontal line ($x_2 = 0, x_3 = 0.51$) that is vertically offset by a distance of 0.51 from the centerline. The $Fr = 1$ wake (figure 4.14 a) exhibits a discrete spectral peak at $St = 0.456$ for all the shown downstream locations.

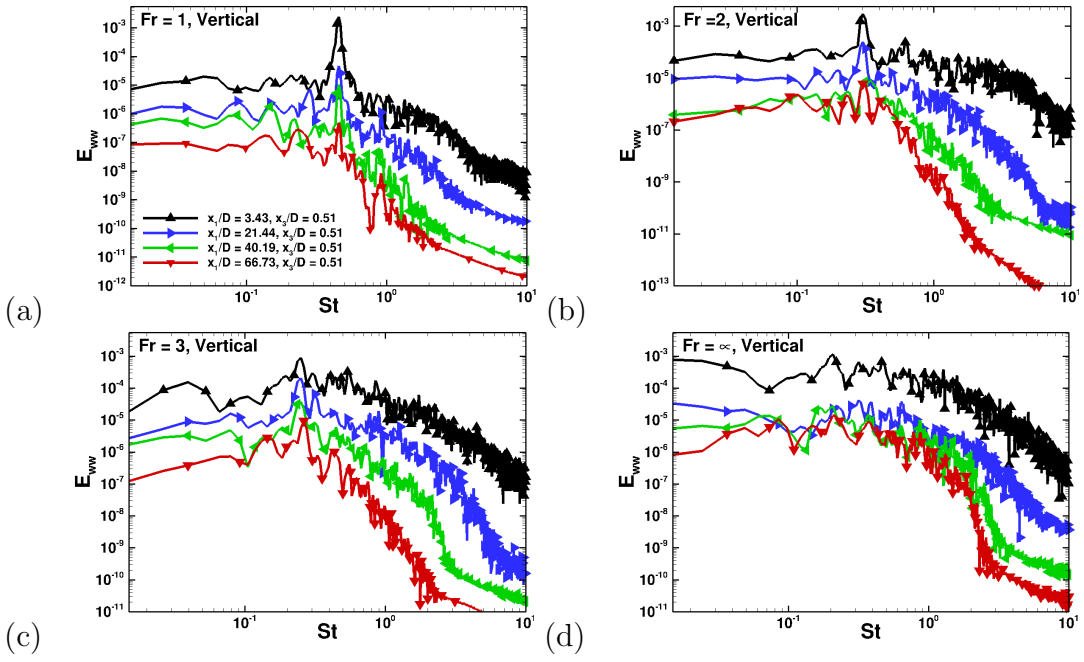

Figure 4.14: Spectra of the vertical velocity at a vertical location $x_3/D = 0.51$ and different downstream locations: (a) $Fr = 1$, (b) $Fr = 2$, (c) $Fr = 3$ and (d) $Fr = \infty$.

The $Fr = 2$ wake (figure 4.14 b) also exhibits a discrete spectral peak, whose characteristic frequency is 0.307. The spectra indicate that the $Fr = 2$ wake is more energetic across scales relative to $Fr = 1$ at the different x_1/D locations. The $Fr = 3$ wake has a characteristic frequency ($St = 0.24$) too but the peak is less prominent and the broadband spectrum is more energetic than in the lower-Fr wakes. The unstratified case shows a characteristic frequency of $St = 0.21$ near the body but it is not preserved further downstream.

4.7 Turbulent kinetic energy and its budget

The streamwise evolution of the turbulent kinetic energy TKE $= \langle u_i' u_i' \rangle / 2$, integrated over the x_2-x_3 cross-section, is shown in figure 4.15. The maximum of the integrated TKE has a similar magnitude among all cases, with the peaks approximately located at the end of the recirculation regime for each case. A significant departure of TKE for $Fr = 3$ from the $Fr = \infty$ case can be observed at

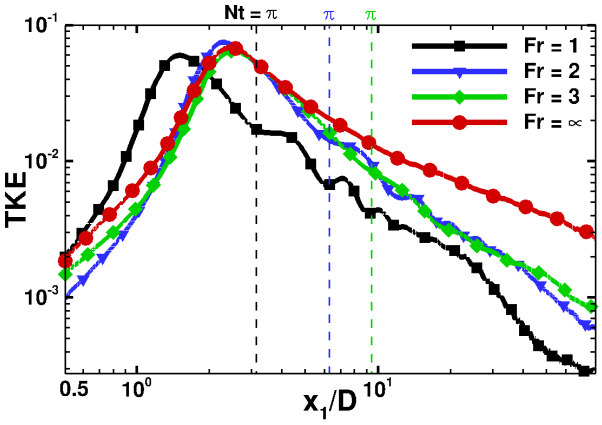

Figure 4.15: Streamwise variation of the area-integrated TKE for wakes at different Fr.

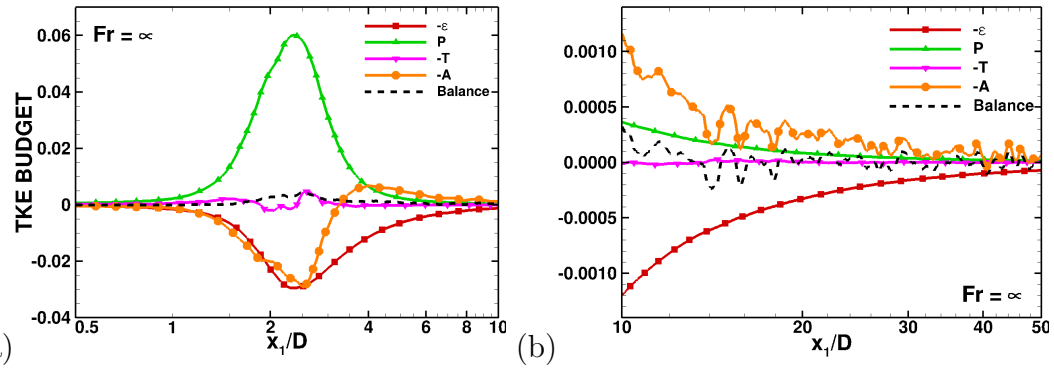

Figure 4.16: The terms in the turbulent kinetic energy budget equation for $Fr = \infty$: (a) $0.5 < x_1/D < 10$, and (b) $10 < x_1/D < 50$.

$x_1/D \approx 5$ with the point of departure moving closer to the sphere with decreasing Fr. The $Fr = 1$ and 2 wakes exhibit noticeable oscillations with a period of approximately $Nt = \pi$, related to the lee wave imprint on the wake that was discussed earlier. The TKE budget equation at statistical steady state is given by

$$0 = -A + P + B - \varepsilon - T\,, \tag{4.10}$$

where

$$A = \langle u_j \rangle \frac{\partial(\text{TKE})}{\partial x_j} \quad , \quad P = -\langle u_i^{'} u_j^{'} \rangle \frac{dU_i}{dx_j} \quad , \quad B = -\frac{g}{\rho_0} \langle \rho^{'} u_3^{'} \rangle, \tag{4.11}$$

are the advection, production, and buoyancy flux, respectively,

$$\varepsilon = 2\nu \langle s_{ij}^{'} s_{ij}^{'} \rangle, \text{ with } s_{ij}^{'} = \frac{1}{2}\left(\frac{\partial u_i^{'}}{\partial x_j} + \frac{\partial u_j^{'}}{\partial x_i}\right), \tag{4.12}$$

is the turbulent dissipation rate and $T = \partial T_i^{'}/\partial x_i$ is the transport term with

$$T_i^{'} = \frac{1}{2}\langle u_i^{'} u_j^{'} u_j^{'} \rangle + \langle u_i^{'} p^{'} \rangle / \rho_0 - 2\nu \langle u_j^{'} s_{ij}^{'} \rangle. \tag{4.13}$$

The governing equations are solved on a cylindrical grid, therefore the velocities and derivatives are transformed into the Cartesian coordinate system using equations (4.7) and (4.8), and then the terms of the TKE budget equation are computed in Cartesian coordinates.

Figures 4.16 (a)-(b) present the TKE budget integrated over a circle with radius 3 that fully contains the wake TKE region for the unstratified case. Near and aft of the sphere, the turbulent shear layer becomes unstable owing to Kelvin-Helmholtz billows which break down into turbulence. The separated shear layer interacts with the body and forms a turbulent recirculation zone. Turbulent production, P, dominates in the interval $0.5 < x_1/D < 3.5$, and is balanced by advection and dissipation. Notice that the production, advection and dissipation attain local maxima at $x_1/D \approx 2.4$, close to the end of the recirculation region. Beyond $x_1/D \approx 3.5$, dissipation becomes larger than production. Further down-

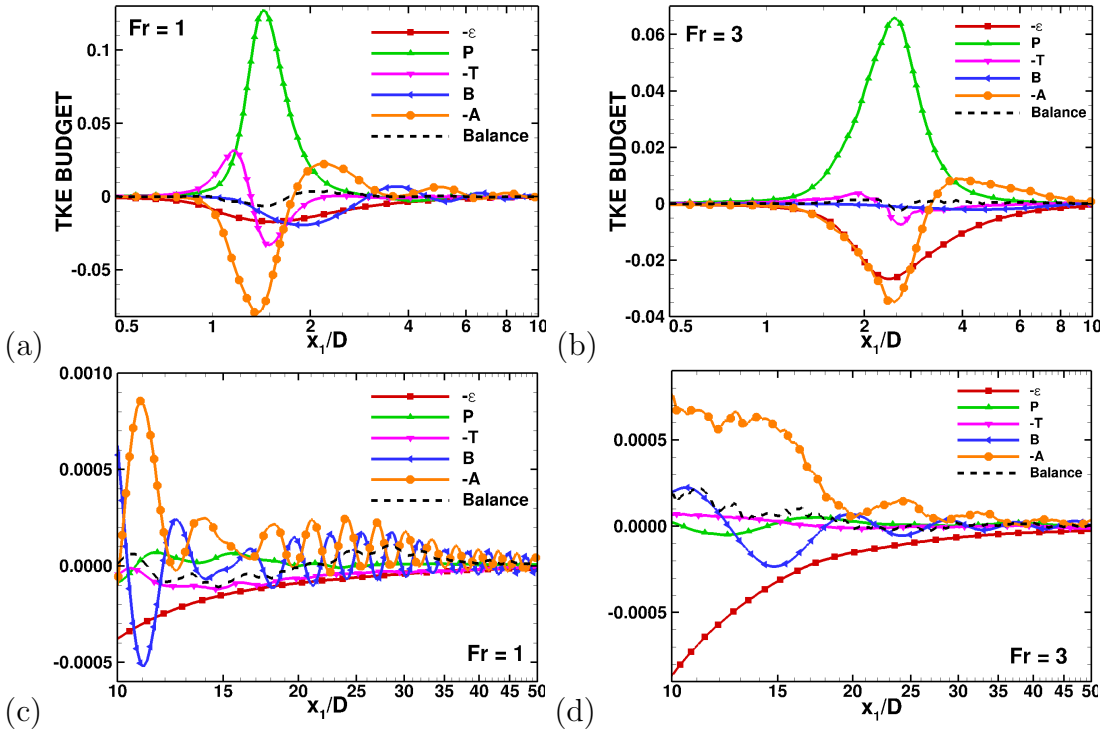

Figure 4.17: The terms in the TKE budget compared between $Fr = 1$ (left column) and $Fr = 3$ (right column).

stream (figure 4.16(b)), shear production becomes small and the balance is between advection and dissipation. The area integrated transport term remains negligible throughout the evolution.

Figure 4.17 compares the TKE budget between $Fr = 1$ and 3 over different ranges of x_1/D. The maximum value of turbulent production, P, for the $Fr = 1$ (figure 4.17 a) case is almost twice that at $Fr = 3$ (figure 4.17 b). The sharp inward curving of the shear layer (figure 4.3 a) at $Fr = 1$ brings high-momentum fluid into the region behind the sphere spanning $0 < x_1/D < 1.5$ resulting in larger P in that region. The transport term also acts as a source of TKE for $0 < x_1/D < 1.5$. Although the production is high for $Fr = 1$, the dissipation, ε, is less than that for $Fr = 3$ and ∞ case (figure 4.17(b), 4.16 (a)). A fraction of the turbulence generated by the high production for $Fr = 1$ is carried away by internal waves, as evidenced by the negative value of the transport term (dominated by pressure transport) and the rest is dissipated via viscosity. Internal waves play a vital role

in the balance as suggested by the importance of the integrated transport term. For $Fr = 3$, the waves are weak for the moderate-Re wake simulated here, and the transport term is much smaller than at$Fr = 1$. Therefore, most of the fluctuation energy is dissipated locally by viscosity in $Fr = 3$ wake.

The advective term remains positive until $x_1/D \approx 2$ for $Fr = 1$ as compared to $x_1/D \approx 3.5$ for the $Fr = 3$ and ∞ cases. We also find reversible transfer between turbulent kinetic and potential energy modes as the buoyancy flux switches signs for $Fr = 1$, whereas this transfer for $Fr = 3$ within $0.5 < x_1/D < 10$ is small. After $x_1/D \approx 2$, the combination of the dissipation and the buoyancy flux dominates the production term and the advective term acts as a gain. The behavior of the TKE budget terms for $Fr = 3$ (figure 4.17 (b)) is similar to the unstratified case within $0.5 < x_1/D < 10$. The stronger effect of buoyancy for $Fr = 1$ is evident from the dominance of local buoyancy flux within the range $10 < x_1/D < 50$ (figure 4.17(c)), with advection being of the same order. The production, dissipation and the transport terms have comparable values. The transport of TKE away from the wake, owing to the propagation of internal waves, is also evident by the negative value of the transport. The $Fr = 3$ case (figure 4.17(d)) has comparable dissipation, advection and buoyancy flux terms with lower values of the production and transport terms.

4.8 Summary and conclusions

DNS of flow past a sphere at $Re = 3700$ has been performed in the regime of moderate stratification ($Fr = U/ND = O(1)$) for cases with $Fr = 1, 2, 3$ as well as an unstratified case with $Fr = \infty$. The Navier-Stokes equations are solved on a cylindrical coordinate system and the sphere is represented using an immersed boundary method. The numerical model has been validated against previous laboratory and DNS results of unstratified flow past a sphere. The evolution of the unstratified case is simulated into the far wake up to $x_1/D = 80$ as are the stratified cases. A detailed discussion of the separated flow, the near wake and the transition from the near to the nonequilibrium (NEQ) region is provided. The

TKE, its budget and turbulence profiles are contrasted between the unstratified and stratified cases to quantify buoyancy effects on the fluctuations.

The centerline mean defect velocity, U_0, of the unstratified wake decays after the recirculation zone as $U_0 \propto x_1^{-1}$, different from the classical, self-similar scaling of $x_1^{-2/3}$, and in agreement with the measurements of the sphere wake by Bonnier & Eiff (2002) and other axisymmetric wakes by Nedić *et al.* (2013) and Dairay *et al.* (2015). The recirculation zone shortens with increasing buoyancy owing to the plunging of the separated flow in the vertical plane brought about by the restoring force of buoyancy which tends to return displaced fluid back towards its neutral position. The recirculation region is followed by a decrease of U_0 with a rate that is similar to that in the unstratified case until $Nt = \pi$ after which U_0 increases with increasing x_1/D. The period of increasing U_0 ends at $Nt \approx 2\pi$, beyond which the wake enters into the NEQ regime. Bonnier & Eiff (2002) identified a phase of wake collapse with accelerated U_0. We find that the increase of U_0 is actually the initial half-cycle of an decaying oscillatory modulation of U_0 with period $Nt = 2\pi$ that is the imprint of a steady lee wave pattern. The lee wave leads to a periodic pattern of vertical flow convergence and divergence at the centerline, thus modulating the thickness and streamwise velocity of the central wake region.

In the NEQ regime of stratified wakes, the decay of U_0 slows down significantly with $U_0 \propto (x_1/D)^{-0.25}$ for all the simulated stratified cases. Thus, the $(x_1/D)^{-0.25}$ scaling seen by Spedding (1997) for $Fr > 5$ wakes is applicable to lower stratifications down to $Fr = 1$. During the NEQ regime, the stratified wakes have a mean deficit that becomes progressively larger relative to their unstratified counterpart and, by $x/d = 80$, the $Fr = 3$ wake has an order of magnitude larger U_0 and defect MKE. The stratified wake is long lived because buoyancy reduces the loss to turbulence, i.e. turbulent production, P, is severely reduced, e.g. P crosses zero at $Nt = 2\pi$. Furthermore, the flow organizes into coherent horizontal motions.

Buoyancy changes TKE levels and introduces significant anisotropy in the fluctuations, both among vertical and horizontal velocity components and in their spatial organization. Therefore, the choice of initial fluctuation profiles for a tem-

poral model will present a challenge for wakes with stratification levels equal to or greater than those examined here. Near the body, TKE is larger at $Fr = 1$ but, by $Nt = 2$, becomes significantly smaller than at $Fr = \infty$. The vertical component decays faster than the horizontal components and has a discrete peak in its spectrum near the body that remains prominent at downstream locations. The spatial profiles of the $r.m.s.$ turbulence are substantially different relative to the unstratified case, e.g., at $x_1/D = 10$, the horizontal width of the streamwise $r.m.s.$ profile in the $Fr = 3$ wake is larger while the vertical width is smaller than in the $Fr = \infty$ wake.

The TKE budget terms, integrated over an area that encloses the wake, show a good balance for all cases owing to the high resolution that is employed. In the unstratified wake, production is the dominant term until $x_1/D = 3$, and is balanced by dissipation and advection. Further downstream, production becomes increasingly less important (by $x_1/D \approx 10$, production is one third of the dissipation) and the balance shifts to one between advection and dissipation. The dominance of advection over production as the source of TKE is an important distinction between wakes and other shear flows which contributes to the long memory of near-body turbulence in the wake. Buoyancy and transport, through the pressure-velocity correlation, contribute to the balance in the stratified flows, from near the body at $Fr = 1$ and from $x_1/D \approx 9$ ($Nt \approx 3$) at $Fr = 3$. The $Fr = 1$ case has a prominent internal wave signature in visualizations and, correspondingly, the pressure transport is also important displaying an oscillatory behavior near the body and then, further downstream, acting as a consistent sink of TKE.

Internal waves are an important constituent of fluctuating motion in stratified flows past bodies. Quantification of the properties of internal waves and their variation as a function of Fr is the subject of ongoing work. The present results have been obtained at a moderate Re and moderate Fr. Simulations at higher Re will be necessary to ascertain the robustness of the present conclusions to increased Re and, with higher Fr simulations, this work can be extended to low-stratification wakes.

4.9 Acknowledgements

The contents of this chapter has been submitted to the Journal of Fluid Mechanics (2016), coauthored by Professor Sutanu Sarkar, Dr. Antonio Posa and Professor Elias Balaras. A. Pal, S. Sarkar, A. Posa & E. Balaras, DNS of stratified flow past a sphere at a Reynolds number of 3700., *J. Fluid Mech.* (submitted) (2016). The thesis author was the primary author of this paper.

Chapter 5

Regeneration of turbulent fluctuations in low-Froude-number flow over a sphere at Reynolds number of 3700.

Recent numerical and experimental studies of the benchmark problem of flow past a sphere in a uniformly stratified fluid mostly consider $Fr \geq O(1)$ where $Fr = U/ND$ is based on body velocity U, body diameter D, and buoyancy frequency N. Strong stratification, e.g. the upper ocean pycnocline, can lead to $Fr \leq O(1)$ considered here. Unlike previous low-Fr studies of flow past a sphere, the present Reynolds number of $Re = UD/\nu = 3,700$ is not small.

The first numerical simulations of the low-Fr case over a sphere (Hanazaki, 1988) were at $Re = 200$ (laminar flow). It was found that the flow tends to flow around in the horizontal rather than going over the sphere if $Fr < 0.5$ and eventually approaches two dimensionality for $Fr < 0.2$. Later experiments (Lin *et al.*, 1992*b*; Chomaz *et al.*, 1993a) covered a wide range of Fr and Re, but the low

Fr cases had low Re as well. The near wake was classified in four regimes (Chomaz *et al.*, 1993a) depending on Froude number, including the quasi 2-D regime that occurred for the lowest examined values of $Fr \in \{0.125, 0.4\}$. A recent DNS (Orr *et al.*, 2015) included $Fr < 1$ cases but at low $Re = 200$. None of these prior studies report turbulence in the low Fr regime. It has been suggested (Chomaz *et al.*, 1993a) that the effect of Re is weak when $Fr < 0.35$ as long as Re exceeds 100. On the other hand, quasi-2D motion in strongly stratified flow can be turbulent when the Reynolds number is large as found for Taylor-Green vortices (Riley & deBruynKops, 2003), homogeneous turbulence (Lindborg, 2006; Brethouwer *et al.*, 2007) and a far wake (Diamessis *et al.*, 2011). The nonequilibrium region of the far wake is also lengthened for large Re (Brucker & Sarkar, 2010).

5.1 Problem formulation, numerical details and validation

Motivated by the unanswered question regarding near-wake turbulence when Fr is low but Re is not, we use DNS to investigate the flow past a sphere at $Re = 3,700$ and $Fr \in \{0.025, 1\}$. The three-dimensional Navier Stokes equations are solved on a cylindrical coordinate system on a staggered grid using an immersed boundary method (IBM) (Balaras, 2004; Yang & Balaras, 2006) for representing the sphere.

The simulation parameters, domain size and grid distribution for the different cases are given in table 6.1. High resolution is used at the sphere surface (20 points across the boundary layer thickness at the point of maximum wall shear stress) and in the wake. The radial grid spacing is $\Delta r \simeq 0.0016$ in the cylindrical region ($r < 0.65$) that encloses the sphere, the azimuthal direction has 128 points, and $\Delta x \simeq 0.0016$ near the surface. The grid has mild stretching, radially and streamwise, away from the body. The IBM results and the grid resolution to resolve the flow have been successfully validated in the unstratified case against

Table 5.1: Simulation parameters. The sphere is located at $(0, 0, 0)$. The substantial domain size in the radial and upstream direction, along with the sponge region, eliminates the spurious reflection of internal waves. $L_\theta = 2\pi$ and $N_\theta = 128$.

Case	*Re*	*Fr*	L_r	L_z	N_r	N_z
1.	3700	0.025	58	63 (40 upstream; 23 downstream)	690	3072
2.	3700	0.05	58	63 (40 upstream; 23 downstream)	690	3072
3.	3700	0.125	58	120 (40 upstream; 80 downstream)	690	4608
4.	3700	0.17	58	56 (40 upstream; 16 downstream)	690	2560
5.	3700	0.21	58	56 (40 upstream; 16 downstream)	690	2560
6.	3700	0.25	58	120 (40 upstream; 80 downstream)	690	4608
7.	3700	0.5	58	120 (40 upstream; 80 downstream)	690	4608
8.	3700	0.8	58	120 (40 upstream; 80 downstream)	690	4608
9.	3700	1	58	103 (25 upstream; 80 downstream)	690	4608
10.	3700	∞	16	95 (13 upstream; 80 downstream)	630	4608

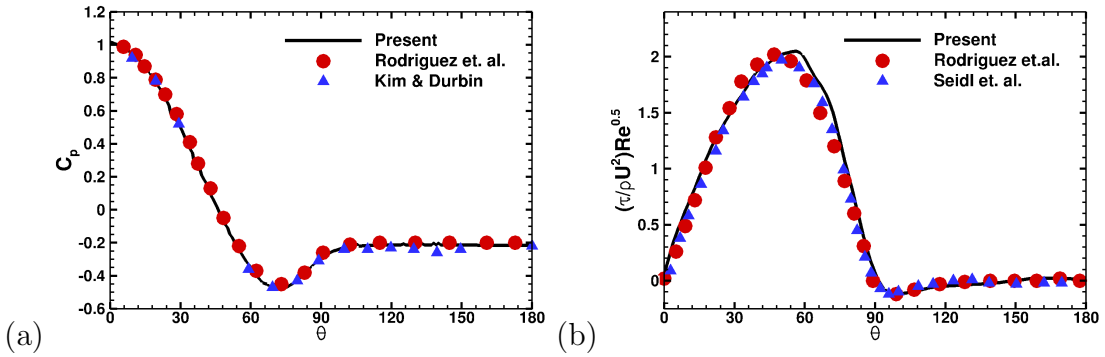

Figure 5.1: Validation of unstratified wake: (a) Pressure coefficient, C_p, (b) Normalized drag coefficient, $(\tau/\rho U^2)Re^{0.5}$. Here, θ is the azimuthal angle with $\theta = 0$ corresponding to the forward stagnation point.

both previous simulations and laboratory experiments. Figures 5.1 (a)-(b) show that the variation of the surface pressure coefficient, C_p, and the surface shear stress $(\tau/\rho U^2)Re^{0.5}$, as a function of azimuthal angle, matches well with results in the available literature. Table 5.2 shows that key characteristics of the near-body flow such as Strouhal number $(St = fD/U)$, the azimuthal separation angle (φ_s), coefficient of drag (C_d) and pressure coefficient (C_{pb}) at the rearward stagnation point also match with previously reported values.

Table 5.2: Comparison of the different statistical flow features of the near-body flow in the present DNS with experimental measurements and numerical results available in the literature.

Case	*Re*	*St*	$\varphi_s(^\circ)$	$\overline{C_d}$	$\overline{C_{pb}}$
Present DNS (unstratified case)	3700	0.210	91.7	0.3938	-0.219
Schlichting (1979)(exp.)	3700			0.39	
Kim & Durbin (1988)(exp.)	3700	0.225			-0.224
Sakamoto & Haniu (1990)(exp.)	3700	0.204			
Seidl *et al.* (1997)(DNS)	5000		89.5	0.38	
Tomboulides & Orszag (2000)(DNS)	1000	0.195	102		
Constantinescu & Squires (2003)(LES)	10^4	0.195	85-86	0.393	
Yun *et al.* (2006)(LES)	3700	0.21	90	0.355	-0.194
Rodriguez *et al.* (2011)(DNS)	3700	0.215	89.4	0.394	-0.207

5.2 Results and discussion

Figure 5.2 shows the downstream evolution of turbulent kinetic energy (TKE) integrated over cross-stream (x_2-x_3) planes for cases with different Fr. Note that x_3 denotes the vertical coordinate, the horizontal directions are x_1 (streamwise) and x_2 (lateral), and the sphere center is at the origin. All statistics are computed after the initial transient by time averaging over an interval of 1.5 L_x/U which is sufficient to obtain converged statistics. Buoyancy in a stratified wake is found to suppress turbulence in previous studies and, accordingly, TKE decreases when Fr decreases from 1 to 0.8 to 0.5. However, the trend reverses when Fr decreases to 0.25 and beyond: TKE *increases* with *decreasing* Fr. The value of TKE in the $Fr = 0.25$ case increases to a level comparable to the $Fr = 0.8$ case and a further decrease of Fr to 0.21 lead to values of TKE larger than in the unstratified case. Subsequent reduction in Fr beyond 0.21 leads to progressive augmentation of TKE.

To understand the remarkable regeneration of fluctuations in the near wake at low Fr, contour plots of azimuthal vorticity magnitude in the horizontal (x_1-x_2) and vertical ($x_1 - x_3$) planes (figure 5.3) are examined. The near-wake dynamics changes *qualitatively* for cases with $Fr \leq 0.25$, as elaborated below. The $Fr = 1$

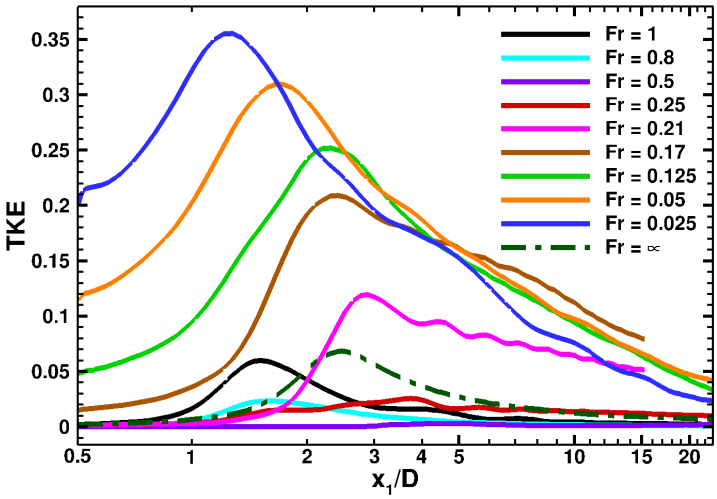

Figure 5.2: Evolution of integrated turbulent kinetic energy in streamwise direction.

wake displays the anisotropy of a moderate-Fr wake: a large spread in the horizontal plane (figure 5.3a) and small scale structures associated with the shear layer instability while, in the vertical plane, the separated boundary layers (figure 5.3b) contract, followed by an undulation of the wake. At $Fr = 0.5$ (not shown here), the recirculation bubble is steady, the disintegration of the shear layer is suppressed in the horizontal plane, and the separating shear layers dip to the centerline in the vertical plane. The shear layer formed by the separating boundary layer exhibits large steady waviness in the vertical plane, there is little unsteadiness in the near wake and, therefore, the TKE for $Fr = 0.5$ is insignificant as was shown in figure 5.3. A quasi-steady recirculation bubble attached to the sphere is found in the horizontal plane (figure 5.3c) for a larger stratification, $Fr = 0.25$. At the end of the recirculation zone, the wake undergoes an unsteady undulation with the shedding of vortices further downstream. The shear layer in the vertical direction (figure 5.3d) manifests waviness (induced by lee waves), but the instability does not break down into turbulence. The flow between the upper and lower shear layers displays thin strips of enhanced vorticity symptomatic of vorticity layering.

The flow organization changes significantly with further decrease in Fr to 0.125 and beyond. There is unsteady motion of the shear layers in the horizontal

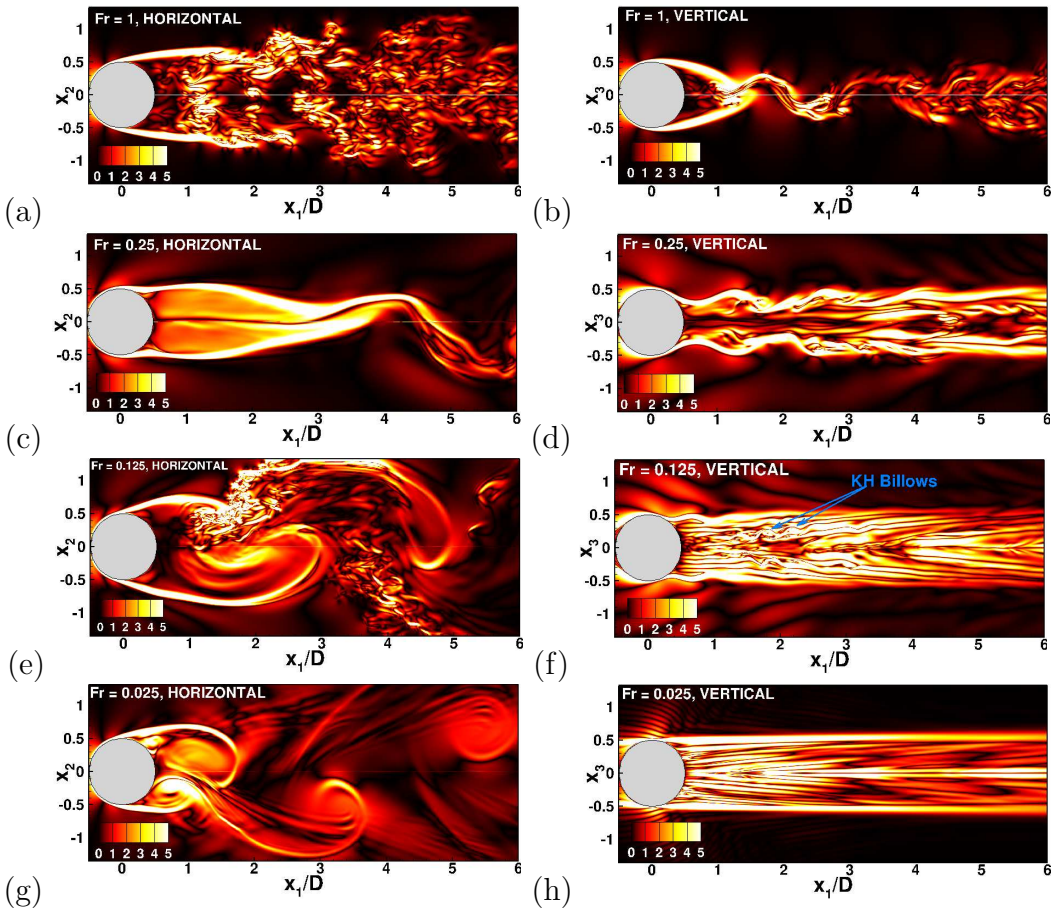

Figure 5.3: Instantaneous azimuthal vorticity magnitude on the horizontal $x_1 - x_2$ plane ($x_3 = 0$) and the vertical $x_1 - x_3$ plane ($x_2 = 0$). Snapshots compared among cases with different Fr.

plane accompanied by patches of small-scale turbulence (figure 5.3e) as compared to the steady recirculation bubble in the $Fr = 0.25$ wake. This reappearance of small scale fluctuations at $Fr = 0.125$ occurs due to unsteady vortex shedding in the horizontal plane, which results in both flapping and destabilization of the shear layer. A similar vertical layering of vorticity as $Fr = 0.25$ is also seen at $Fr = 0.125$ but, in this case, the layers roll up intermittently to form Kelvin-Helmholtz (KH) billows (figure 5.3f) which then break down into finer-scale fluctuations. A secondary instability of pancake vortices in the far wake to form KH rolls was noted in previous temporal simulations (Diamessis *et al.*, 2011) for sufficiently high Re. In the present near wake, the perturbations provided by the horizontal flapping motion and the value of the local Re are sufficient to destabilize the vertically layered vorticity into KH billows. As Fr approaches 0.025, the unsteady vortex shedding from the sphere in the horizontal plane becomes more noticeable. The TKE in the region $x/D < 1$ that belongs to the very near wake is also the largest among all simulated cases as shown in figure 5.2. In the horizontal plane (figure 5.3g), there are coherent vortices with interspersed threads of rolled-up vorticity. In the vertical plane(figure 5.3h), layered vortical structures are seen but do not manifest KH billows. The fact that KH billows are absent in the $Fr = 0.025$ case will be explained, based on the value of buoyancy Reynolds number and the scaling analysis of Riley & deBruynKops (2003) and Brethouwer *et al.* (2007), later in the paper. The vorticity pattern at $Fr = 0.025$ appears to have less fine-scale activity relative to $Fr = 0.125$. Internal gravity waves at the body can be seen in the vertical plane (figure 5.3d, f, h) but their discussion is deferred to future work.

Both mean and turbulent kinetic energy are increasingly dominated by horizontal motions as Fr decreases to 0.25 and below. The evolution of the ratio of area-integrated mean kinetic energy of the horizontal component ($MKE_{11} + MKE_{22}$) and vertical component (MKE_{33}) is shown in figure 5.4(a). For $Fr = 1$, horizontal MKE is larger near the sphere but, beyond $x_1/D \approx 5$, MKE becomes similarly distributed among the horizontal and vertical components. The undulations after $x_1/D \approx 5$ signify the exchange of MKE between horizontal and

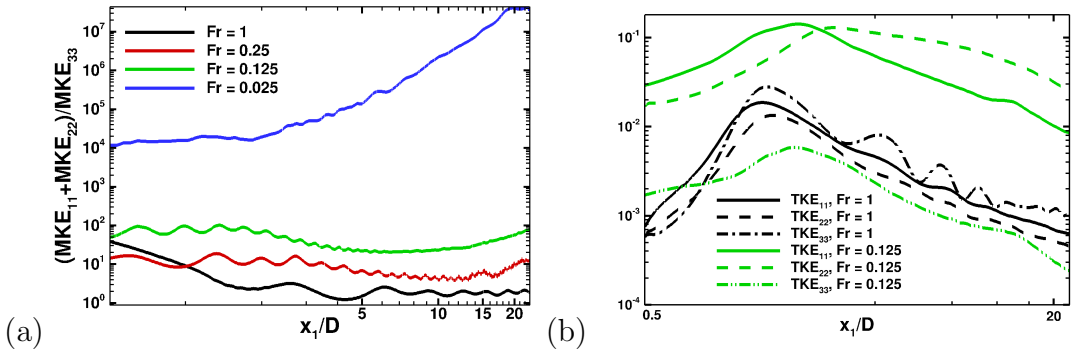

Figure 5.4: Evolution of (a) the ratio of area-integrated horizontal and vertical mean kinetic energy, (b) components of integrated turbulent kinetic energy, in streamwise direction. The area integration is over the x_2, x_3 plane normal to the streamwise direction.

vertical components. The ratio $(MKE_{11} + MKE_{22})/MKE_{33}$ for $Fr = 0.25$ and 0.125 characterizes the transition of the near wake into quasi-horizontal motion. The case with $Fr = 0.025$ exhibits the complete dominance of horizontal motion wake unsteadiness, present primarily in the form of layered coherent vortices that span a wide lateral (x_2) extent. The streamwise variation of the components of TKE for $Fr = 1$ and 0.125 is presented in figure 5.4(b). The components of TKE for $Fr = 1$ evolve in a similar manner, whereas for $Fr = 0.25$ (not shown here) the streamwise (TKE_{11}) and spanwise (TKE_{22}) components are larger relative to the vertical (TKE_{33}) component. A significant difference between the horizontal (TKE_{11}, TKE_{22}) and vertical components is observed as Fr is further decreased to 0.125 (shown here) and 0.025 (not shown here).

Temporal spectra are examined to quantify buoyancy effects on the frequency content of lateral velocity, v. Figure 5.5(a) shows that there is a significant decrease of energy at all frequencies when stratification increases to change Fr from 1 to 0.25. However, a further decrease of Fr to 0.125 and 0.025 shows a re-energization of fluctuations at all frequencies. There is a strong low-frequency peak in these cases: (i) $St = \omega D/U = 0.163$ for $Fr = 0.125$, (ii) $St = 0.200$ for $Fr = 0.025$. Secondary peaks of E_{vv} at harmonics of the low-frequency mode are also evident. There is substantial energy, much larger than at $Fr = 0.25$, at the

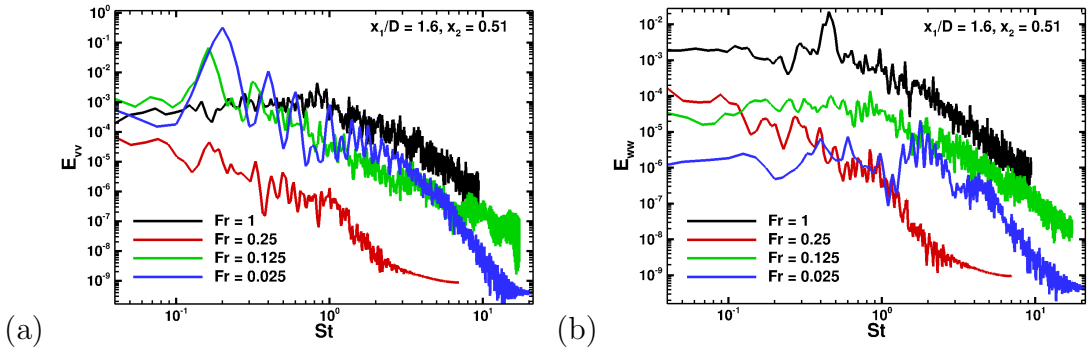

Figure 5.5: Energy spectra of (a) lateral v and (b) vertical w fluctuations at a downstream point ($x_1 = 1.6, x_2 = 0.51, x_3 = 0$) in horizontal center plane at various Froude numbers. E_{vv}, E_{ww} and Strouhal number, St are nondimensional values based on U and D.

intermediate frequencies as well. Notice that for flow over a circular cylinder in an unstratified environment at $Re = 3900$, the shedding frequency is found to be ≈ 0.2 (Parnaudeau *et al.*, 2008). Therefore, with increasing stratification, the vortex shedding of a sphere shifts towards that of a circular cylinder. This is because the flow at depths larger than $O(U/N)$ with respect to the top of the sphere tends to divert around the sphere rather than over the sphere because of the potential energy barrier. We emphasize that the low-Fr near wake, apart from the similarity of vortex shedding, is quite different from the unstratified cylinder wake where the strong inhibition of vertical fluctuations by buoyancy is absent. For example, the vertical velocity spectra E_{ww} (figure 5.5(b)) at $Fr = 0.125$ and $Fr = 0.025$ have much smaller amplitude relative to their corresponding horizontal counterpart, E_{vv}, and also have smaller amplitude with respect to E_{ww} for the $Fr = 1$ case.

The mean velocity profiles change significantly with decreasing Fr because of the preferential flow around the sphere rather than over it. Thus, the profile of the mean streamwise velocity (figure 5.6 a) along the lateral line ($x_1 = x_3 = 0, x_2 > 0.5$) shows enhanced horizontal shear in the vicinity of the sphere boundary at $x_2 = 0.5$, for the lower-Fr cases in comparison to $Fr = 1$. At $x_1 = 1$ (figure 5.6 b), the shear is confined within a narrow band of $0.5 < x_2 < 0.8$ for $Fr = 1$, whereas $Fr = 0.25, 0.125, 0.025$ show progressively broader regions of shear. The

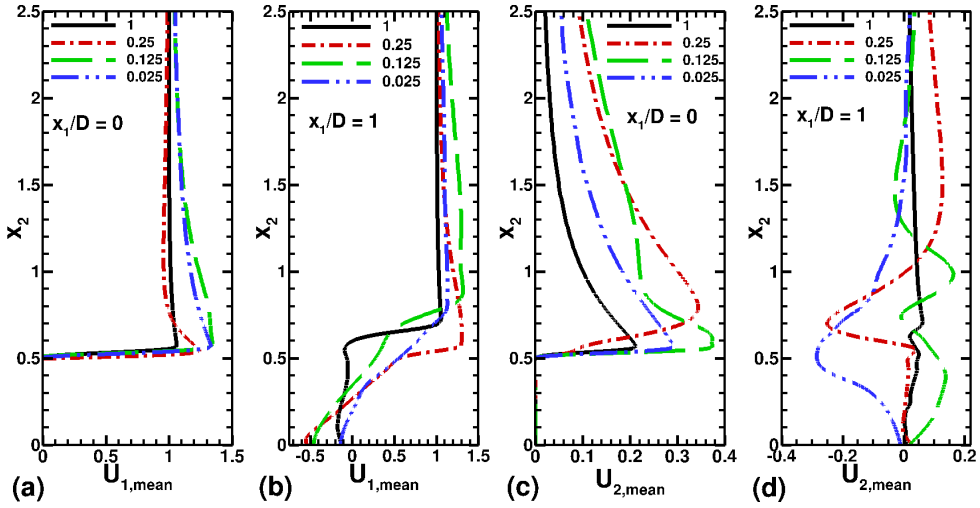

Figure 5.6: Streamwise ($U_{1,mean}$) and lateral ($U_{2,mean}$) mean velocity profiles are plotted as a function of lateral coordinate x_2 at two streamwise locations ($x_1/D = 0, 1$) in the horizontal central plane, $x_3 = 0$.

lateral, horizontal motion of the fluid near the sphere is also enhanced as shown by the the profile of the lateral velocity $U_{2,mean}(x_2)$ on the line ($x_1 = x_3 = 0, x_2 > 0.5$) as shown by figure 5.6 (c). At $x_1 = 1$, the variation of $U_{2,mean}$ as a function of x_2 (figure 5.6 d) is substantial for $Fr = 0.25, 0.125, 0.025$ and has a complex shape because of the three-dimensional mean flow near the body.

The production of TKE is given by $P = -\overline{u_i' u_j'} \partial \bar{U}_i / \partial x_j$ with the overbar denoting mean value. The various components, $P_{\alpha,\beta}$ that comprise P change in the near wake ($x/D < 5$) because of the buoyancy effect. Figure 5.7 shows the downstream evolution of the components, $P_{\alpha,\beta}$, integrated over the cross-stream $x_2 - x_3$ plane. The integrated production for the $Fr = 1$ wake is primarily dominated by the components (P_{13}, P_{31}) involving vertical fluctuations u_3' with some contributions from the components (P_{12}, P_{22}) involving horizontal fluctuations u_2' as shown in figure 5.7 (a). This scenario changes when stratification increases. As illustrated in figure 5.7 (b) for $Fr = 0.25$, the components P_{13} and especially P_{31} are suppressed with respect to $Fr = 1$ and by $Fr = 0.025$ (figure 5.7 d), both become negligible as the buoyancy effect strengthens to make u_3' negligible. However, P_{12} and P_{22} associated with horizontal fluctuations *increase* when Fr is reduced

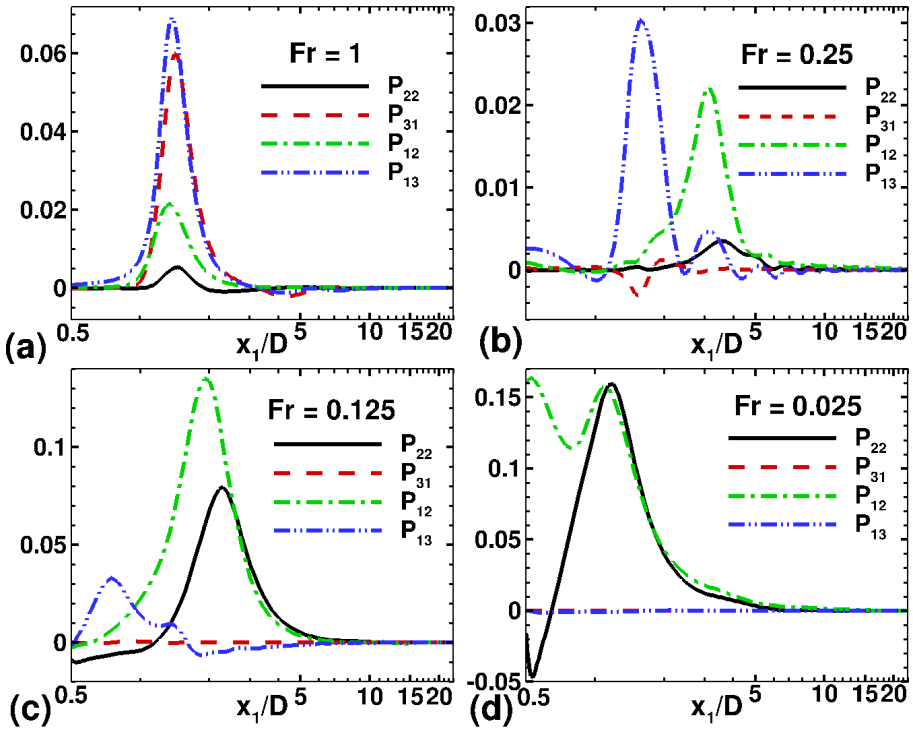

Figure 5.7: Shear production components for different Fr cases, integrated over $x_2 - x_3$ planes.

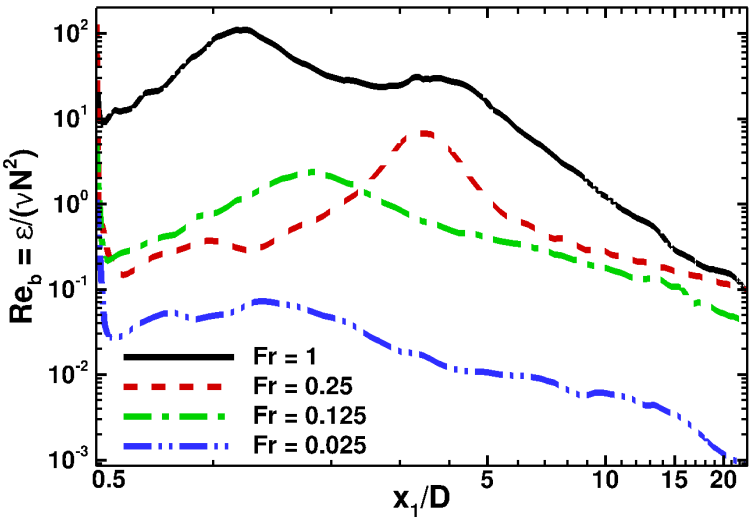

Figure 5.8: Variation of buoyancy Reynolds number $Re_b = \varepsilon/(\nu N^2)$ for different Fr at the center line $x_2 = 0, x_3 = 0$ in the streamwise direction x_1.

to 0.125 from 0.25. The large lateral (x_2) gradients of mean U_1 (figure 5.6 b) and mean U_2 (figure 5.6 d) enhance P_{12} and P_{22}, respectively, making them the leading production terms for $Fr = 0.125$ and 0.025.

The buoyancy Reynolds number, $Re_b = \varepsilon/\nu N^2$, where ε is the turbulent dissipation rate and N is the background buoyancy frequency, is an often-used parameter to distinguish the turbulent nature of fluctuations in stratified flow. A similar parameter that distinguishes turbulence is $\mathcal{R} = ReFr_h^2$, where $Fr_h = u/l_h N$ (l_h is the length scale and u is the velocity scale of horizontal fluctuations) is the horizontal Froude number, and $Re = ul_h/\nu$. The choice of $l_h = u^3/\varepsilon$ makes $\mathcal{R}$ identical to Re_b. Riley & deBruynKops (2003) estimated the Richardson number of layered motions in strongly stratified flow by $Ri \simeq 1/\mathcal{R}$, and proposed that layer instability was possible if $Ri \lesssim 1$ or, equivalently, $\mathcal{R} \gtrsim 1$. Brethouwer *et al.* (2007) concluded that if $\mathcal{R} >> 1$ an energy cascade from large to small scales is possible allowing an inertial range in horizontal energy spectra. In contrast for $\mathcal{R} << 1$, the dissipation ε is associated with quasi-two-dimensional scales. Arobone & Sarkar (2010), in their DNS of a stratified fluid with horizontal shear found a network of quasi-2D vortices with interspersed dislocations that were laminar for small Re_b

but exhibited secondary instability for larger Re_b.

We find that the values of Re_b (figure 5.8) provide guidance to the observed differences in the state of fluctuating motion at different Fr. The $Fr = 1$ case has Re_b values between $10 - 100$ at $0.54 < x_1/D < 5.5$, signifying broadband turbulence as observed from the energy content at high frequencies in the horizontal and vertical energy spectra (figure 5.5a and b). For the lower Fr of 0.25, the streamwise locations $0.5 < x_1/D < 3$ have $0.1 < Re_b < 1$. At these streamwise locations, the vortices are still attached as shown in figure 5.3(c) and no small scale features are present. Some of the small scales observed in the $Fr = 0.25$ case (figure 5.3c) at $x_1/D = 4 - 5$ are consistent with $Re_b \gtrsim 1$ in this region. Small scales observed in figure 5.3(e) are consistent with the $O(1)$ values of Re_b for $Fr = 0.125$ at locations $1.14 < x_1/D < 2.75$ where $Re_b < 1$ and the flow transitions towards quasi-2D dissipation. For $Fr = 0.025$, $Re_b << 1$ at all x_1/D locations. There is vertical shear between pancake eddies as shown in figure 5.3(f) and (h) that is quasi laminar for small Re_b consistent with Brethouwer *et al.* (2007). Nevertheless the flow is far from laminar. The horizontal motion is unsteady owing to vortex shedding, there is broadband turbulence in the near wake as shown by velocity spectra, and there are small scales, e.g. thin braid vortices between the vortices being shed from the sphere (figure 5.3g) in the vorticity field.

From figure 5.8, it can be seen that for $Fr = 0.25$ and 0.125, the value of $Ri \approx 1/Re_b$ is $\lesssim 1$ and, therefore, secondary KH instabilities are present in the vertical layers (figure 5.3d and f). However, for $Fr = 0.125$ at $x_1/D > 5$, the value of $Ri > 1$ and for $Fr = 0.025$ the value of $Ri >> 1$ at all x_1/D locations. Hence, secondary instability is absent in the vertical layers at $x_1/D \approx 5$ location in figure 5.3(f) and at all locations in figure 5.3(h).

5.3 Conclusions

To summarize, although turbulence decreases and is almost extinguished when stratification increases and Fr decreases to 0.5, it is regenerated when Fr decreases further to 0.25 and beyond at $Re = 3,700$. This new finding is contrary to the belief that turbulence suppression is monotone with increasing stratification for flow past a sphere that was based on experiments at low Re. Owing to the suppression of vertical motion, the fluid moves horizontally around the sphere. This leads to a new regime of unsteady vortex shedding with frequency similar to that for a circular cylinder, there is transition to broadband turbulence if Re is sufficiently large, and the enhanced shear of the horizontal motion feeds energy into the fluctuation energy. The buoyancy Reynolds number is $Re_b = O(1)$ at locations in the low-Fr wake where quasi-2D vortices are accompanied with small-scale features in vertical layers between these vortices. Future simulations of flow past a sphere at higher Re are desirable to explore the low-Fr dynamics of the near wake at higher Re_b.

5.4 Acknowledgements

Chapter 5, in full, is a reprint of the material as it appears in Journal of Fluid Mechanics Rapids 2016, coauthored by Professor Sutanu Sarkar, Dr.Antonio Posa and Professor Elias Balaras. A. Pal, S. Sarkar, A. Posa & E. Balaras, Regeneration of turbulent fluctuations in low-Froude number flow over a sphere at a Reynolds number of 3700, *J. Fluid Mech.*, 804, R2, 1-11 (2015).
The thesis author was the primary author of this paper.

Chapter 6

Internal waves generated by flow past a sphere at a Reynolds number of 3700 in a stratified fluid.

6.1 Introduction

Translation of bluff bodies in a stratified environment is responsible for the generation and subsequent propagation of internal gravity waves. In the ocean, flow over topographies and movement of submerged bodies and in the atmosphere, flow over mountains are the prime sources of internal wave generation (Lighthill, 1955; Baines, 1995). Such internal waves can be classified as: (a) lee waves which are generated by the fluid displaced by the moving body, and (b) wake generated internal waves induced by the turbulent wake behind the body. These internal waves transport momentum, increase the drag and, if they subsequently break, contribute to the turbulent mixing and transport of the nutrients and pollutants in the ocean and atmosphere. In this paper, we focus on the dynamics and the properties of these two types of internal waves generated by flow past a sphere at $Re = 3700$ and $Fr \in [0.025, 3]$.

Investigations of the lee waves and random waves generated by a moving sphere and its wake, respectively, have been performed using experimental (Gilreath & Brandt, 1985; Hopfinger *et al.*, 1991; Bonneton *et al.*, 1993; Chomaz *et al.*, 1993a; Bonneton *et al.*, 1996; Brandt & Rottier, 2015), numerical (Abdilghanie & Diamessis, 2013) and theoretical techniques (Voisin, 1991, 1994, 2007). Gilreath & Brandt (1985) reported a strong coupling between wake turbulence and random internal waves.

Brandt & Rottier (2015) recently performed a series of experiments for Fr ($Fr = U/ND$, where U is the towing speed of the sphere, D is the diameter of the sphere and N is the buoyancy frequency) in the range of $[0.1, 5]$ and $Re \in [10^3,\ 2.2 \times 10^4]$. They concluded that for $Fr \lesssim 1$ the sphere is the source of wave generation (lee waves are dominant) whereas for $Fr \gtrsim 1$, the turbulent wake is the primary wave generator (random waves prevail). They also found that at $Fr \lesssim 1$, the input energy into the domain is primarily converted to the potential energy of the lee waves. A maximum of 70% conversion of the input energy into the lee wave potential energy is observed at $Fr \sim 0.5$.. For $Fr \gtrsim 1$, Brandt & Rottier (2015) showed that the input energy primarily goes into the turbulent wake.

Previous stratified wake simulations (Brucker & Sarkar, 2010; Abdilghanie & Diamessis, 2013) have studied internal waves with a temporal flow model. Since the sphere was not included in these simulations, the dynamics of the lee waves and their interaction with the random waves were not captured. Linear theory predicts various aspects of the lee waves. However the linear model considers a moving point source and hence lacks the effect of the boundary layer and shear layer of a sphere on the dynamics of the lee waves. The present simulations capture all the boundary layer and shear layer dynamics as reported in Pal *et al.* (2016*b*,*a*) and Chongsiripinyo *et al.* (2016) and, therefore, provide higher fidelity representation of the wave field. We examine the partition of the input potential energy between the lee and random modes of the internal waves and the variation of the drag on the sphere owing to the lee-waves and the turbulent wake in the present work.

Table 6.1: Simulation parameters. The sphere is located at $(0, 0, 0)$. The substantial domain size in the radial and upstream direction, along with the sponge region, eliminates the spurious reflection of internal waves. $L_\theta = 2\pi$ and $N_\theta = 128$.

Case	*Re*	*Fr*	L_r	L_z	N_r	N_z
1.	3700	0.025	58	63 (40 upstream; 23 downstream)	690	3072
2.	3700	0.033	58	56 (40 upstream; 16 downstream)	690	2560
3.	3700	0.05	58	63 (40 upstream; 23 downstream)	690	3072
3.	3700	0.066	58	56 (40 upstream; 16 downstream)	690	2560
4.	3700	0.125	58	120 (40 upstream; 80 downstream)	690	4608
5.	3700	0.17	58	56 (40 upstream; 16 downstream)	690	2560
6.	3700	0.21	58	56 (40 upstream; 16 downstream)	690	2560
7.	3700	0.25	58	120 (40 upstream; 80 downstream)	690	4608
8.	3700	0.5	58	120 (40 upstream; 80 downstream)	690	4608
9.	3700	0.6	58	120 (40 upstream; 80 downstream)	690	4608
10.	3700	0.7	58	120 (40 upstream; 80 downstream)	690	4608
11.	3700	0.8	58	120 (40 upstream; 80 downstream)	690	4608
12.	3700	1	58	103 (25 upstream; 80 downstream)	690	4608
13.	3700	3	58	95(13 upstream; 80 downstream)	690	4608

6.2 Problem formulation and numerical details.

We use DNS to investigate the flow past a sphere at $Re = 3,700$ and $Fr \in \{0.025, 1\}$. The details of the governing equation and numerical method is discussed in chapter 4 and Pal *et al.* (2016*a*).

6.3 Comparison of DNS with Linear theory

A comparison of the vertical velocity u_3 between the present DNS and linear theory is shown in figure 6.1. The calculation of the vertical velocity of a moving point mass source using Green's function approach is given by Voisin (1994). The present DNS captures the lee-wave pattern similar to the findings of Voisin (1994) using linear theory. This similarity in the lee-wave pattern supports the fact that these lee-waves are linear in nature as compared to the random waves. The non-linearity in the system generates wake turbulence leading to the generation of

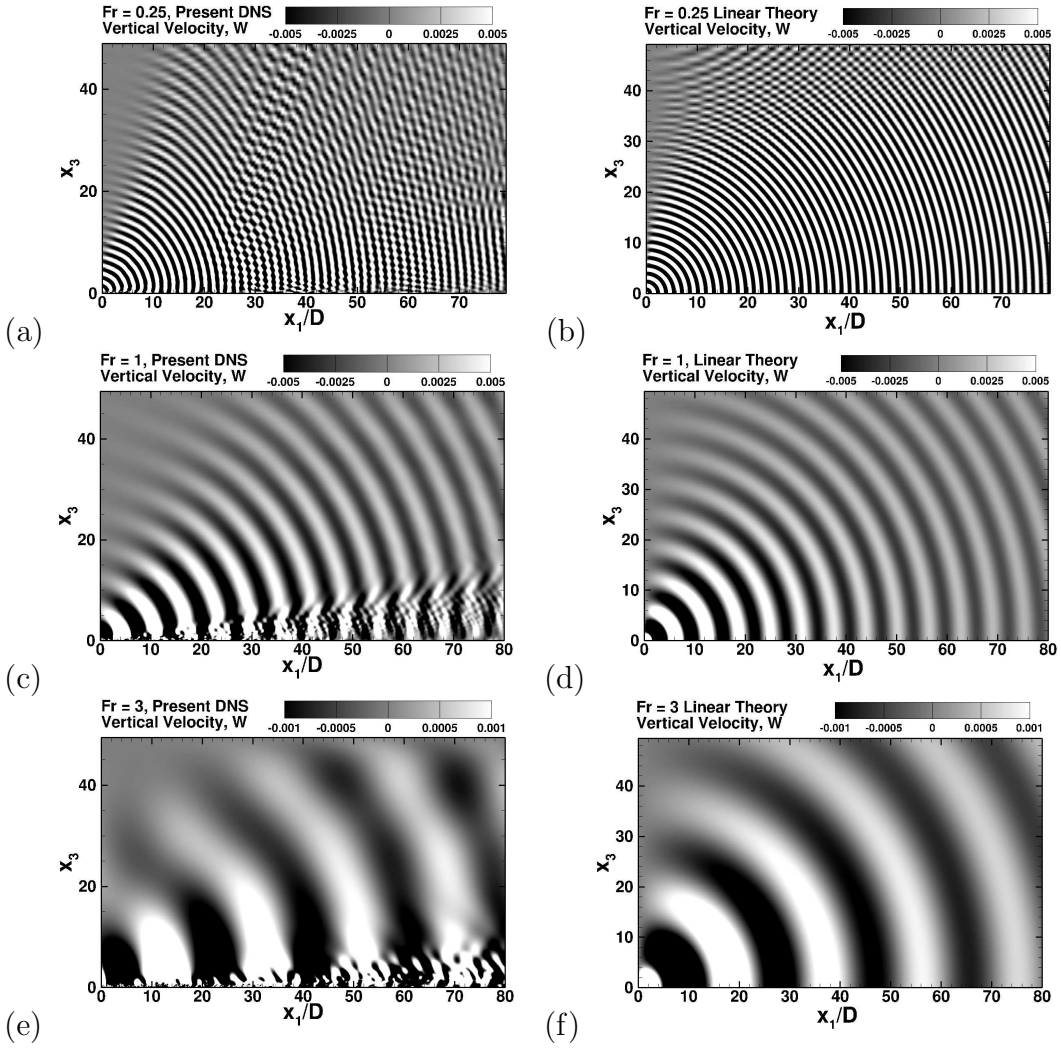

Figure 6.1: Comparison of vertical velocity contour plots at vertical ($x_2 = 0$) planes: (a) DNS, Fr = 0.25, (b) linear theory, Fr = 0.25, (c) DNS, Fr = 1, (d) linear theory, Fr = 1, (e) DNS, Fr = 3, and (f) linear theory, Fr = 3.

random waves. For $Fr = 0.25$, the signature of these random waves can be observed near the centerline as secondary oscillations. These secondary oscillations, when propagating away from the center, disturb the steady lee-waves pattern as seen from figure 6.1(a). The random waves for $Fr = 1$ are stronger than the $Fr = 0.25$ case. A clear distinction between the lee waves and the random waves for $Fr = 1$ is observed in figure 6.1(c). With the increase in Fr to 3, the lee-waves becomes weaker than the rest of the cases whereas the random waves are stronger owing to increased turbulence (figure 6.1(e)). The qualitative comparison of the lee-waves between the DNS and linear theory shows a good match. For quantitative comparison, vertical velocity at $x_3/D = 10$ at vertical plane is shown in figure 6.2. The wavelength and amplitude of the lee-waves for $Fr = 1$ and 3 show a good match between DNS and linear theory, but a phase shift is observed for both the cases. This phase shift and relative mismatch between DNS and linear theory can be attributed to the presence of an actual body in the present simulation as compared to an assumed point source. For $Fr = 0.25$ the boundary layer is attached to the body longer than for $Fr = 1, 3$ (Pal *et al.*, 2016*b*). The shear layer for $Fr = 0.25$ in the vertical direction unlike $Fr = 1, 3$ has an oscillating pattern and do not shed from the body (Pal *et al.*, 2016*b*). These two factors drastically reduce the linearity of the lee-waves for $Fr = 0.25$.

6.4 Internal wave potential energy

To understand the dynamics of the two different type of waves (lee and random), it is required to first separate them from each other. We follow a similar method to that adopted by Brandt & Rottier (2015). The lee waves vary in space (x_1, x_2, x_3), but are steady in time. Therefore, time averaging of a variable (ϕ) will produce mean quantities independent of time and hence will include the lee waves. The quantity left after removing the mean from the actual variable (ϕ) will include the random waves. The variable ϕ is chosen to be du_3/dx_3 to focus on the wave field. We perform the following decomposition:

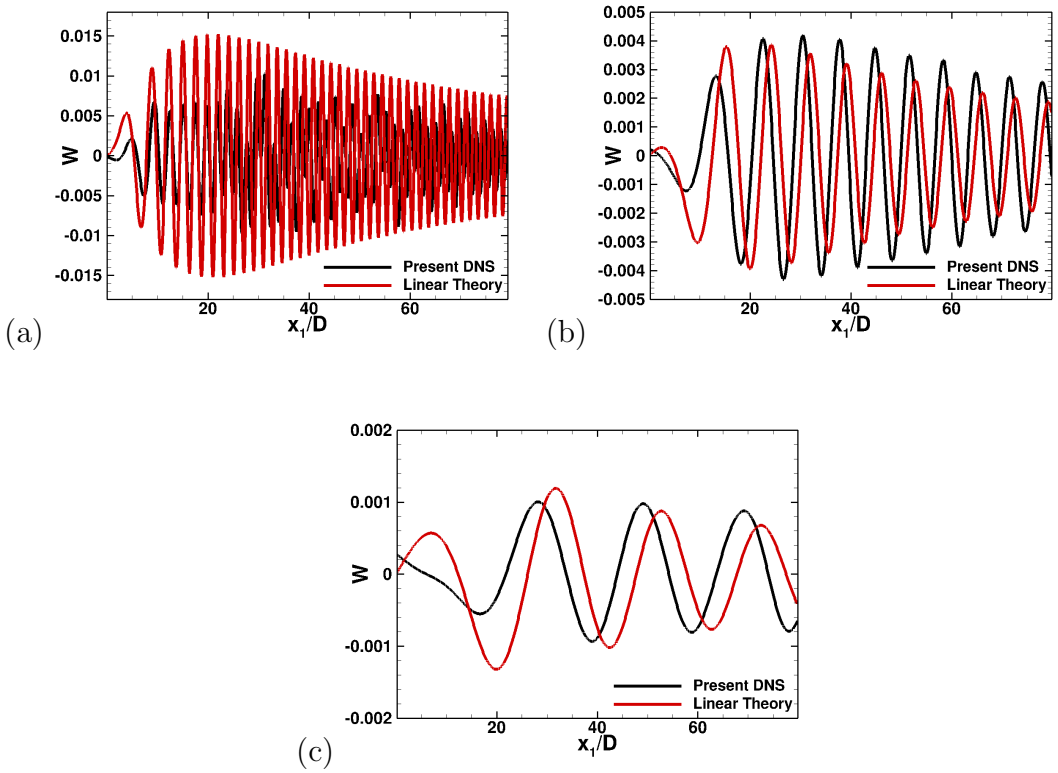

Figure 6.2: Comparison of vertical velocity obtained from DNS and linear theory using line plots at $x_3/D = 10$ on the vertical ($x_2 = 0$) planes: (a) Fr = 0.25, (b)Fr = 1, (c)Fr = 3.

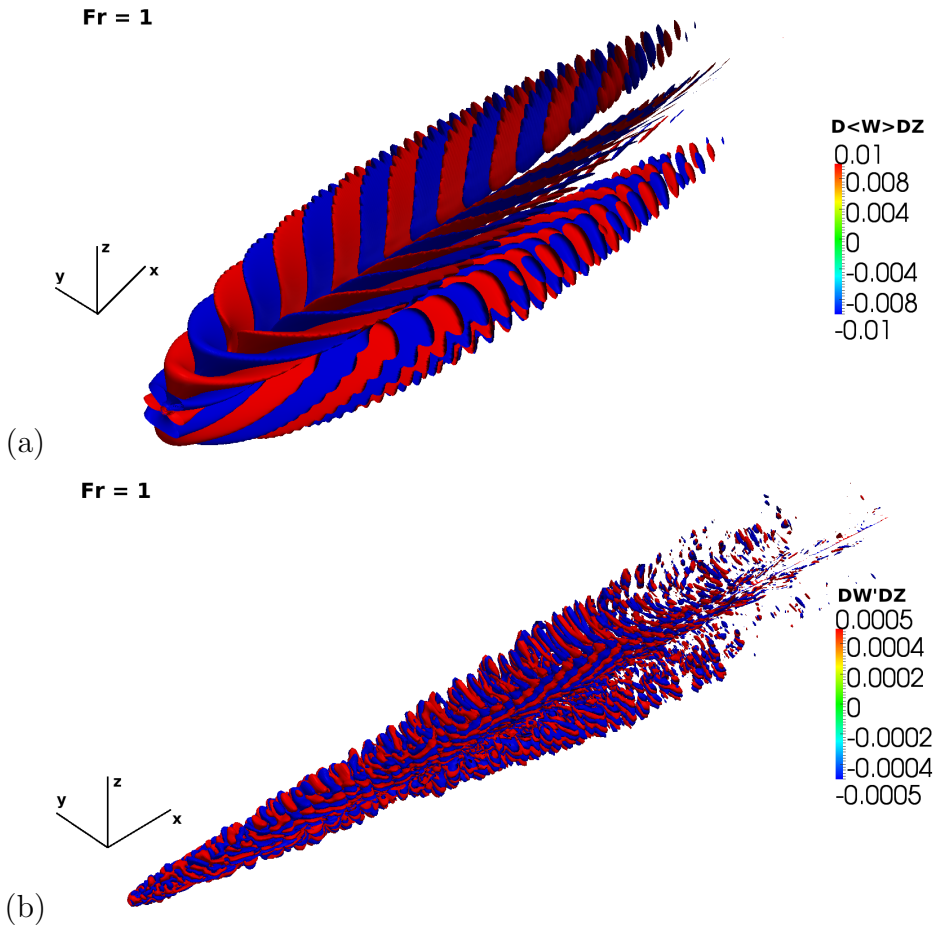

Figure 6.3: Three-dimensional visualization: (a) lee waves, and (b) random waves.

$$\frac{du_3}{dx_3}(x_1, x_2, x_3, t) = \langle \frac{du_3}{dx_3}(x_1, x_2, x_3) \rangle + (\frac{du_3}{dx_3}(x_1, x_2, x_3, t))' \tag{6.1}$$

where $\langle\ \rangle$ represents time averaging. Figures 6.3 (a)-(b) show the 3-dimensional visualization of $\langle \frac{du_3}{dx_3}(x_1, x_2, x_3) \rangle$ and $(\frac{du_3}{dx_3}(x_1, x_2, x_3, t))'$ respectively for $Fr = 1$. The lee waves are organized in a sheet like pattern with longer wavelengths and low frequency as seen in figure 6.3(a). The random waves (figure 6.3b) however manifest much shorter wavelengths and high frequency modes.

The strength of the internal waves (lee waves and random waves) with the

variation in intensity of stratification is characterized by computing the potential energy E_p. The potential energy of the internal waves is calculated in terms of the wave amplitude ζ, recorded from the displacement of the isopycnals by Brandt & Rottier (2015) using the following equation:

$$E_p = \frac{1}{2}\rho_0 N^2 \zeta^2. \tag{6.2}$$

However ζ is related to the density deviation $\widetilde{\rho}$, e. g. via Kundu & Cohen (2011):

$$\widetilde{\rho} = \frac{N^2 \rho_0 \zeta}{g}, \tag{6.3}$$

$$\zeta = \frac{g\widetilde{\rho}}{N^2 \rho_0}, \tag{6.4}$$

$$E_p = \frac{g^2 \widetilde{\rho}^2}{2\rho_0 N^2}. \tag{6.5}$$

E_p can be decomposed into a steady (lee-wave) and fluctuating (random-wave) component similar to (6.1) as follows:

$$E_p(x_1, x_2, x_3, t) = \langle E_p(x_1, x_2, x_3) \rangle + (E_p(x_1, x_2, x_3, t))'. \tag{6.6}$$

We compute the $r.m.s$, $E_{p,rms}$ of $(E_p(x_1, x_2, x_3, t))'$. The area integrated plots of $\langle E_p \rangle$ and $E_{p,rms}$ for different Fr is shown in figure 6.5(a)-(b). For $Fr = 3$, for $0.5 < x_1/D < 4$ the lee waves are the dominant internal waves and this is verified by the higher potential energy of the lee waves as compared to the random-waves within this regime. The recirculation region for $Fr = 3$ is at $x_1/D \sim 2$ after which the intensity of the lee-waves starts decreasing as observed from the decline in $\langle E_p \rangle$. The intensity of the random-waves increases continuously behind the body and overpowers the lee waves as $x_1 \sim 4$. This is justified by the similar distribution of the potential energy between the lee and random waves at $x_1/D \sim 4$. Between $4 < x_1/D < 15$, $E_p^{'}$ dominates signifying the higher intensity of random waves as compared to lee waves. Beyond $x_1/D \sim 15$, the strength of both lee and random waves decrease as shown by a similar decline in $\langle E_p \rangle$ and $E_{p,rms}$. With the increase in stratification ($Fr = 1$), the turbulence behind the sphere is suppressed

and therefore a decrease in the intensity of random-waves with respect to lee-waves will occur. This is evident from the dominance of $\langle E_p \rangle$ over $E_{p,rms}$ across the entire domain. Pal *et al.* (2016*b*) found that turbulence extinguishes completely at $Fr = 0.5$ and therefore the entire potential energy of the system converts only into $\langle E_p \rangle$ and the lee-waves for $Fr = 0.5$ are strongest among all the cases. The turbulence regenerates progressively with decrease in Fr from 0.25 to 0.125 and 0.025, as explained in Pal *et al.* (2016*b*) primarily in the horizontal direction. This regenerated turbulence for $Fr = 0.25$ is weaker than $Fr = 0.125$ and 0.025 cases. As $Fr = 0.25$ has lower turbulence intensity, the random waves have less potential energy compared to the lee waves. As the turbulence becomes stronger for $Fr = 0.125, 0.025$ in the horizontal direction, the potential energy of both lee and random waves decreases as compared to $Fr = 0.25$. For $Fr = 0.125$, owing to the oscillations in the attached shear layer in the vertical direction as observed in figure 6.4(b) (**?**) the lee waves are stronger as compared to the random-waves till $x_1/D < 4$. An similar distribution of potential energy between the lee and random modes is observed after $x_1/D \sim 4$ for $Fr = 0.125$. There is a decrease in the intensity of lee-waves for $Fr = 0.025$ as seen from figure 6.4(c) owing to the non-oscillatory nature of the shear layer. This suppression of the undulation of the shear layer for $Fr = 0.025$ is associated with the low buoyancy Re. As the lee waves are weaker and the turbulence is generated in the horizontal direction, a similarity in observed in the evolution of $\langle E_p \rangle$ and $E_{p,rms}$ for $Fr = 0.025$.

6.5 The Fr dependence of the drag coefficient.

The drag force exerted by the fluid on a body in relative motion is of fundamental importance. The non-dimensional drag coefficient $C_d(Re, Fr)$ as a function of Re and Fr is defined as:

$$C_d(Re, Fr) = \frac{F}{\frac{1}{8}\rho_0 U_\infty^2 \pi D^2}, \tag{6.7}$$

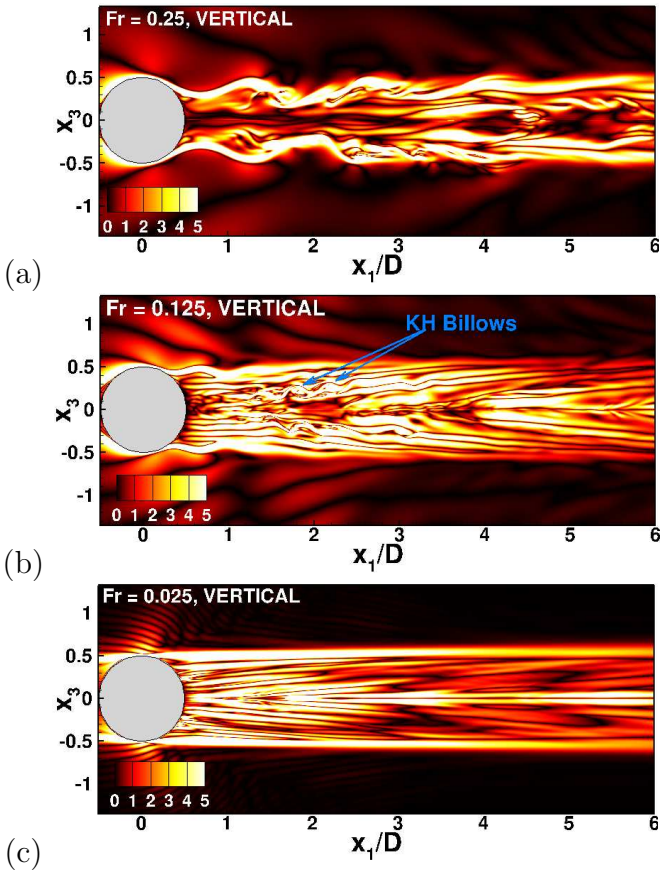

Figure 6.4: Instantaneous azimuthal vorticity magnitude on the vertical $x_1 - x_3$ plane ($x_2 = 0$). Snapshots compared among cases with different Fr.

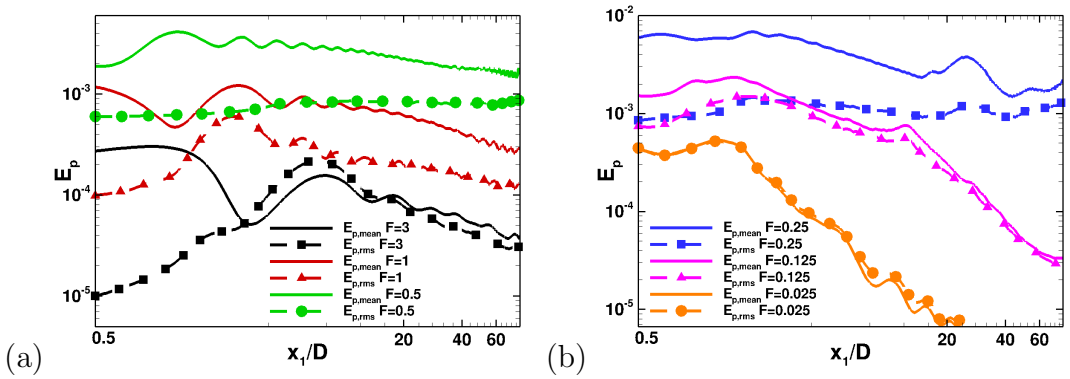

Figure 6.5: Streamwise evolution of area-integrated potential energy : (a) $Fr = 3, 1, 0.5$, and (b) $Fr = 0.25, 0.125, 0.025$.

where F is the magnitude of the drag force, ρ_0 is the background density, U_∞ is the free-stream velocity and D is the diameter of the sphere. The drag force F is a combination of the pressure and viscous force. Therefore, $C_d = C_p + C_f$, where C_p and C_f are the pressure and the skin-friction coefficients, computed from the surface force component, f_i, in x_i direction as follows:

$$f_i = \tau_{ji} n_j = [-p\delta_{ij} + \mu(\frac{\partial u_i}{\partial x_j} + \frac{\partial u_j}{\partial x_i})]n_j \tag{6.8}$$

$$C_p = \frac{1}{\frac{1}{8}\rho_0 U_\infty^2 \pi D^2} \int_S (-p\delta_{ij}) n_j dS_j, \tag{6.9}$$

$$C_f = \frac{1}{\frac{1}{8}\rho_0 U_\infty^2 \pi D^2} \int_S \mu(\frac{\partial u_i}{\partial x_j} + \frac{\partial u_j}{\partial x_i}) n_j dS_j, \tag{6.10}$$

where τ_{ji} is the stress tensor, n_j is the direction cosine of outward unit normal vector, $\mathbf{n}$ to the sphere surface and dS_j is the surface area component in the direction of n_j. $C_d(Re, Fr = \infty)$ is defined as the drag coefficient for the unstratified case and its time averaged value is computed in our unstratified simulation as 0.3938. To examine the effects of stratification only, we compute:

$$\Delta C_d(Re, Fr) = C_d(Re, Fr) - C_d(Re, \infty). \tag{6.11}$$

Figure 6.6 compares the variation of ΔC_d with Fr^{-1} among previously reported studies. All the previous studies (Lofquist & Purtell, 1984; Hanazaki, 1988; Orr *et al.*, 2015) report that ΔC_d will *increase* with increasing stratification (decrease in Fr) up to a certain point, after which it will start decreasing. Theoretical modeling of Greenslade (2000) and Voisin (2007) also gives a similar behavior of ΔC_d with increase in stratification. Lofquist & Purtell (1984) performed experiments with a range of Re and Fr, and postulated that the change ΔC_d due to stratification is unaffected by Re. However, for lower Re, Lofquist & Purtell (1984) have low values of Fr and vice versa. The numerical investigation of Hanazaki (1988) considered only low $Re = 200$. The simulations of Orr *et al.* (2015) also plotted the time-averaged ΔC_d for $Re = 200$ and low Fr as shown in

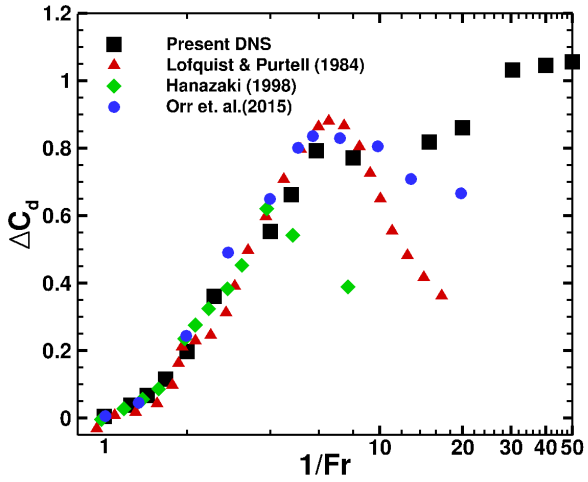

Figure 6.6: Variation of change in drag, ΔC_d with Fr^{-1}.

figure 6.6. In contrast to all these low Re studies, an *increase* in ΔC_d is observed for the present low Fr cases suggesting that, in fact, Re plays a significant role in determining the drag force at high stratification. Experimental studies of Castro *et al.* (1990); Vosper *et al.* (1999) for flow over orography at relative higher Re and low values of Fr also suggest an increase in ΔC_d. Castro *et al.* (1990) used a half sinusoidal shape and *"Witch of Agnesi"* shape obstacle for their study whereas Vosper *et al.* (1999) used two sizes of hemisphere and two cones of different slope for their study. An increase in C_d is reported by Vosper *et al.* (1999) for the hemisphere with larger diameter (higher Re) at low Fr. This increase in C_d is also accompanied by local minima and maxima. They concluded that these oscillations in C_d are a consequence of the finite size of the tank used in their experiment.

6.6 Future work

Further analysis of the pressure distribution on the surface of the sphere, as a function of Fr is required to understand the increase in ΔC_d. The drag force on the sphere at low Fr has two components as formulated by Greenslade (2000); Voisin (2007). One component is the drag owing to the waves and another is the drag due to the wake. Therefore, C_d can be defined as a $C_{d,wave} + C_{d,wake}$. It will

be interesting to compute these terms separately and understand the contribution of each component as the stratification increases. Existing linear theory models predict the variation of C_d for low Re. It will be intriguing to explore if development of a model is possible to predict C_d for moderate to high Re at low values of Fr.

Another aspect of this investigation is to quantify the propagation angle of the lee and random waves. The random waves observed in the numerical simulations of Abdilghanie & Diamessis (2013) cluster in a band around approximately 45° propagation angle. Similar propagation angles are observed in the laboratory experiments (Sutherland & Linden, 1998; Dohan & Sutherland, 2003) and numerical simulations (Taylor & Sarkar, 2007; Pham *et al.*, 2009) of waves emitted by broad-band turbulence. The high- and low-frequency components (correspondingly, high and low propagation angles with respect to the horizontal) of the wave field were found to exhibit preferential viscous decay consistent with the model proposed by (Taylor & Sarkar, 2007). It will be interesting to see if the preferential viscous decay hypothesis also applies to the random waves of the present simulations.

6.7 Acknowledgements

Contents of this chapter are *in preparation* for publication in *Journal of Fluid Mechanics* coauthored by Professor Sutanu Sarkar. A. Pal & S. Sarkar , Internal waves generated by flow past a sphere at a Reynolds number of 3700 in a stratified fluid. The thesis author is the primary author of this paper.

Chapter 7

Summary and Conclusions

In the first phase (Pal *et al.*, 2013) of the thesis research, the primary focus is to contrast the influence of the mean velocity profile with that of the initial turbulence on the subsequent evolution of velocity and density fluctuations in a stratified wake. Direct numerical simulation is used to simulate the following cases: (a) a self-propelled momentumless turbulent wake, case SP50 with a canonical mean velocity profile, (b) a patch of turbulence, case TP1 with the same initial energy spectrum as (a), and (c) a patch of turbulence, case TP2 with a different initial energy spectrum with higher small-scale content. The evolution of the fluctuations is found to be strongly dependent on the initial energy spectrum, e.g., in case TP2, the kinetic energy is substantially smaller, and the late-wake vortices are less organized. The effect of the mean velocity field is negligible for mean kinetic energy (MKE) of the order 10% of the total kinetic energy and the evolution in this case is similar to a turbulent patch with the same initial energy spectrum. Increasing the MKE to 50% shows significant difference from the turbulent patch with the same initial energy spectrum during the initial stages of the evolution, but at later stages the evolution of turbulence statistics is similar. Both the turbulent patch and the momentumless wake show layering and formation of pancake eddies owing to buoyancy. Another objective of the paper is to compare the spatially evolving wake with the temporally evolving approximation when the initial near-wake condition of the temporal approximation is chosen to match the inflow of the spatially evolving model. The mean and turbulent flow statistics are found to agree well

between the spatial and temporal computational models under these conditions.

In the second phase, direct numerical simulations are performed to study the evolution of a towed stratified wake subject to external turbulence in the background. A field of isotropic turbulence is combined with an initial turbulent wake field and the combined wake is simulated in a temporally evolving framework similar to that of (Rind & Castro, 2012*a*). Simulations are performed for external turbulence whose initial level varies between zero and a moderate intensity of up to 7% relative to the free stream and whose initial integral length scale is of the same order as that of the wake turbulence. A series of simulations are carried out at a Reynolds number of 10 000 and Froude number of 3. Background turbulence, especially at a level of 3% or above, is found to have substantial quantitative effects in the stratified simulations. Turbulence inside the wake increases due to the entrainment of external turbulence, and the energy transfer through turbulent production from mean to fluctuating velocity also increases, leading to reduced mean velocity. The profiles of normalized mean and turbulence quantities in the stratified wake exhibit little change in the vertical direction but the horizontal spread increases in comparison to the case with undisturbed background. The spatial organization of the internal wave field is disrupted even at the 1% level of external turbulence. However, key characteristics of stratified wakes such as the formation of coherent pancake vortices and the long lifetime of the mean wake are robust to the presence of fluctuations in the background. A corresponding series of simulations for the unstratified situation is carried out at the same Reynolds number of 10 000 and with similar levels of external turbulence. The change of mean and turbulence statistics is found to be weaker in the unstratified cases compared with the corresponding stratified cases and also weaker relative to that found by (Rind & Castro, 2012*a*) at a similar level of external turbulence relative to the free stream and similar integral length scale. Theoretical arguments and additional simulations are provided to show that the level of external turbulence relative to wake turbulence (dissimilar between the present investigation and Rind & Castro (2012*a*) is a key governing parameter in both stratified and unstratified backgrounds.

The previous simulations of the turbulent wakes in the thesis are performed without the body. In the third phase of the thesis, DNS of flow past a sphere in a stratified fluid, including the body, is carried out at a sub-critical Reynolds number of 3700 and $Fr = U_\infty/ND = 1, 2$ and 3 to understand the dynamics of moderately stratified flows with $Fr = O(1)$. Here, U_∞ is the free stream velocity, N is the background buoyancy frequency and D is the diameter. The unstratified flow past the sphere consists of a separated shear layer that transitions to turbulence, a recirculation zone, and a wake with a mean deficit velocity, U_0, that decreases with downstream distance as a power law. With increasing stratification, the separated shear layer plunges inward vertically and its roll-up is inhibited, the recirculation zone is shortened, and the mean wake decays at a slower rate of $U_0 \propto (x_1/D)^{-0.25}$ in the non-equilibrium (NEQ) region. The longer lifetime of the mean wake is due to a reduction of turbulent production by buoyancy. The transition from the near wake where U_0 has a decay rate similar to the unstratified case to the NEQ regime occurs as an oscillatory modulation by a steady lee wave pattern with a period of $Nt = \pi$ that leads to a period of accelerated U_0 between $Nt = \pi$ and approximately $Nt = 2\pi$. Far downstream, the wake is dominated by coherent horizontal motions. The intensity, spectral content and structure of turbulent fluctuations in the wake are assessed. Buoyancy induces significant anisotropy among the velocity components and between their vertical and horizontal profiles. Consequently, the near wake ($x_1/D < 10$) exhibits significant differences in turbulence profiles relative to its unstratified counterpart. Spectra of vertical velocity show a discrete peak in the near wake that is maintained further downstream. The turbulent kinetic energy (TKE) balance is computed and contributions from pressure transport and buoyancy are found to become increasingly important as stratification increases.

As a followup problem, DNS are performed to study the behavior of flow past a sphere in the regime of high stratification ($Fr < O(1)$). In contrast to previous results at lower Re that suggest monotone suppression of turbulence with increasing stratification in flow past a sphere, it is found that, below a critical Fr,

increasing the stratification induces unsteady vortical motion and turbulent fluctuations in the near wake. The near wake is quantified by computing the energy spectra, the turbulence energy equation, partition of energy into horizontal and vertical components, and the buoyancy Reynolds number. These diagnostics show that the stabilizing effect of buoyancy changes flow over the sphere to flow around the sphere. This qualitative change in the flow leads to a new regime of unsteady vortex shedding in the horizontal planes that results in turbulence regeneration.

In the final phase of this study, a detailed analysis of the two different types of internal waves generated owing to the fluid motion past the body is performed. The waves generated due to the movement of the fluid over the body generates lee waves whereas the turbulent wake gives rise to random waves. The behavior of these waves in terms of energy content, wavelength, frequency differ significantly with the variation in the stratification. It is also found that the drag coefficient C_d *increases* with the increase in stratification even in the low-Fr regime.. This finding is in contrast with the previous studies, where a *decrease* in C_d is reported in this regime. A more detailed analysis of the variation of wave drag with respect to wake drag with the increase in stratification will be conducted in future work.

Appendix A

Immersed Boundary Method

This section is taken from chapter 3 of Yang (2005) discussing the immersed boundary method.

A.0.1 Interface Description

In the present formulation, the interface is explicitly described independent of the underlying grid. As shown in figure A.1, a two-dimensional immersed interface, ψ, can be represented by a series of interfacial marker particles, which are defined by arc length coordinates $X(s,t)$. The immersed interface can have arbitrary shape and it can be open or closed. The marker particles are evenly attached to the interface with a spacing approximating the local grid size, and the beginning of the arclength coordinate is defined such that the fluid (or interested side of the interface) is always to the left of the observer as one moves along the interface toward increasing s. For each marker particle with arclength coordinates X_i, the functions defining the coordinates can be written as

$$x(s,t) = a_x s^2 + b_x s + c_x \qquad y(s,t) = a_y s^2 + b_y s + c_y \tag{A.1}$$

These functions are generated at each sub-step of the splitting scheme for moving interfaces. The coefficients $a_{x,y}, b_{x,y}, c_{x,y}$ can be obtained by fitting quadratic polynomials to particle (i) and its two neighbors $(i-1)$ and $(i+1)$. The normal from any location on the interface to the fluid can be calculated by the following

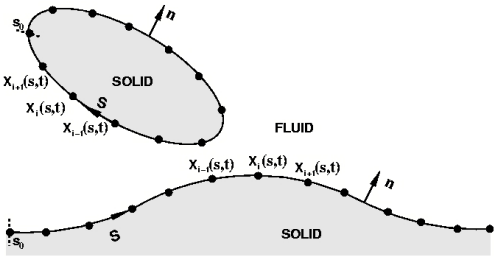

Figure A.1: The parametrized description of interfaces of arbitrary shapes using marker particles.

equations:

$$n_x = \frac{-y_s}{\sqrt{(x_s^2 + y_s^2)}} \qquad n_y = \frac{x_s}{\sqrt{(x_s^2 + y_s^2)}} \tag{A.2}$$

where the derivatives,x_s, y_s can be evaluated from the functions in eq. (A.1) above as follows,

$$x(s,t) = 2a_x s + b_x \qquad y(s,t) = 2a_y s + b_y \tag{A.3}$$

The coordinates $X(s,t)$ and the coefficients are stored for each marker particle on the interface. For three-dimensional interfaces Bi-spline fitting can be used.

A.0.2 Tagging of Points on the Eulerian Grid

Having defined the immersed interface as a series of marker particles, one can now establish the relationship between these particles and the underlying Eulerian grid. Figure A.2 (a) shows the parametrized interface immersed in a Cartesian grid. The procedure for tagging is summarized as below:

1. Determine the part of the grid occupied by the interface as the coordinates of each marker particle are known from the previous Section.

2. For those grid points, a search for the closest marker particle, s_b, is performed. A ray, $\mathbf{r}$, is shot from this marker particle to the grid point, and the dot product of $\mathbf{r}$ and $\mathbf{n_b}$ is calculated. 3. If $\mathbf{r} \bullet \mathbf{n_b} < \mathbf{0}$, then this grid point is inside the interface and assigned a tag of -1; otherwise, it is outside the interface and maintains its initial tag of 1 (figure A.2 (b)).

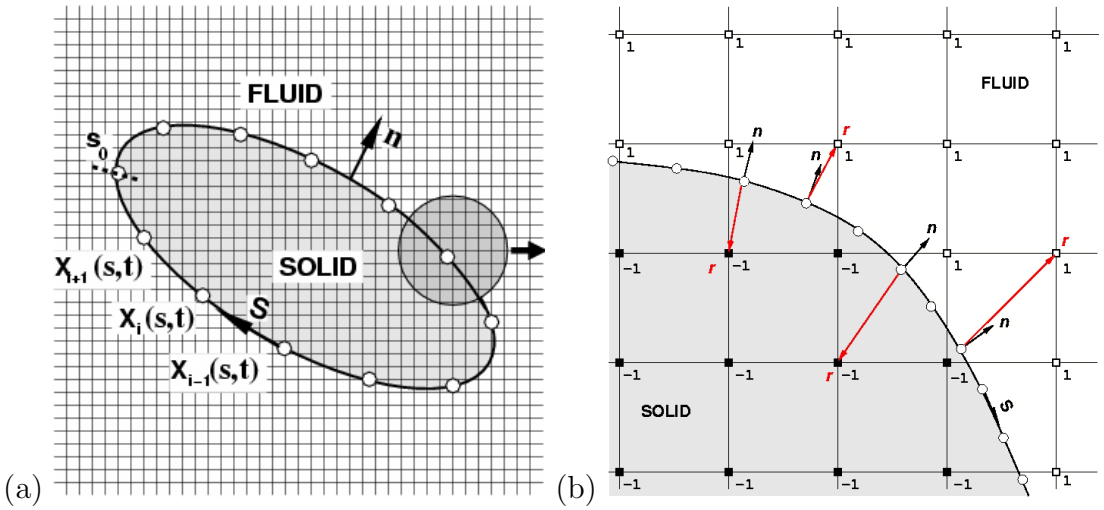

Figure A.2: Gridinterface relation. (a) Parametrized interface immersed in the underlying Cartesian grid; (b) Zoom in the vicinity of interface where the inside/outside status of the Eulerian grid points are shown. Fluid points; Solid points.

In the next step the boundary points are identified, which are points in the fluid phase with at least one neighboring point in the solid. A reconstruction procedure to estimate the predictor velocities will be carried out at these points. An example of the result of the flagging process is shown in figure A.3(a) where all Eulerian grid points are split into three different categories: (a) forcing points, which are grid points in the fluid phase that have one or more neighboring points in the solid phase; (b) solid points, which are all the points in the solid phase; (c) fluid points, which are all the remaining points in the fluid phase. In the solution procedure, the fluid points are the unknowns, the forcing points are boundary points, while the solid points do not influence the rest of the computation. For a stationary boundary the above tagging and flagging process is done only once at the beginning of the computation.

For a moving body the process is repeated at each timestep. In addition, another set of flags is used for the field extension treatment, which is shown in figure A.3(b). Again, all Eulerian grid points are split into three different categories: (a) pseudo-fluid points, which are grid points in the solid phase that have one or more neighboring points in the fluid phase; (b) solid points, which are all other

remaining points in the solid phase; (c) fluid points, which are all the grid points in the fluid phase. In the field extension procedure, the solution at those pseudo-fluid points are extrapolated from the known solution of the fluid points and the interface. It is obvious that the forcing points and the pseudo-fluid points are the points closest to the interface inside the fluid and inside the solid, respectively. The proper manipulation of those boundary points is very important to the success of the embedded boundary formulation.

A.0.3 Establishment of Interface-Normal Intersections

With the boundary points identified, the next task is to establish the information required for the reconstruction procedure. Central to this algorithm is the normal from the boundary points to the interface. This normal passes through boundary point (xi, yj) and intersects the interface at s_n, or (x_n, y_n). Therefore, the unit normal vector of this line is identical to the unit normal vector of the interface on point (x_n, y_n) and can be written as,

$$\frac{x_i - x_n}{\sqrt{(x_i - x_n)^2 + (y_j - y_n)^2}} = n_x = \frac{-y_s}{\sqrt{(x_s^2 + y_s^2)}} \tag{A.4}$$

$$\frac{y_j - y_n}{\sqrt{(x_i - x_n)^2 + (y_j - y_n)^2}} = n_y = \frac{x_s}{\sqrt{(x_s^2 + y_s^2)}} \tag{A.5}$$

The above equations can be combined to get

$$(x_i - x_n)x_s + (y_j - y_n)y_s = 0 \tag{A.6}$$

Substituting equ. A.3 in A.6 we obtain

$$(x_i - x_n)(2a_x s + b_x) + (y_j - y_n)(2a_y s + b_y) = 0 \tag{A.7}$$

$$s_n = \frac{-b_x(x_i - x_n) - b_y(y_j - y_n)}{2a_x(x - 1 - x_n) + 2a_y(y_i - y_n)} \tag{A.8}$$

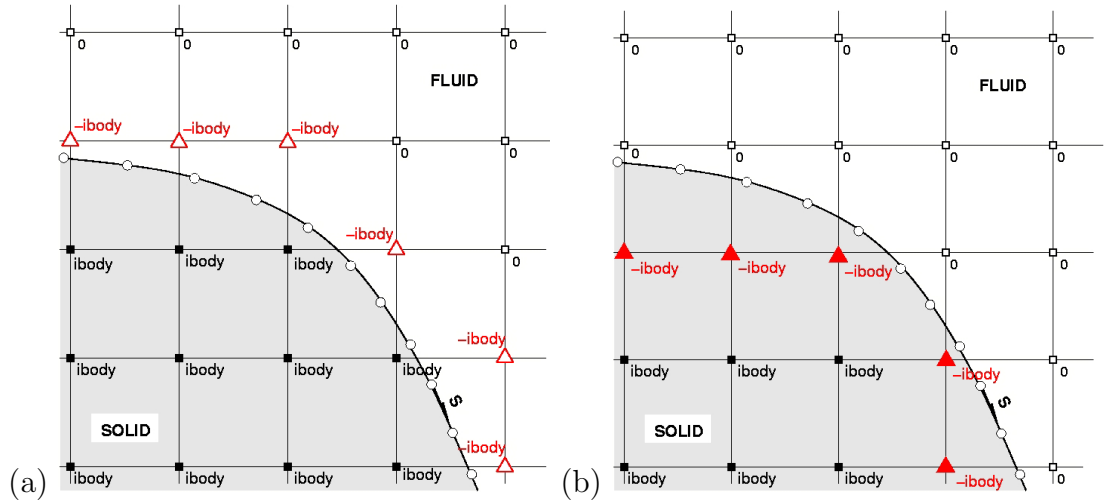

Figure A.3: Identification of boundary points. (a) 4 Forcing points, fluid points, and solid points for momentum forcing procedure; (b) N Pseudo-fluid points, fluid points, and solid points for field extension procedure.

Using A.1 for x_n and y_n will yield a cubic equation in s_n as follows,

$$(2a_x^2 + 2a_y^2)s_n^3 + \quad (3a_xb_x + 3a_yb_y)s_n^2 + (2a_xc_x + 2a_yc_y + b_x^2 + b_y^2 - 2a_xx_i - 2a_yy_j)s_n + (b_xc_x + b_yc_y - b_xx_i - b_yy_j) = 0. \tag{A.9}$$

and can be solved iteratively using Newton-Raphson method. The initial solution to this equation is the closest interfacial marker particle, s_b. Figure A.4 shows the schematic of the solution procedure from s_b to s_n. After obtaining s_n, the interface-normal intersection coordinates (x_n, y_n) and the unit normal vector n at the intersection can be calculated from eqns. A.1 and A.2.

A.0.4 Treatment of Stationary Immersed Boundaries

The calculation of the forcing function f_i^k for the cases where the Eulerian grid points coincides with the immersed interface ψ thereby enforcing the Dirichlet boundary condition has been discussed in details in Yang (2005). However, in most of the practical situations the Eulerian grid nodes never coincide with the immersed boundary. In such cases, f_i, has to be computed at grid points near and not exactly on the interface. Balaras (2004) proposed to perform the interpolation

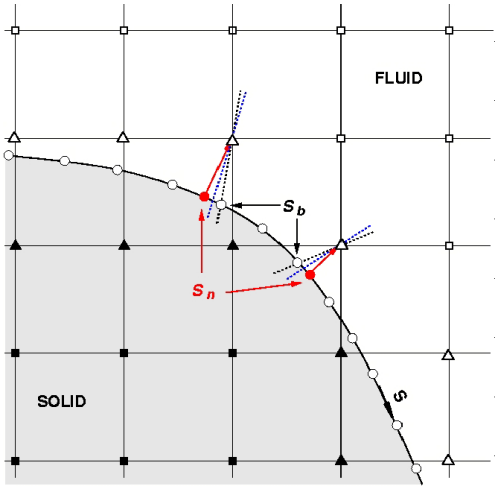

Figure A.4: Schematic of the solution procedure for interface-normal intersections. Forcing points, N Pseudo-fluid points, fluid points, and solid points.

along the well defined line normal to the boundary as illustrated in figureA.5(a): initially a virtual point is located along the normal; then, the virtual point together with the point on the interface is used to perform the linear interpolation to find the predicted velocities at the location of the forcing point. The predicted velocity at the virtual point is computed from the surrounding fluid nodes using bi-linear interpolation. In this last step, one also has to impose the constraint that the stencil does not involve other forcing points, which can be easily achieved by gradually moving the virtual point further away from the boundary (see for example Case 1 in figure A.5(a)).

A variation of the above method is adopted that is better suited to moving boundary problems. It utilizes, however, a more compact stencil and allows for the computation of all components of the strain rate tensor on the interface in a straightforward manner. In the present approach virtual point is replaced with two points on an x-grid line, y-grid line, or along the diagonal. Consequently, the interpolation procedure is now a single-step process that involves two points from the fluid and one on the interface (shaded area in figureA.5 (b)).

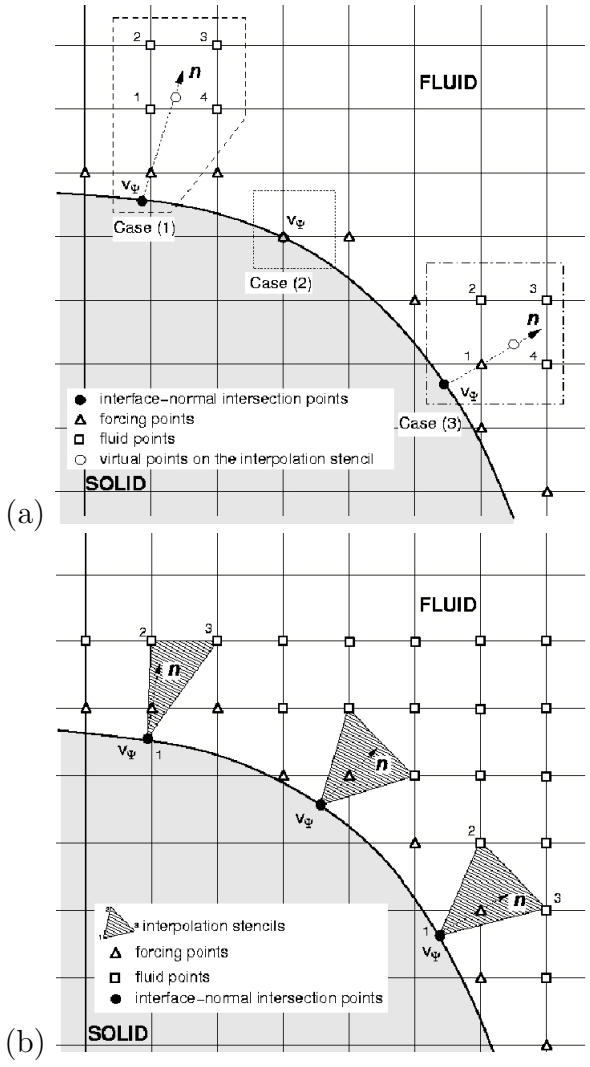

Figure A.5: Previous Interpolation schemes. (a) Two-dimensional scheme in Balaras (2004). Cases (1) and (3) illustrate two possible interpolation stencils depending on the interface topology and local grid size, (b)Generalized Interpolation stencil.

Table A.1: Validation of flow past a circular cylinder at different Reynolds number.

Case	40	100	300
Present Study	1.54	1.34	1.35
Mittal & Balachandar (1995)	1.53	1.35	1.36
Henderson (1995)	1.54	1.35	1.37
Marella (2005)	1.52	1.36	1.28

A.0.5 Numerical Procedure

Having established the treatment of all Eulerian points in the vicinity of a stationary or moving interface, we can summarize the overall algorithm as follows:
1. Given the location of the interface at step k, identify fluid, forcing, solid, and pseudo-fluid points on the Eulerian grid. This procedure needs to be performed only once in the beginning of the computation for problems with stationary boundaries.
2. Calculate the predicted velocity field u_i^k.
3. Reconstruct the predicted velocity u_i^k at the forcing points.
4. Solve the pressure Poisson equation.
5. Update the velocity field to u_i^k and pressure field to p^k.

References

Abdilghanie, A. M. & Diamessis, P. J. 2013 The internal gravity wave field emitted by a stably stratified turbulent wake. *J. Fluid Mech.* **720**, 104–139.

Amoura, Z, Roig, V, Risso, F & Billet, A-M 2010 Attenuation of the wake of a sphere in an intense incident turbulence with large length scales. *Phys. Fluids* **22**, 055105.

Arobone, E. & Sarkar, S. 2010 The statistical evolution of a stratified mixing layer with horizontal shear invoking feature extraction. *Phys. Fluids* **22**, 1–15.

Bagchi, Prosenjit & Balachandar, S 2004 Response of the wake of an isolated particle to an isotropic turbulent flow. *J. Fluid Mech.* **518** (1), 95–123.

Baines, P. 1995 *Topographic Effects in Stratified Flows.*. Cambridge University Press.

Balaras, E. 2004 Modeling complex boundaries using an external force field on fixed cartesian grids in large-eddy simulations. *Comput. Fluids* **33** (3), 375–404.

Bazilevs, Y., Yan, J., deStadler, M. & Sarkar, S. 2014*a* Computation of the flow over a sphere at Re = 3700: A comparison of uniform and turbulent inflow conditions. *J. Appl. Mech.* **81**, 121003.

Bazilevs, Y., Yan, J., de Stadler, M. & Sarkar, S. 2014*b* Computation of the flow over a sphere at Re= 3700: A comparison of uniform and turbulent inflow conditions. *J. Appl. Mech.* **81** (12), 121003.

Bevilaqua, Paul M & Lykoudis, Paul S 1978 Turbulence memory in self-preserving wakes. *J. Fluid Mech.* **89** (3), 589–606.

Bonneton, P., Chomaz, J. M., Hopfinger, E. & Perrier, M. 1996 The structure of the turbulent wake and the random internal wave field generated by a moving sphere in a stratified fluid. *Dyn. Atmos. Oceans* **23** (1), 299–308.

Bonneton, P., Chomaz, J. M. & Hopfinger, E. J. 1993 Internal waves produced by the turbulent wake of a sphere moving horizontally in a stratified fluid. *J. Fluid Mech.* **254**, 23–23.

Bonnier, M. & Eiff, O. 2002 Experimental investigation of the collapse of a turbulent wake in a stably stratified fluid. *Phys. Fluids* **14**, 791.

Brandt, A. & Rottier, J. R. 2015 The internal wavefield generated by a towed sphere at low Froude number. *J. Fluid Mech.* **769**, 109–129.

Brethouwer, G., Billant, P., Lindborg, E. & Chomaz, J.M. 2007 Scaling analysis and simulation of strongly stratified turbulent flows. *J. Fluid Mech.* **585**, 343–368.

Brucker, K. A. & Sarkar, S. 2007 Evolution of an initially turbulent stratified shear layer. *Phys. Fluids* **19**, 105105.

Brucker, K. A. & Sarkar, S. 2010 A comparative study of self-propelled and towed wakes in a stratified fluid. *J. Fluid Mech.* **652**, 373–404.

Castro, I. P., Snyder, W. H. & Baines, P. G. 1990 Obstacle drag in stratified flow. In *Proceedings of the Royal Society of London A: Mathematical, Physical and Engineering Sciences*, , vol. 429, pp. 119–140. The Royal Society.

Chen, CC, Gibson, CH & Lin, SC 1968 Measurements of turbulent velocity and temperature fluctuations in the wake of a sphere. *AIAA Journal* **6**, 642–649.

Chomaz, JM, Bonneton, P, Butet, A, Perrier, M & Hopfinger, EJ 1992 Froude number dependence of the flow separation line on a sphere towed in a stratified fluid. *Physics of Fluids A: Fluid Dynamics (1989-1993)* **4** (2), 254–258.

Chomaz, J.-M., Bonneton, P., Butet, A. & Hopfinger, E. J. 1993*a* Vertical diffusion of the far wake of a sphere moving horizontally in a stratified fluid. *Phys. Fluids* **5**, 2799–2806.

Chomaz, J.-M., Bonneton, P. & Hopfinger, E. J. 1993*b* The structure of the near wake of a sphere moving horizontally in a stratified fluid. *J. Fluid Mech.* **254**, 1–21.

Chomaz, J. M., Bonneton, P. & Hopfinger, E. J. 1993a The structure of the near wake of a sphere moving horizontally in a stratified fluid. *J. Fluid Mech.* **254** (1), 1–21.

Chongsiripinyo, K., Pal, A. & Sarkar, S. 2016 On the vortex dynamics of flow past a sphere at Re = 3700 in a uniformly stratified fluid (in revision). *Phys. Fluids* .

Constantinescu, George S & Squires, Kyle D 2003 LES and DES investigations of turbulent flow over a sphere at Re= 10,000. *FTC* **70** (1-4), 267–298.

Dairay, T., Obligado, M. & Vassilicos, J.C. 2015 Non-equilibrium scaling laws in axisymmetric turbulent wakes. *J. Fluid Mech.* **781**, 166–195.

Diamessis, P. J., Spedding, G. R. & Domaradzki, J. A. 2011 Similarity scaling and vorticity structure in high Reynolds number stably stratified turbulent wakes. *J. Fluid Mech.* **671**, 52–95.

Dohan, K. & Sutherland, B.R. 2003 Internal waves generated from a turbulent mixed region. *Phys. Fluids* **15** (2), 488–498.

Dommermuth, D. G., Rottman, J. W., Innis, G. E. & Novikov, E. A. 2002 Numerical simulation of the wake of a towed sphere in a weakly stratified fluid. *J. Fluid Mech.* **473**, 83–101.

George, William K 1989 The self-preservation of turbulent flows and its relation to initial conditions and coherent structures. *Advances in Turbulence* pp. 39–73.

Ghosal, Sandip & Rogers, Michael M 1997 A numerical study of self-similarity in a turbulent plane wake using large-eddy simulation. *Physics of Fluids (1994-present)* **9** (6), 1729–1739.

Gilreath, H. E. & Brandt, A. 1985 Experiments on the generation of internal waves in a stratified fluid. *AIAA J.* **23** (5), 693–700.

Gourlay, M. J., Arendth, S. C., Fritts, D. C. & Werne, J. 2001 Numerical modeling of initially turbulent wakes with net momentum. *Phys. Fluids A* **13**, 3783–3802.

Greenslade, M. D. 2000 Drag on a sphere moving horizontally in a stratified fluid. *J. Fluid Mech.* **418**, 339–350.

Hanazaki, H. 1988 A numerical study of three-dimensional stratified flow past a sphere. *J. Fluid Mech.* **192**, 393–419.

Henderson, R. D. 1995 Details of the drag curve near the onset of vortex shedding,. *Phys. Fluids* **9**, 2102–2104.

Higuchi, H. & Kubota, T. 1990 Axisymmetric wakes behind a slender body including zero-momentum configurations. *Phys. Fluids* **2** (9), 1615–1623.

Hopfinger, EJ, Flor, J-B, Chomaz, J-M & Bonneton, P 1991 Internal waves generated by a moving sphere and its wake in a stratified fluid. *Exp. Fluids* **11** (4), 255–261.

Jacobitz, F. G . & Sarkar, S. 1998 The effect of nonvertical shear on turbulence in a stably stratified medium. *Phys. Fluids* **10** (5), 1158–1168.

Jacobitz, F. G . & Sarkar, S. 1999 A direct numerical study of transport and anisotropy in a stably stratified turbulent flow with uniform horizontal shear. *Flow Turbul. Combust.* **63** (1), 343 – 360.

Kim, H. J. & Durbin, P. A. 1988 Observations of the frequencies in a sphere wake and of drag increase by acoustic excitation. *Phys. Fluids* **31** (11), 3260–3265.

Kundu, Piyush, K. & Cohen, Ira, M. 2011 *Fluid Mechanics*. Elsevier.

Legendre, D, Merle, A & Magnaudet, J 2006 Wake of a spherical bubble or a solid sphere set fixed in a turbulent environment. *Phys. Fluids* **18**, 048102.

Lighthill, M. J. 1955 *Waves in Fluids*. Cambridge University Press.

Lin, J. T. & Pao, Y. H. 1979 Wakes in stratified fluids. *Ann. Rev. Fluid Mech.* **11**, 317–338.

Lin, Qiang, Boyer, DL & Fernando, HJS 1992*a* Turbulent wakes of linearly stratified flow past a sphere. *Physics of Fluids A: Fluid Dynamics (1989-1993)* **4** (8), 1687–1696.

Lin, Q., Lindberg, W. R., Boyer, D. L. & Fernando, H. J. S. 1992*b* Stratified flow past a sphere. *J. Fluid Mech.* **240**, 315–354.

Lindborg, E. 2006 The energy cascade in a strongly stratified fluid. *J. Fluid Mech.* **550**, 207–242.

Lofquist, K. E. B. & Purtell, L. P. 1984 Drag on a sphere moving horizontally through a stratified liquid. *J. Fluid Mech.* **148**, 271–284.

Marella, S., Krishnan S. Liu H. Udaykumar H. S. 2005 Sharp interface cartesian grid method i: an easily implemented technique for 3d moving boundary computations. *Journal of computational Physics* **210** (1), 1–31.

Meunier, P., Diamessis, P. J. & Spedding, G. R. 2006 Self-preservation in stratified momentrum wakes. *Phys. Fluids* **18** (10), 106601.

Meunier, P. & Spedding, G. R. 2006 Stratified propelled wakes. *J. Fluid Mech.* **552**, 229–256.

Mittal, R. & Balachandar, S. 1995 Effect of three-dimensionality on the lift and drag of nominally two-dimensional cylinder. *Phys. Fluids* **7** (8), 1841–1865.

Moser, Robert D, Rogers, Michael M & Ewing, Daniel W 1998 Self-similarity of time-evolving plane wakes. *Journal of Fluid Mechanics* **367**, 255–289.

Naudascher, E. 1965 Flow in the wake of self-propelled bodies and related sources of turbulence. *J. Fluid Mech.* **22** (4), 625–656.

Nedić, J., Vassilicos, J. C. & Ganapathisubramani, B. 2013 Axisymmetric turbulent wakes with new nonequilibrium similarity scalings. *Phys. Rev. Lett.* **111** (14), 144503.

Orr, T. S, Domaradzki, J. A., Spedding, G. R. & Constantinescu, G. S. 2015 Numerical simulations of the near wake of a sphere moving in a steady, horizontal motion through a linearly stratified fluid at Re= 1000. *Phys. Fluids* **27** (3), 035113.

Pal, A., de Stadler, M. B. & Sarkar, S. 2013 The spatial evolution of fluctuations in a self-propelled wake compared to a patch of turbulence. *Phys. Fluids* **25**, 095106.

Pal, A. & Sarkar, S. 2015 Effect of external turbulence on the evolution of a wake in stratified and unstratified environments. *J. Fluid Mech.* **772**, 361–385.

Pal, A., Sarkar, S., Posa, A. & Balaras, E. 2016*a* Dns of stratified flow past a sphere at a Reynolds number of 3700. *J. Fluid Mech.* **submitted**.

Pal, A., Sarkar, S., Posa, A. & Balaras, E. 2016*b* Regeneration of turbulent fluctuations in low-Froude number flow over a sphere at a Reynolds number of 3700. *J. Fluid Mech.* **804, R2**, 1–11.

Parnaudeau, P., Carlier, J., Heitz, D. & Lamballais, E. 2008 Experimental and numerical studies of the flow over a circular cylinder at Reynolds number 3900. *Phys. Fluids* **20** (8), 085101.

Pasquetti, R 2011 Temporal/spatial simulation of the stratified far wake of a sphere. *Comput. Fluids* **40** (1), 179–187.

Pham, H. T., Sarkar, S. & Brucker, K. A. 2009 Dynamics of a stratified shear layer above a region of uniform stratification. *J. Fluid Mech.* **630**, 191–223.

Redford, J.A. & Coleman, G.N. 2007 Numerical study of turbulent wakes in background turbulence. *5th International Symposium on Turbulence and Shear Flow Phenomena (TSFP-5 Conference), Munich, Germany,* pp. 561–566.

Redford, J. A., Castro, I. P. & Coleman, G. N. 2012 On the universality of turbulent axisymmetric wakes. *J. Fluid Mech.* **710**, 419.

Redford, J. A., Lund, T. S. & Coleman, G. N. 2015 A numerical study of a weakly stratified turbulent wake **776**, 568–609.

Riley, J. J. & deBruynKops, S. M. 2003 Dynamics of turbulence strongly influenced by buoyancy. *Phys. Fluids* **15** (7), 2047–2059.

Rind, E. & Castro, I. P. 2012*a* Direct numerical simulation of axisymmetric wakes embedded in turbulence. *J. Fluid Mech.* **710**, 482.

Rind, E. & Castro, I. P. 2012*b* On the effects of free-stream turbulence on axisymmetric disc wakes. *Exp. Fluids* **53** (2), 301–318.

Rodriguez, I., Borelli, Y., Lehmkuhl, O., Perez Segarra, C. D. & A., Oliva. 2011 Direct numerical simulation of the flow over a sphere at re = 3700. *J. Fluid Mech.* **679**, 263–287.

Rogallo, R. S. 1981 Numerical experiments in homogeneous turbulence. *Tech. Rep.* 81315. NASA.

Rossi, T. & Toivanen, J. 1999 A parallel fast direct solver for block tridiagonal systems with separable matrices of arbitrary dimension. *SIAM J. Sci. Comp.* **20** (5), 1778–1793.

Sakamoto, Haniu & Haniu, H 1990 A study on vortex shedding from spheres in a uniform flow. *J. Fluid Eng.* **112** (4), 386–392.

Schlichting, H 1979 *Boundary Layer Theory*. McGraw-Hill.

Seidl, V, Muzaferija, S & Perić, M 1997 Parallel dns with local grid refinement. *Appl. Sci. Res.* **59** (4), 379–394.

Sirviente, A. I. & Patel, V. C. 2000 Wake of a self-propelled body, part 1: Momentumless wake. *AIAA J.* **38** (4), 613–619.

Spedding, G. 1997 The evolution of initially turbulent bluff-body wakes at high internal Froude number. *J. Fluid Mech.* **337**, 283–301.

Spedding, G. R. 2002 Vertical structure in stratified wakes with high initial Froude number. *J. Fluid Mech.* **454**, 71–112.

Spedding, G. R. 2014 Wake signature detection. *Ann. Rev. Fluid Mech.* **46**, 273–302.

Spedding, G. R., Browand, F. K. & Fincham, A. M. 1996a The long-time evolution of the initially turbulent wake of a sphere in a stable stratification. *Dyn. Atmos. Oceans* **23** (1-4), 171–182.

Spedding, G. R., Browand, F. K. & Fincham, A. M. 1996b Turbulence, similarity scaling and vortex geometry in the wake of a towed sphere in a stably stratified fluid. *J. Fluid Mech.* **314**, 53–103.

de Stadler, Matthew B, Rapaka, Narsimha R & Sarkar, Sutanu 2014 Large eddy simulation of the near to intermediate wake of a heated sphere at Re= 10,000. *Int. J. Heat. Fluid Flow* **49**, 2–10.

de Stadler, M. B. & Sarkar, S. 2012 Simulation of a propelled wake with moderate excess momentum in a stratified fluid. *J. Fluid Mech.* **692**, 28–52.

Sutherland, B.R. & Linden, P.F. 1998 Internal wave excitation from stratified flow over a thin barrier. *J. Fluid Mech.* **377**, 223–252.

Taylor, J. R. & Sarkar, S. 2007 Internal gravity waves generated by a turbulent bottom ekman layer. *J. Fluid Mech.* **590**, 331–354.

Tennekes, H. & Lumley, J. L. 1972 *A first course in Turbulence*. Cambridge,Massachusetts: The MIT press.

Tomboulides, Ananias G. & Orszag, Steven A. 2000 Numerical investigation of transitional and weak turbulent flow past a sphere. *J. Fluid Mech.* **416**, 45–73.

Uberoi, M. S. & Freymuth, P. 1970 Turbulent energy balance and spectra of axisymmetric wake. *Phys. Fluids* **13** (9), 2205–2210.

Voisin, B. 1991 Internal wave generation in uniformly stratified fluids. part 1. greens function and point sources. *J. Fluid Mech.* **231**, 439–480.

Voisin, B. 1994 Internal wave generation in uniformly stratified fluids. part 2. moving point sources. *J. Fluid Mech.* **261**, 333–374.

Voisin, B. 2007 Lee waves from a sphere in a stratified flow. *J. Fluid Mech.* **574**, 273–315.

Voropayev, S. I., McEachern, G. B., Fernando, H. J. S. & Boyer, D. L. 1999 Large vortex structures behind a maneuvering body in stratified fluids. *Phys. Fluids* **11** (6), 1682–1684.

Vosper, S. B., Castro, I. P., Snyder, W. H. & Mobbs, S. D. 1999 Experimental studies of strongly stratified flow past three-dimensional orography. *J. Fluid Mech.* **390**, 223–249.

Wu, J-S & Faeth, G. M. 1994 Sphere wakes at moderate Reynolds numbers in a turbulent environment. *AIAA J.* **32** (3), 535–541.

Wu, J-S & Faeth, G. M. 1995 Effect of ambient turbulence intensity on sphere wakes at intermediate Reynolds number. *AIAA J.* **33** (1), 171–173.

Yang, Jianming 2005 An embedded-boundary formulation for large-eddy simulation of turbulent flows interacting with moving boundaries. *PhD. Thesis* .

Yang, J. & Balaras, E. 2006 An embedded-boundary formulation for large-eddy simulation of turbulent flows interacting with moving boundaries. *J. Comput. Phys.* **215** (1), 12–40.

Yavneh, Irad 1996 On red-black SOR smoothing in multigrid. *SIAM J. Sci. Comput.* **17** (1), 180–192.

Yun, Giwoong, Kim, Dongjoo & Choi, Haecheon 2006 Vortical structures behind a sphere at subcritical reynolds numbers. *Phys. Fluids* **18** (1), 015102.